

ABSTRACT

Title of Document: ESTIMATION OF ULTRASOUND INDUCED
HEAT GENERATION RATES FOR
THERAPEUTIC APPLICATIONS

Esteban Echeverría Fernández, M.S., 2012

Directed By: Dr. Chandrasekhar Thamire, Department of
Mechanical Engineering

The use of ultrasound for therapeutic applications has been increasingly examined mostly because of its noninvasive nature. Though many experimental studies have been conducted to verify the feasibility of the method, no correlations predicting the ultrasonic parameters required to generate prescribed volumetric heat generation rates. In this study, heat generated due to propagation of ultrasound, in soft tissue mimicking material, is examined. Using numerical methods, pressure fields are first computed for different source geometries, signal frequencies, and signal waveforms. Volumetric heat generation rates are then calculated from the computed pressures. The Klinger and Pennes bioheat transfer models are used to compute the temperature distributions. Results from this study will be useful in estimating the volumetric heat generation fields from prescribed ultrasound parameters, which in turn can be used to design ultrasound devices as well as treatment protocols for a variety of therapeutic applications.

ESTIMATION OF ULTRASOUND INDUCED HEAT GENERATION RATES
FOR THERAPEUTIC APPLICATIONS

By

Esteban Echeverría Fernández

Thesis submitted to the Faculty of the Graduate School of the
University of Maryland, College Park, in partial fulfillment
of the requirements for the degree of
Master of Science
2012

Advisory Committee:

Dr. Chandrasekhar Thamire, Chair

Dr. Amir Riaz

Dr. Kenneth Kiger

© Copyright by

Esteban Echeverría Fernández

2012

Dedication

To my dear parents:

Carlos Manuel Echeverría Esquivel and Sara María Fernández Araya

Thank you for all the love and support. I have truly been blessed with all the tools you have given to me. I promise you they will only be used for good.

Acknowledgements

I would like to acknowledge Dr. Chandrasekhar Thamire for his constant support and help while developing this study. His kindness and patience are very much appreciated and will never be forgotten.

I also thank Andrew Oles for all his useful insight and help in the development of the numerical analysis. Your friendship will always be very valuable to me.

I want to give special thanks to my lab partners Danica Gordon and Babak Eslami for all the support given while completing my course requirements. I wish you both the best of luck in your future projects and endeavors.

Finally, I want to thank my other lab partners along with my close friends, family, and loved ones for all the support given.

Table of Contents

Dedication	ii
Acknowledgements	iii
Table of Contents	iv
List of Tables	vi
List of Figures	vii
Chapter 1: Introduction	1
Therapeutic Applications of Ultrasound	1
Biophysical Effects of Ultrasound in Tissue	2
Objective of the Study	5
Chapter 2: Background	8
Nonlinear Acoustics	8
Transducer Theory	15
Piezoelectric Effect and Transducer Devices	16
Transducer Geometry and Signal Types	18
Experimental Methods for Simulating Pressure Fields	22
Intensity and Heat Generation	24
Temperature Analysis	26
Chapter 3: Numerical Scheme	33
Modeling	33
Schematic	33
Geometry	34
Finite Difference Methods	36
Pressure Field Discretization	37
Pressure Field Boundary Conditions	41
Stability of the Numerical Procedure for Pressure Solution	46
Volumetric Heat Generation	47

Temperature Discretization	48
Temperature Field Stability/Grid Coarsening	51
Chapter 4: Results and Discussion.....	58
Pressure Field	59
Unfocused Signals	60
Focused Signals	69
Heat Generation.....	71
Selection of Time Average	72
Continuous Wave Vs. Pulsed Signals	74
Temperature	75
Stability.....	76
Unfocused Sources	79
Focused Sources	83
Effect of Advection and Viscous Dissipation	85
Effect of Blood Perfusion.....	91
Mathematical Relationship between Maximum Pressure and Signal Parameters for Unfocused Sources	95
Mathematical Relationship between Maximum Volumetric Heat Generation and Signal Parameters for Unfocused Sources	98
Chapter 5: Conclusion.....	102
Pressure Field	102
Heat Generation.....	103
Temperature	103
Final Thoughts.....	104
Appendix A: Nomenclature	106
Chapter 6: Bibliography.....	107

List of Tables

Table 1: Properties of prostate tissue	58
Table 2: Error between Magnitude and Location of the Maximum Pressure with respect to the Calculated Focal Point: $P_0=1$ MPa	66
Table 3: Resulting Gain and Error with respect to linear Gain Theory for a 0.25MPa, and 1 MHz signal with a radius source of 10 mm	71
Table 4: Values for Maximum Temperature and Relative Error with Different values of N and M, induced by a 0.25 MPa and 1MHz continuous wave signal with a source radius of 8 mm for 30 s	77

List of Figures

Figure 1: Biological applications of ultrasound.....	1
Figure 2: Depiction of sound waves; top: transverse (mathematical description) bottom: longitudinal (physical description, where undisturbed particle is represented on the top line and the disturbed particle in the bottom line. C stands for Compression and R for Rarefaction).....	9
Figure 3: Piezoelectric effect (generator action) and inverse piezoelectric effect (motor action) (Permission granted by APC International, Ltd.) [47].....	16
Figure 4: Diagram of a typical ultrasonic transducer [48].....	17
Figure 5: Top: Pressure vs. time for continuous wave (CW) signal described by Eq. 19 Bottom: Pressure vs. time for pulsed signal described by Eq. 20 for $n = 5$ and $m = 2$	19
Figure 6: Transducer geometries to be studied: focused (left) and planar (right) disk transducers	20
Figure 7: Schematic of focused transducer with its respective geometric parameters	21
Figure 8: Schematic of generic ultrasound experiment	23
Figure 9: Schematic view of biological soft tissue [57]	26
Figure 10: Simplified Schematic View of Biological Tissue	27
Figure 11: Schematic of a transducer delivering an ultrasound signal to a certain medium	34
Figure 12: Left: Representation of Medium as an Axisymmetric Cylinder; Right: Cylinder's Radial and Propagation Coordinates r and z , respectively.....	35
Figure 13: Schematic of the spatial grid used.....	37
Figure 14: Illustration of the method used to define the symmetry boundary for all z when $r=0$	42
Figure 15: Absorption coefficient versus distance. L and R are the tissue's propagation and radial length, respectively Left: r -axis profile, Right: z -axis profile	43
Figure 16: Schematic for the spatial pressure and temperature field used, where the larger dots define the temperature field nodes and the smaller dots define the pressure field nodes	53

Figure 17: Left: schematic of certain point in space described for index values of temperature; Right: schematic of the same point in space described for index values of pressure	55
Figure 18: Results for axial profile of normalized peak pressures $P_o=0.5MPa$, $f=1MHz$, $R_s=7mm$; Left: Obtained with numerical scheme of this study; Right: separated into the first three harmonics, obtained with numerical scheme study by Huijssen [26].....	59
Figure 19: Pressure contour graphs (Pa) for a continuous wave signal in development: $P_o=1MPa$, $f=1MHz$, $R_s=5mm$; Top left: for $t=10\ \mu s$, Top right: for $t=20\ \mu s$, Bottom left: for $t=30\ \mu s$, Bottom right: for $t=40\ \mu s$,	61
Figure 20: Pressure Contour graphs (Pa) for a Pulsed Signal in Development: $P_o=1MPa$, $f=1MHz$, $R_s=5mm$ $T_o=0.1\ \mu s$, $DF=0.25\%$	62
Figure 21: Axial Normalized Pressure for an Unfocused Source Delivering a Continuous Wave Signal: $P_o=1\ MPa$, $f=1\ MHz$, $R_s=5mm$	63
Figure 22: Root Mean Squared Pressure (Last 20% of the propagation Time) For Different Frequencies Prescribed by an Unfocused Source: $P_o=1MPa$, $R_s=5mm$	64
Figure 23: Root Mean Squared Pressure (Last 20% of the propagation Time) For Different Source Radii Prescribed by an Unfocused Source: $P_o=1MPa$, $f=1\ MHz$	65
Figure 24: Left: Pressure contours for $P_o=1\ MPa$, $f=0.75\ MHz$, $R_s=8mm$, $ka=25.13$; right: pressure contours for $P_o=1\ MPa$, $f=1\ MHz$, $R_s=6mm$, $ka=25.13$	67
Figure 25: Root Mean Squared Pressure (last 20% of the Propagation time) for Different Source Pressures Prescribed.....	68
Figure 26: Root Mean Normalized Squared Pressure (last 20% of the Propagation time) for Different Source Pressures Prescribed.....	69
Figure 27: Pressure Contour for a focused source $P_o=0.25\ MPa$, $f=1\ MHz$, $R_s=10mm$, Left: $\epsilon=11.20mm$, Right: $\epsilon=17.30\ mm$	70
Figure 28: Axial Profile of Average Volumetric Heat Generation for different Time Ranges	73
Figure 29: Contour Graphs For Volumetric Heat Generation Fields $P_o=0.5\ MPa$, $f=1\ MHz$, $R_s=7.5mm$, Left: CW Signal, Right: Pulsed Signal, $T_o=0.1\ \mu s$ $DF=0.35\%$	74
Figure 30: Contour Graphs For Volumetric Heat Generation Fields $P_o=0.25\ MPa$, $f=1\ MHz$, $R_s=10mm$, $\epsilon=11.20\ mm$; Left: CW Signal, Right: Pulsed Signal, $DF=0.25\%$	75

Figure 31: Schematic of Both Pressure and Temperature Grids Points Illustrating the Values of M and N	76
Figure 32: Graph of The Relative Error vs. N for Different values of M (Increasing values of these two numbers leads to decrease in the overall amount of nodes.....)	78
Figure 33: Contour Graph for Temperature Field at Different Times for an Unfocused Source $Po=0.25 MPa, f=1 MHz, Rs= 8mm ka=33.51$	80
Figure 34: Contour Graph for Temperature Field at different Times for an Unfocused Source $Po=0.25 MPa, f=1 MHz, Rs= 10mm ka=41.88$	81
Figure 35: Contour Graph for the rate of change of the Temperature Field at different Times for an Unfocused Source $Po=0.25 MPa, f=1 MHz, Rs= 8mm$	82
Figure 36: Contour Graph for Temperature Field at different Times for a Focused Source $Po=0.25 MPa, f=1 MHz, Rs= 10mm, \epsilon = 11.20 mm$	83
Figure 37: Contour Graph for Temperature Field at different Times for a Focused Source $Po=0.25 MPa, f=1 MHz, Rs= 10, \epsilon = 11.20 mm, DF=0.25\%$	84
Figure 38: Contour Graph for the rate of change of the Temperature Field at different Times $Po=0.25 MPa, f=1 MHz, Rs= 10mm \epsilon = 11.20 mm$	85
Figure 39: Left: Contour Graph of Streamlines for an Unfocused Source $Po=0.25 MPa, f=1 MHz, Rs= 10mm$ Time=40s; Right: Closed-Up of Enclosed Area with Velocity Vectors Included.....	86
Figure 40: Left: Contour Graph of Streamlines for a Focused Source $Po=0.25 MPa, f=1 MHz, Rs= 10mm \epsilon = 11.20 mm$ Time=20s; Right: Closed-Up of Enclosed Area with Velocity Vectors Included	87
Figure 41: Contour Graph for the Temperature Field for an Unfocused Source $Po=0.25 MPa, f=1 MHz, Rs= 10mm, Time=40s$, for the Case $\psi = 0$	88
Figure 42: Contour Graph for the Temperature Field Percentage Difference in between Porous and Nonporous Media for an Unfocused Source $Po=0.25 MPa, f=1 MHz, Rs= 10mm, Time=40s$	89
Figure 43: Contour Graph for the Temperature Field for an Focused Source $Po=0.25 MPa, f=1 MHz, Rs= 10mm, \epsilon = 11.20 mm, Time=20s$, for the Case $\psi = 0$	90

Figure 44: Contour Graph for the Temperature Field Percentage Difference in between Porous and Nonporous Media for a Focused Source $P_o=0.25\text{ MPa}$, $f=1\text{ MHz}$, $R_s=10\text{ mm}$, $\epsilon = 11.20\text{ mm}$, $\text{Time}=20\text{ s}$ 91

Figure 45: Contour Graphs for the Temperature Field delivered by an Unfocused Source $P_o=0.25\text{ MPa}$, $f=1\text{ MHz}$, $R_s=10\text{ mm}$, $\text{Time}=40\text{ s}$, for different Cases of WP_{ennes} 93

Figure 46: Contour Graphs for the Changes in Temperature Field with respect to the field in Figure 40: delivered by an Unfocused Source $P_o=0.25\text{ MPa}$, $f=1\text{ MHz}$, $R_s=10\text{ mm}$, $\text{Time}=40\text{ s}$, for Different Cases of WP_{ennes} 94

Figure 47: Scatter plot of Pressure at the Focal Point PPF vs. ka number. Data points were obtained from various experiments with different values for signal frequency f , source Pressure P_o , and source radii R_s 96

Figure 48: Scatter plot of quantity Θ vs. ka number. Data points were obtained from various experiments with different values for signal frequency f , source Pressure P_o , and source radii R_s 97

Figure 49: Scatter plot of Heat Generation at the Focal Point QFP vs. ka number. Data points were obtained from various experiments with different values for signal frequency f , source Pressure P_o , and source radii R_s 99

Figure 50: Scatter plot of quantity Γ vs. ka number. Data points were obtained from various experiments with different values for signal frequency f , source Pressure P_o , and source radii R_s 100

Chapter 1: Introduction

Therapeutic Applications of Ultrasound

The use of ultrasound in biological applications has been increasing in the past few decades. Close to one century ago, it was discovered that high frequency ultrasonic waves with high intensities produced long lasting biological and physical effects [1]. Since then, it has been used for a great range of applications. Figure 1 shows some important applications of ultrasound [2].

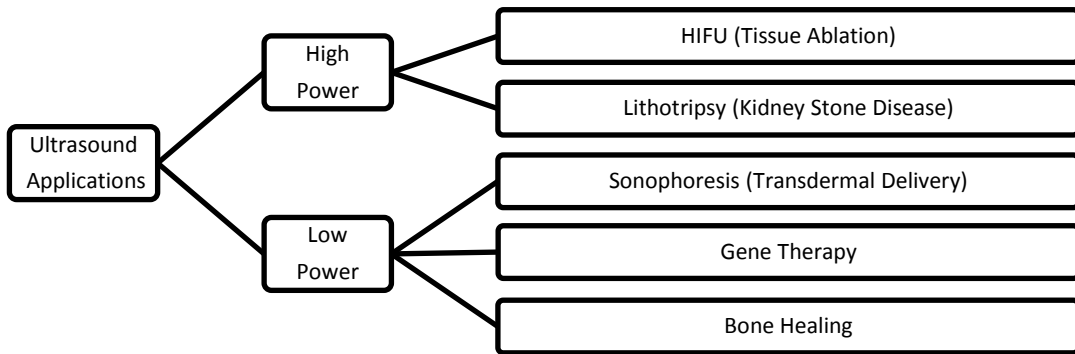


Figure 1 Biological applications of ultrasound

These applications use different ultrasonic power levels and frequencies, as well as different types of sources and treatment durations. Several therapies and treatments are making use of these applications. For example, High Intensity Focused Ultrasound (HIFU) have been used for prostate and breast cancer [3] [4] [5] [6], as well as treatment for brain tumors [7] [8] [9], and glaucoma [10]. Moreover, guided ultrasound and sonophoresis have been used to deliver different drugs and compounds to treat illnesses such as Parkinson’s disease, various types of cancer, cardiovascular disorders, and hormone replacement therapy [11] [12] [13].

The application of therapeutic ultrasound involves a transducer that transforms electrical energy into mechanical pressure in the form of ultrasonic waves. These waves are able to travel through tissue and have characteristic pressure magnitudes and frequencies. Usually, the application of ultrasound requires no break in the skin or any internal body cavity beyond an artificial orifice. This is often useful for therapies where surgical procedures and resulting side effects are to be avoided.

Biophysical Effects of Ultrasound in Tissue

Traveling ultrasound signals get absorbed by the medium as they propagate and their energy either transforms into heat, increasing the temperature of the medium, or induces interstitial fluid flow. Both phenomena might serve as an advantage or an issue depending on the application.

The effects of ultrasound in tissue have been traditionally classified to be either thermal or non-thermal [14]. Thermal effects are those caused by the temperature rise in tissue. The direct effect due to temperature rise is tissue ablation [15] [16] [17], however, homeostatic mechanisms in the tissue activate once unusual temperature rise has been detected [18]. The most common effect is the increment perfusion due to changes in blood flow [19], which fails to prevent temperature rise for ultrasonic applications [20].

Non-thermal effects normally fall into the category of cavitation, which can be used to describe any mechanism regarding the formation of small bubbles in the medium. However, it has been proved “difficult to demonstrate” that this mechanism occurs at the intensities usually used for ultrasonic signals [21]. Acoustic streaming is the effect of fluid flow in the medium, resulting

from the vibration of the bubbles formed [22]. This fluid can either swirl in the form of eddies or can be travelling in a certain direction [21].

Both thermal and non-thermal effects are used for a wide variety of applications, but both effects usually are not desired to develop at the same time. It has been stated that the development of these depends on the method of ultrasonic delivery (continuous or pulsed signals), as well as the geometry of the ultrasonic source used (either focused or unfocused) [21].

When used for tissue ablation, ultrasound is used to generate heat in a specific area. High Intensity Focused Ultrasound (HIFU) concentrates the signal delivered by the transducer which accurately generates heat in a specific region of interest. By focusing the ultrasound signal, this region can be targeted for accurate ablation, leaving the surrounding healthy tissue nearly intact [23]. Other applications such as sonophoresis or gene therapy do not use ultrasound for tissue ablation purposes. These usually use unfocused sources delivering pulsed signals because these generate less heat while providing the required non-thermal effects with the same efficacy, as claimed in past studies [24]. Heat generation is an important factor that might negatively affect the outcomes of these applications and it has to be controlled.

Even though it has been stated that that thermal and non-thermal effects are separable and completely dependent on the source signal, there is some dispute regarding how separable can these really be [21]. According to studies, the mechanisms by which physical effects are produced due to ultrasound are not clearly understood [2]. It has been concluded in the past that, because of the lack of evidence for a biological rationale, the use of ultrasound for therapeutic

applications is “unlikely to be beneficial” [21]. These reasons show that, thermal and non-thermal effects induced by ultrasound have to be studied, regardless of the source and signal geometry.

Numerical and analytical methods have been used to model the pressure propagation, in thermoviscous fluids, obtained by different driving sources. Hallaj et al. performed FDTD (Finite Difference in Time Domain) simulations for pressure propagation, where they proved the nonlinearity of ultrasound waves travelling through a medium and the temperature rise due to the absorbed energy on unfocused sources [25]. Huijssen, et al. used these methods for the same type of source to compare results obtained from two different pressure propagation models [26].

Liu et al. performed numerical simulations for focused sources and compared the results obtained from inclusion of exclusion of nonlinear terms, developing an extra absorption factor, for the obtained heat generation, for compensation [27]. Khokhlova et al. have numerically modeled ultrasound propagation in both frequency and time domains for both unfocused sources [28], leading to conclusions about the nonlinearity present, development of weak shocks, and the pressure distribution of the propagating wave. Makov et al. used numerical methods to inspect the linear focal shift effect happening in unfocused sources [29].

Experimental methods, used for proper validation of the models, have been developed. Huijssen, et al. [26], Liu et al. [27], Canney et al. [30], Hallaj et al. [31], and Kruse et al. [32] compared their pressure propagation results for different models with experimental data. Nonlinear behavior of the pressure propagation profile around a geometrical or natural focal point has been

observed for these studies. Pinton et al. compared the same results with experimental data for heterogeneous mediums, having different acoustic and thermal properties [33].

Numerical methods used to describe temperature rise due to ultrasound have been developed. Both of the mentioned work by Hallaj et al. have included results for temperature rise due to ultrasound induced heat generation [31] [25]. Moreover, Lee et al. compared the numerical results for temperature rise with experimental data [34].

The main challenge faced is the “lack of treatment protocol planning and real-time treatment monitoring” [35]. Properly modeling the relationship between the ultrasound doses and resulting temperature rise provides a useful tool for efficient application and design of ultrasonic instruments, as well as open the possibility for creating treatment protocols, for various applications.

Objective of the Study

The objective of this study is to establish simple relationships between ultrasonic dosages and volumetric heat generation rates in specific types of tissue. The ultrasound signal's pressure and frequency prescribed as well as the ultrasound source geometry will be used are the primary factors that affect the volumetric heat generation rates.

A secondary objective of this study is to determine if thermal heat dissipation effects due to moving interstitial fluid, such as perfusion and natural convection, are needed for proper

modeling of temperature rise in tissue. This objective will be achieved by examining different temperature models for ultrasound induced heat generation.

This study does not include non-thermal effects such as cavitation or acoustic streaming. However, future work regarding the inspection of only non-thermal effects, as well as both types, will be able to use the methods developed in this study.

The developed relationships will serve as a tool for future design and use of focused and unfocused ultrasonic applicators. The developed methods will also present new ways of analyzing similar models needed for further research regarding ultrasound delivery in soft tissue.

The background required for the study, which encompasses nonlinear acoustics and heat generation theory, along with the models used, will be presented in the following chapters. The numerical schemes for the pressure and temperature analysis will be presented, as well as the coupling method used to reduce overall computational expenses. Finally, resulting temperature increments for different signals and sources will be examined and compared.

The pressure distribution, heat generation, and temperature rise will be analyzed for several signal frequencies and pressures, ranging from 0.8 to 1.25 MHz and 0.1 MPa to 1 MPa, respectively. Several relationships regarding the maximum values for pressure and heat generation and their distance from the source will be presented as functions of the prescribed parameters. Temperature distributions will be analyzed and the importance of the heat dissipation due to convection and perfusion will be examined.

Chapter 2: Background

In this chapter, specific topics of nonlinear acoustic theory needed to understand ultrasound wave propagation will be covered, followed by the introduction of transducer theory. The concepts and parameters behind each of these will be discussed further. Moreover, mathematical models for both will also be presented for later use and experimental methods used to study the propagation of ultrasound signals will also be reviewed.

The theory and mathematical models used for pressure propagation, heat generation and temperature rise will be subsequently presented and analyzed in order to develop the numerical method needed to perform the experiments.

Nonlinear Acoustics

Propagation of finite amplitude sound waves are described with the fundamental laws of mass and momentum conservation. Further, modeling of propagating waves in thermoviscous fluids have led to the use of nonlinear acoustics to describe ultrasound propagation in biological tissue. The general theory of nonlinear acoustics will now be explained, followed by introducing mathematical models that describe it.

Sound is recognized to be the phenomenon of periodic pressure waves, with a defined amplitude and frequency, traveling through a medium. Ultrasound is defined as pressure waves that travel at frequencies higher than the threshold value detected by the human hearing sense, which is 20

kHz [36]. Figure 2 shows a plot of the exerted pressure induced by a sound wave on a specific region with time (top), as well as the physical representation of the wave (bottom). The compression and rarefaction induced by the wave indicates that the waves are longitudinal, which means that they travel in a “slinky-like” fashion. For solids, or thermoviscous fluids, these mainly depend on the time-varying stress applied to the medium [37].

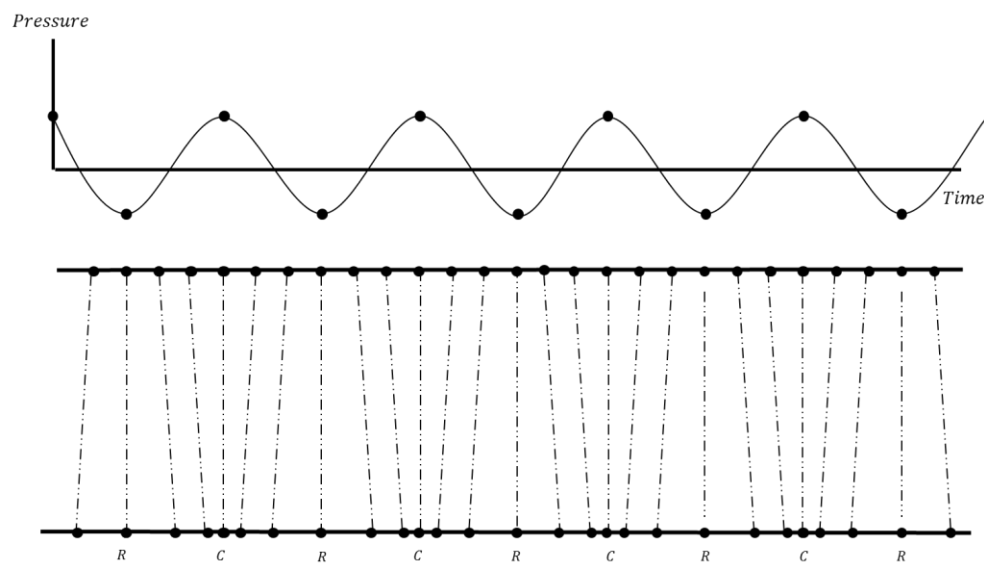


Figure 2 Depiction of sound waves; top: transverse (mathematical description) bottom: longitudinal (physical description, where undisturbed particle is represented on the top line and the disturbed particle in the bottom line. C stands for Compression and R for Rarefaction)

The fundamental equations used to calculate sound waves are shown below [36]. Eq. 1 is the continuity equation, where ρ [kg/m^3] is the density, t is time [s], and \vec{u} is the fluid velocity vector.

$$\frac{\partial \rho}{\partial t} + \bar{u} \cdot \nabla \rho + \rho \nabla \cdot \bar{u} = 0 \quad \text{Eq. 1}$$

Eq. 2 is the momentum equation, where μ [$\text{kg s}^{-1}\text{m}^{-1}$] is the shear viscosity, μ_B [$\text{kg s}^{-1}\text{m}^{-1}$] is the bulk viscosity, and P [kg m/s^2] is the pressure. The last two terms account for the diffusion of momentum by viscous terms.

$$\rho \left(\frac{\partial \bar{u}}{\partial t} + \bar{u} \cdot \nabla \bar{u} \right) + \nabla P = \mu \nabla^2 \bar{u} + \left(\mu_B + \frac{1}{3} \mu \right) \nabla (\nabla \cdot \bar{u}) \quad \text{Eq. 2}$$

Eq. 3 is the entropy equation, where s [$\text{J K}^{-1} \text{kg}^{-1}$] is the specific entropy per unit mass, T [K] is the temperature, k [$\text{W K}^{-1} \text{m}^{-1}$] is the coefficient of thermal conductivity and $\delta_{i,j}$ is the Kronecker delta. The index numbers i and j are used to represent the velocity and the direction x in Cartesian notation.

$$\rho T \left(\frac{\partial s}{\partial t} + \bar{u} \cdot \nabla s \right) = k \nabla^2 T + \mu_B (\nabla \cdot \bar{u}) + \frac{1}{2} \mu \left(\frac{\partial \bar{u}_i}{\partial x_j} + \frac{\partial \bar{u}_j}{\partial x_i} + \frac{2}{3} \delta_{i,j} \frac{\partial \bar{u}_k}{\partial x_k} \right)^2 \quad \text{Eq. 3}$$

Finally, the state equation, shown in Eq. 4 is written in terms of the entropy, for convenience, instead of the temperature.

$$P = P(\rho, s) \quad \text{Eq. 4}$$

Nonlinear acoustic effects have to be taken into account for modeling therapeutic ultrasound, as they cannot be ignored at high frequencies and pressures [37]. Due to the induced compression and rarefaction, the waves travelling at high frequencies and pressures affect the density of the medium. Because the propagation speed of the wave is dependent on the density of the medium, the wave to travel faster during compression than rarefaction. This means that some parts of the wave travel faster than others. The resulting waveform is therefore distorted from its original state. Large enough variations (such as the ones cause by ultrasonic waves) lead to significant downshifts on the signal's center frequency [37] [38]. Not taking nonlinear effects into consideration leads to inaccurate pressure and temperature field calculations [25].

Small signal approximation will therefore have to be used in order to describe ultrasound with the fundamental equations just presented. These are shown in Eq. 5, where the subscript o, in this case, represents the reference, or ambient, value, which are constant over time and space.

$$P' = P - P_o, \rho' = \rho - \rho_o, T' = T - T_o, s' = s - s_o \quad \text{Eq. 5}$$

If these values are substituted into Eq. 1-Eq. 4, and only the second order terms or terms of higher order are collected, Eq. 6-Eq. 9 are obtained [37] [38]. In these equations, the first order terms are located in the left, while the second order terms are located in the right. Every third order term or higher is neglected

The reference parameters ρ_o , P_o , s_o and T_o are constant in space and time. Moreover, the vorticity terms produced by the curl of the velocity (which is obtained by using the vector

identities [39]) are discarded, leading to Eq. 7. The last viscosity terms in the entropy equation are discarded because they are very small compared to the conduction term. These are therefore neglected, which leads to Eq. 8. Finally, performing Taylor series expansion of the equation of state along the isentrope $s = s_o$ leads to Eq. 9, where the parameter $\frac{B}{A} = \left(\frac{\rho_o}{c_o^2}\right) \left(\frac{\partial^2 P}{\partial \rho^2}\right)$, accounts for the nonlinearity just mentioned. In this relationship, the parameter c_o [m/s] is the small signal sound speed.

$$\frac{\partial \rho'}{\partial t} + \rho_o \nabla \cdot \vec{u} = -\rho' \nabla \cdot \vec{u} - \vec{u} \cdot \nabla \rho' \quad \text{Eq. 6}$$

$$\rho_o \frac{\partial \vec{u}}{\partial t} + \nabla P' = \left(\mu_B + \frac{4}{3}\mu\right) \nabla^2 \vec{u} - \frac{1}{2}\rho_o \nabla \vec{u}^2 - \rho' \frac{\partial \vec{u}}{\partial t} \quad \text{Eq. 7}$$

$$\rho_o T_o \left(\frac{\partial s'}{\partial t}\right) = k \nabla^2 T' \quad \text{Eq. 8}$$

$$P' = c_o^2 \rho' + \frac{c_o^2}{\rho_o} + \frac{B}{2A} \rho'^2 + \left(\frac{\partial P}{\partial s}\right)_{\rho,0} s' \quad \text{Eq. 9}$$

An extensive combination of these equations leads to the main model used for ultrasonic wave propagation, in thermoviscous fluids, shown in Eq.10. A detailed derivation of these equations is shown in the literature [37] [38].

$$\nabla^2 P - \frac{1}{c_o^2} \frac{\partial^2 P}{\partial t^2} + \frac{\delta}{c_o^4} \frac{\partial^3 P}{\partial t^3} + \frac{\beta}{\rho_o c_o^4} \frac{\partial^2 P^2}{\partial t^2} + \left(\nabla^2 + \frac{1}{c_o^2} \frac{\partial^2}{\partial t^2} \right) \mathcal{L} = 0 \quad \text{Eq.10}$$

In this equation, β [-] is the coefficient of nonlinearity, and \mathcal{L} is the Lagrangian density [kg m s⁻²]. Moreover, the diffusivity of sound, δ [m²/s] is defined in Eq.11

$$\delta = \frac{2c_o^3 \alpha}{\omega_o^2}, \quad \omega_o = \frac{2\pi \lambda}{c_o} \quad \text{Eq.11}$$

In this equation, α [Np/m] is the acoustic absorption coefficient, which will be discussed in later sections, and ω_o [rad/s] is the angular frequency of the signal also defined, where λ is the signals wavelength.

The Lagrangian density is defined in Eq.12, where u [m/s] is the travelling velocity of the wave. Progressive waves use the linear relationship $P = c_o \rho_o u$ in order to describe the travelling velocity.

$$\mathcal{L} = \frac{1}{2} \rho_o u^2 - \frac{P^2}{2\rho_o c_o^2} \quad \text{Eq.12}$$

This relationship can be used only because the effect of this term is significantly small compared to the combined effect of the other terms of Eq.10 once the wave has travelled a distance much larger than its wavelength [38]. Using the linear relationship for P and substituting for u in Eq.12 leads to $\mathcal{L} = 0$, letting the last term in Eq.10 to be discarded. The results of this substitution is

also known as Westervelt model, shown in Eq.13, Several authors have used this model to develop numerical analyses for progressive plane waves [26] [33] [25] [40] [41].

$$\nabla^2 P - \frac{1}{c_o^2} \frac{\partial^2 P}{\partial t^2} + \frac{\delta}{c_o^4} \frac{\partial^3 P}{\partial t^3} + \frac{\beta}{\rho_o c_o^4} \frac{\partial^2 P^2}{\partial t^2} = 0 \quad \text{Eq.13}$$

Time can be redefined to make it relative to the position of an observer travelling at the speed of sound c_o , as shown in Eq.14.

$$\tau = t - \frac{x}{c_o} \quad \text{Eq.14}$$

Where τ [s] is the new time frame and x is the position relative to an observer in the old time frame t [s]. Burgers model, shown in Eq.15, assumes a one dimensional form of Eq.13 in the new time frame [38]. The reason for this new time frame deals with the simplification of analytical solutions.

$$\frac{\partial P}{\partial x} - \frac{\delta}{2c_o^3} \frac{\partial^2 P}{\partial \tau^2} - \frac{\beta P}{\rho_o c_o^3} \frac{\partial P}{\partial \tau} = 0 \quad \text{Eq.15}$$

The KZK model is a simpler derivation of Westervelt model with different time frames, following the same procedure as burgers model. It assumes large enough sources such that the wave described is almost completely directional and therefore a parabolic approximation can be applied [38]. This means that spatial variations in the direction of propagation, known as z , are perceived faster than the ones occurring at directions perpendicular to propagation, known as x

and y . This approximation makes the relationship between space and time, shown in Eq.14, applicable only for the propagation direction. Substitution of these values results in the model shown in Eq. 16 [38].

$$\frac{\partial^2 P}{\partial z \partial \tau} - \frac{c_0}{2} \nabla_{\perp}^2 P - \frac{\delta}{2c_0^3} \frac{\partial^3 P}{\partial \tau^3} - \frac{\beta}{\rho_0 c_0^3} \frac{\partial^2 P^2}{\partial \tau^2} \quad \text{Eq. 16}$$

In this equation, z is the coordinate of the direction of propagation, and ∇_{\perp} is shown in Eq. 17, which represents the Laplacian acting perpendicularly to the direction of propagation.

$$\nabla_{\perp} = \frac{\partial^2}{\partial x^2} + \frac{\partial^2}{\partial y^2} \quad \text{Eq. 17}$$

The KZK equation has been extensively used for developing numerical schemes of ultrasound beams [30] [27] [42] [28] [43] [44] [45].

The Westervelt model is the one used in this study. For planar sources, this model has been shown to be more accurate in the near field and locations far from the propagation axis [26]. Recent studies have shown that, for focused signals, its accuracy increases with increasing the wavenumber of the signal and the source size [46].

Transducer Theory

Transducers are used to convert one form of energy to another. In the case of ultrasound, electrical energy is converted into mechanical waves by making use of the piezoelectric effect.

Piezoelectric Effect and Transducer Devices

Piezoelectric crystals are subjected to a polarizing process where they are heated slightly and subjected to an electric current. This process gives the crystal a net dipole moment, and therefore a net polarization, as shown in Figure 3 (a) [47]. The polarization will be permanent as long as the crystal's temperature does not exceed a specific threshold temperature, also known as the Curie temperature [48].

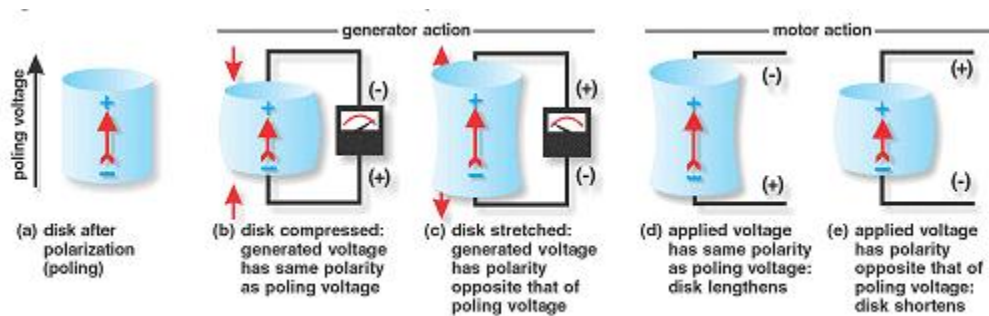


Figure 3 Piezoelectric effect (generator action) and inverse piezoelectric effect (motor action)
(Permission granted by APC International, Ltd.) [47]

Linking opposite charges and producing a strain in each face of a piezoelectric crystal (parallel to the direction of polarization) will generate a voltage [47]. This voltage will be the same one as the poling voltage if the crystal is compressed, as shown in Figure 3 (b), and opposite if the voltage is stretched, as shown in Figure 3 (c). This voltage generation is useful for some transducers that measure ultrasound signals, such as hydrophones.

Moreover, linking opposite charges into each faces of a piezoelectric crystal, and generating a voltage will produce a force [47]. The direction of this force can be either outwards or inwards,

depending on whether the induced and poling voltages are equal or opposite, respectively. The force will produce a strain on the crystal which will either make it compress or expand, as shown in Figure 3 (d) and (e) [47]. This is called the motor action and, in this case, it is the one used by the transducer that induces the ultrasound signal.

Transducers used for ultrasound applications are driven by an AC signal with specific frequency, voltage, and current. If an AC signal is applied, the transducer will vibrate at roughly the same frequency of the electric signal, and placing the transducer next to a medium will induce an ultrasonic signal within that medium [47].

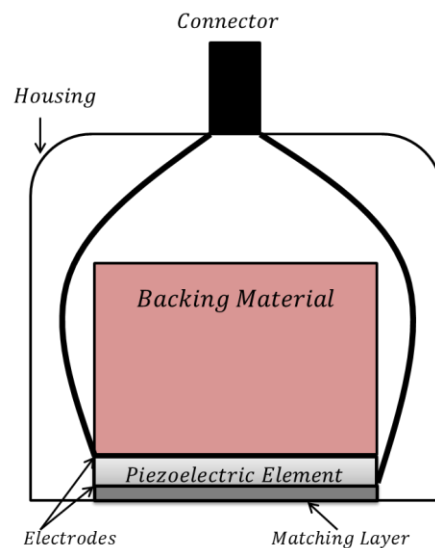


Figure 4 Diagram of a typical ultrasonic transducer [48]

Proper design of transducers is required to transform as much electrical energy into mechanical waves, directed to the desired location, as possible. Figure 4 shows the main components of a transducer [48]. The piezoelectric crystal is connected to an AC circuit through electrodes

attached to each face. The backing material prevents the crystal from radiating the signal through both of its faces. This makes the signal radiate only in the desired direction of propagation, increasing the overall efficiency of the transducer [48]. Matching layers, made out of different types of epoxy [48], decrease acoustic impedance between the crystal and the medium.

A lens is usually inserted in front of the matching layer in order to focus the ultrasonic signal on a specific point [48]. However, arrays of multiple transducers can be used instead of a lens in order to create a focusing point depending of the phase difference within them [49]. Moreover, transducers with concave geometries will also provide the same results.

Transducer Geometry and Signal Types

In this study, the two types of ultrasound signals of interest are the continuous wave (CW) and pulsed signals. These can be mathematically represented with a time dependent sinusoidal function, as shown in Eq. 18, where ω_o [rad/s] is the monochromatic (center) angular frequency of the signal, and t is the time [s].

$$f(t) = \sin(\omega_o t) \quad \text{Eq. 18}$$

The main difference between both signals is the dependence of amplitude in time. A continuous signal is represented with Eq. 19. In this equation, P_o [MPa] is the prescribed source pressure amplitude and it is always constant for this type of signal. An envelope function, shown in Eq. 20, is used to describe a pulsed signal [50], where n is the number of cycles of the signal and it

represents the signal's active time. The value m dictates the waveform, or how steep the envelope will be. A value of 1 for m is used to describe Gaussian shaped pulses; moreover, a value of ∞ describes rectangular envelope pulses [51]. These equations are illustrated in Figure 5, where they are plotted with respect to time.

$$P = P_o f(t) \tag{Eq. 19}$$

$$P = P_o e^{-\left(\frac{\omega_o t}{n\pi}\right)^{2m}} f(t) \tag{Eq. 20}$$

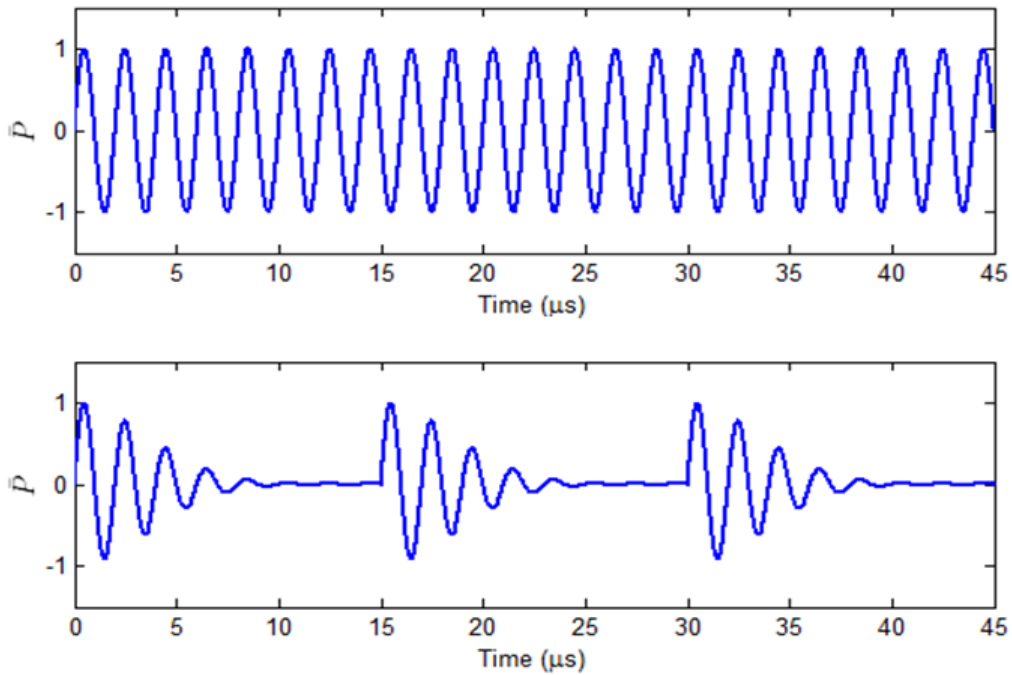


Figure 5 Top: Pressure vs. time for continuous wave (CW) signal described by Eq. 19 Bottom: Pressure vs. time for pulsed signal described by Eq. 20 for $n = 5$ and $m = 2$

How frequently the pulsed signals are delivered is important for many applications and it is considered to be a variable called the duty factor (DF) [37], given in Eq. 21. It represents the percentage of the signal's active time T_o [s] with respect to the total time between pulses T_{tot} [s].

$$DF = \frac{T_o}{T_{tot}} ; T_o = \frac{n\pi}{\omega_o} \quad \text{Eq. 21}$$

There is a wide variety of transducer geometries and their use depends on the application. The two main geometries to be studied are planar and focused transducers, which are shown in Figure 6. The transducer radius R_s and the radius of curvature φ are important variables that affect the pressure gain at the focal point.

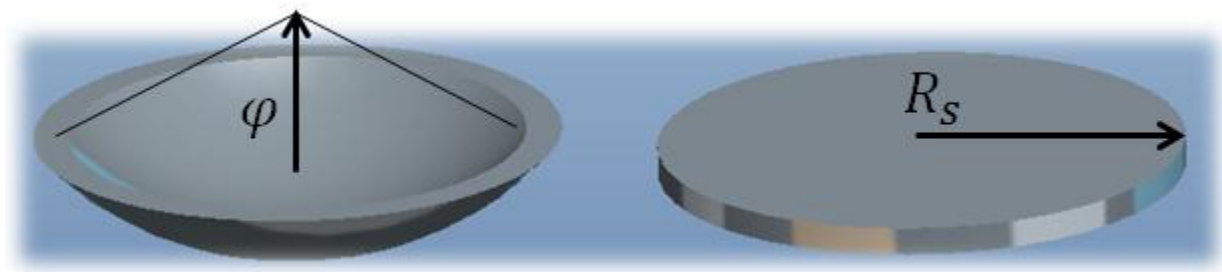


Figure 6 Transducer geometries to be studied: focused (left) and planar (right) disk transducers

Other geometric parameters for focused transducers are shown in Figure 7. These are important for proper mathematical modeling of the signal driven by this source. The parameter ϵ [m] is the distance from the source plane to the location of the focal point, h [m] is the rim height of the transducer, and θ [°] is the half-angle of aperture. These are calculated with trigonometric relationships using the known transducer radius R_s and radius of curvature φ values.

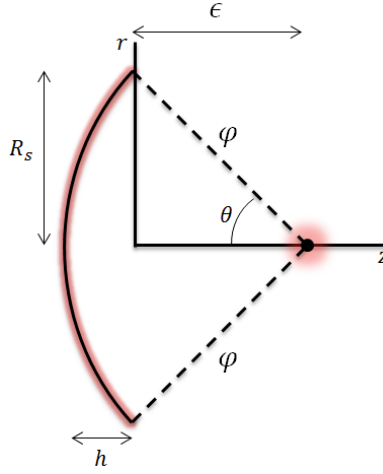


Figure 7 Schematic of focused transducer with its respective geometric parameters

The phase distribution required in the source plane for the signal to converge at $z = \epsilon$ is given by Eq. 22, which represents a continuous wave (constant amplitude with respect to time) [38]. The symbol z_{fp} represents the distance starting from a certain location in the transducer face to the location of the focal point ϵ , shown in Eq. 23.

$$P = \frac{\varphi}{z_{fp}} P_o f \left(t + \frac{(z_{fp} - \varphi)}{c_o} \right) \quad \text{Eq. 22}$$

$$z_{fp} = \sqrt{r^2 + \epsilon^2} \quad \text{Eq. 23}$$

Pulsed signals for focused transducers are modeled by Eq. 24. This equation is obtained by recalling the envelope pressure amplitude characteristic already discussed.

$$P = \frac{\varphi}{z_{fp}} P_o e^{-\left(\frac{\omega_o \left(t + \frac{(z_{fp} - \varphi)}{c_o} \right)}{n\pi} \right)^{2m}} f \left(t + \frac{(z_{fp} - \varphi)}{c_o} \right) \quad \text{Eq. 24}$$

The accuracy of the KZK and Westervelt equation heavily depend on the aperture angle θ because they carry important assumptions. Westervelt Equation ignores local effects and the KZK equation is a parabolic approximation of the Westervelt Equation, as discussed before [38]. An aperture angle θ of 20° is said to be the limit of validity for the KZK equation [52] [53]. According to studies, the Westervelt equation is a fair approximation of the nonlinear acoustic field resulting from geometrically focused signals with sufficiently big source radii [46]. There are other models developed with the sole purpose of explaining this focal shift in terms of either the aperture angle or the linear gain (which will be explained in further sections) [29].

Experimental Methods for Simulating Pressure Fields

Simulating the pressure field in a medium induced by an ultrasonic signal has been done numerous times in the past. The models just discussed have been validated with experimental results, usually by comparing the experimental data with one obtained with numerical methods [26] [33] [54] [30] [55] [32] [34] [56].

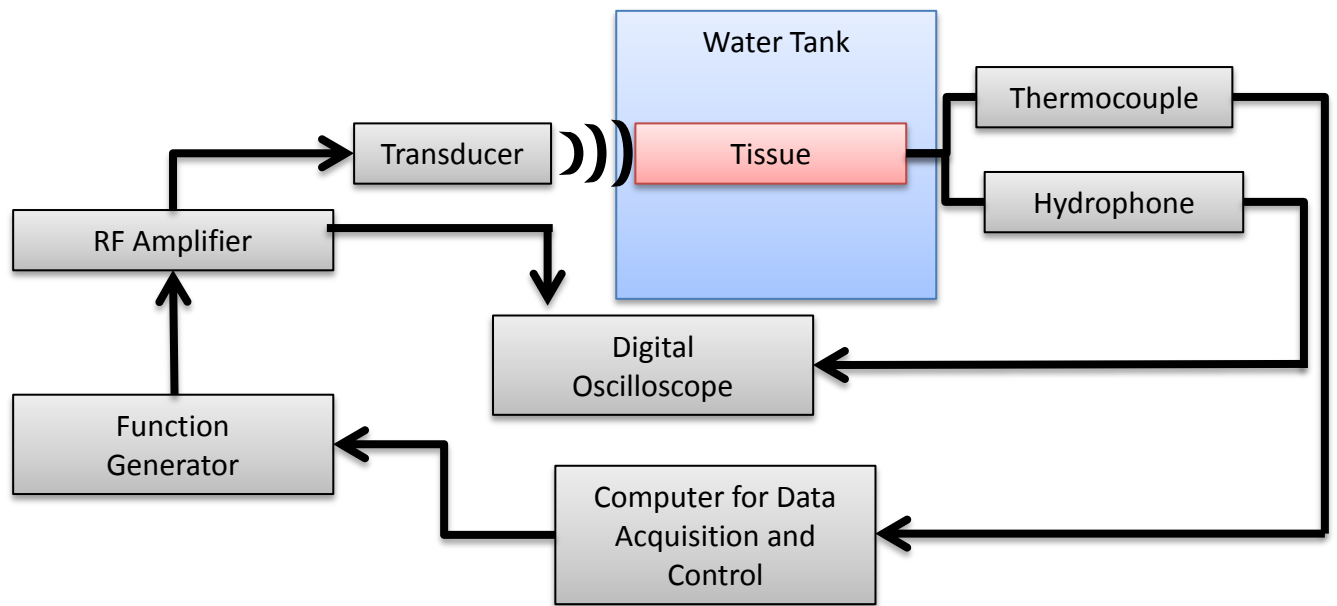


Figure 8 Schematic of generic ultrasound experiment

Figure 8 shows the general setup for experiments involving ultrasound. A function generator is in charge of delivering the signal. The amplifier will increase the overall power of this signal, which will be delivered to the oscilloscope in order for the operator to check that its properties are correct.

The amplifier also sends a signal to the transducer, which is in charge of converting it into mechanical power, as already discussed. This mechanical power is in the form of pressure waves with both prescribed frequency and pressure amplitudes. The geometry of the transducer will dictate the direction of these waves. They will be delivered to the sample, which is generally tissue, or tissue mimicking material, located in a water tank.

A needle hydrophone and a needle thermocouple measure the resulting pressure and temperature at their respective position. These are inserted from the back in order to make the measurements without intervening in the process. The needle hydrophone sends the signal to the oscilloscope for evaluation and comparison. The thermocouple sends a signal that has to be conditioned and eventually acquired by the data acquisition system.

The reason behind the use of this setup is that water and tissue share very similar acoustic properties. The advantage of using tissue or tissue mimicking materials is that the volume of ablated tissue can be measured at the end of the experiment. However, water can be used if only the pressure field is being calculated [26].

A disadvantage of this experimental procedure is that both the hydrophone and the thermocouple make their measurements only at a certain location in space. Usually the data is taken at points along the axis of propagation, or only at the focal point [26] [28] [32].

Intensity and Heat Generation

As discussed before, the energy of an ultrasonic wave, described by the pressure amplitude, will eventually start decaying as it travels through absorbing media. The intensity of a collimated, plane harmonic wave travelling in a direction x , I [W m^{-2}] decays exponentially [37], as shown in Eq. 25.

$$I(x) = I_0 e^{-2\mu x} \quad \text{Eq. 25}$$

Where I_0 is the reference intensity when $x = 0$, and μ is the amplitude attenuation coefficient per unit length. This attenuation can be either a product of signal scattering, due to aberrations in the medium, or signal absorption. In this case, it is assumed that there are no aberrations due to the uniform properties of the medium. The amplitude attenuation coefficient will be therefore considered to be the power-law frequency dependent absorption coefficient α_o . The absolute absorption coefficient α is shown in Eq. 26 [38]. The absolute absorption coefficient can be plotted along with frequency in order to obtain η [37]□.

$$\alpha = \alpha_o f^\eta \quad \text{Eq. 26}$$

Volumetric heat generation \dot{Q} [W/m³] is obtained by differentiating the intensity along the axis of propagation, as shown in Eq. 27 [37] [38].

$$\dot{Q} = -\frac{\partial I}{\partial x} = 2\alpha I_0 e^{-2\alpha x} = 2\alpha I(x) \quad \text{Eq. 27}$$

The intensity [W m⁻²] of a regular wave depends on its pressure P and velocity u , as shown in Eq. 28. It is instantaneous and varies with time.

$$I = Pu \quad \text{Eq. 28}$$

It is useful to use the first order approximation $P/\rho_o c_o = u$ for progressing waves [38], which was already used to eliminate the Lagrangian term of Eq.10. The approximation makes Eq. 28 dependent on pressure only. If the root-mean squared pressure is computed, it can be used to find the time-averaged intensity, shown in Eq. 29. Suitable averaging times $t_2 - t_1$ depend on the

type of signal, its frequency, nonlinearity levels, pressure amplitude, etc. [37]. The times t_1 and t_2 will be analyzed and its value will be discussed in further sections

$$I = \frac{P_{rms}^2}{\rho_o c_o}, \quad P_{rms} = \sqrt{\frac{1}{t_2 - t_1} \int_{t_1}^{t_2} P^2 dt} \quad \text{Eq. 29}$$

Temperature Analysis

The main models that will be used in this study will differ by either the inclusion or exclusion of the tissue's ability to dissipate the heat generated via convective means. Natural convection and forced convection due to blood flowing through the vascular regions will be explained below.

Figure 9 shows a schematic of biological soft tissue (not applied to bone), where the vascular region is the region where blood flows in and out. This will disperse the heat generated by ultrasound in the extravascular region.

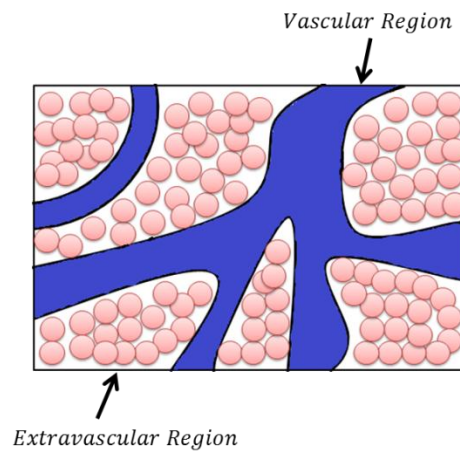


Figure 9 Schematic view of biological soft tissue [57]

Each of the vascular and extravascular regions has its specific control volume, where heat and mass are transferred in and out. The representation of this medium can be simplified by assuming that the vascular region is comprised of micro channels with uniform spacing and identical diameter. Figure 10 shows this assumption, illustrating that the ratio of the volume occupied by the extravascular region V_{EV} and the volume occupied by the vascular region V_V stays constant for large volumes.

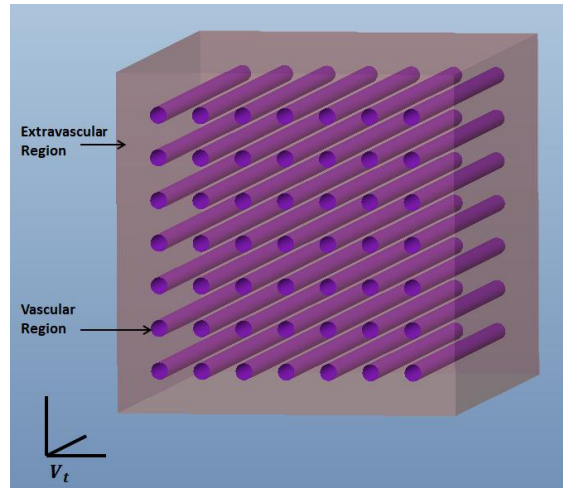


Figure 10 Simplified Schematic View of Biological Tissue

This ratio is also known as porosity ϵ (not to be confused with the focal point distance of a focused transducer ϵ) and it has been used for the development of many models as an important variable to couple the separate energy equations (one each for the extravascular and vascular regions [57] [58]), shown in Eq. 30 and Eq. 31.

$$\rho_b c_{pb} \left(\epsilon \frac{\partial T_b}{\partial t} + u_b \frac{\partial T_b}{\partial z} + w_b \frac{\partial T_b}{\partial r} \right) = \frac{1}{r} \frac{\partial}{\partial r} \left(\epsilon k_b r \frac{\partial T_b}{\partial r} \right) + \frac{\partial}{\partial z} \left(\epsilon k_b \frac{\partial T_b}{\partial z} \right) - a_{bT} h_{bT} (T_b - T_T) - c_{pb} W_b (T_b - T_T) \quad \text{Eq. 30}$$

$$\rho_T c_{pT} (1 - \varepsilon) \frac{\partial T_T}{\partial t} = \frac{1}{r} \frac{\partial}{\partial r} \left((1 - \varepsilon) k_T r \frac{\partial T_T}{\partial r} \right) + \frac{\partial}{\partial z} \left((1 - \varepsilon) k_T \frac{\partial T_T}{\partial z} \right) + \dot{Q} + a_{bT} h_{bT} (T_b - T_T) + c_{pb} W_b (T_b - T_T) \quad \text{Eq. 31}$$

These equation are shown for axisymmetric conditions to fit this study (which will be discussed in later sections), T is the temperature [$^{\circ}\text{C}$], ρ is the density [kg m^{-3}], c_p is the specific heat capacity [$\text{J kg}^{-1} \text{K}^{-1}$], k is the thermal conductivity constant [$\text{W K}^{-1} \text{m}^{-1}$], \dot{Q} is the volumetric rate of heat generation [W m^{-3}], u and w are the velocities in each the propagation and radial direction respectively [m/s], a is the volumetric area [$\text{m}^2 \text{m}^{-3}$], h is the coefficient of convection [$\text{W K}^{-1} \text{m}^{-2}$] and W is the perfusion coefficient [$\text{kg m}^{-3} \text{s}^{-1}$]. The subscripts b and T denote the vascular (blood) and the extravascular (tissue) regions.

Eq. 30 (being the energy conservation model for fluids) includes heat dissipation by advection, while Eq. 31 (being the energy conservation model for solids) does not. Both of these terms include heat transfer by the interphase between the vascular and extravascular (second to last term) and by perfusion (last term). However, it can be seen that they have opposite signs for these two terms. The difference between the following models, which are simpler versions of these models, is the way these two terms are treated.

The most general energy conservation model for biological media is the Pennes bioheat model [59]. This model assumes that the temperature of the blood at the vascular region T_b and the extravascular region T_T are equal [57]. It also assumes that the parameters for each are equal or can be averaged.

The heat dissipation by advection, perfusion, and transfer at the interphase is also substituted by a new perfusion term which refers to blood coming in and out of the entire domain of interest (as opposed to the blood inside of the domain, which has the same temperature as the tissue).

$$c_{pb}W_{pennes}(T_{\infty} - T) = a_{bT}h_{bT}(T_b - T_T) + c_{pb}W_b(T_b - T_T) \quad \text{Eq. 32}$$

It can be seen that the new perfusion coefficient W_{pennes} and reference temperature T_{∞} attempt to approximate the combination of the old perfusion and transfer at the interphase as an exchange to assuming that $T_b = T_T = T$. The Pennes model is shown in Eq. 33, where T_{∞} is the temperature of blood which comes in and out of the region of interest, not to be confused with T_b .

$$\frac{1}{r} \frac{\partial}{\partial r} \left(kr \frac{\partial T}{\partial r} \right) + \frac{\partial}{\partial z} \left(k \frac{\partial T}{\partial z} \right) + \dot{Q} + c_{pb}W_{pennes}(T_{\infty} - T) = \rho_o c_p \frac{\partial T}{\partial t} \quad \text{Eq. 33}$$

The heat generation term couples the pressure and temperature analyses together. Also, the heat will either be diffused by conduction or forced convection will be stored. This energy storage will in turn raise the overall temperature of the medium.

As mentioned before, porous media dissipates heat in other ways that might not be described by Eq. 33. Therefore, inclusion of the viscous dissipation and natural convection (in the extravascular region) in this energy conservation model is needed. If the terms of conduction and energy storage are neglected from Eq. 30, then Eq. 34 is obtained.

$$\rho_b c_{pb} \left(u_b \frac{\partial T_b}{\partial z} + w_b \frac{\partial T_b}{\partial r} \right) = -a_{bT} h_{bT} (T_b - T_T) - c_{pb} W_b (T_b - T_T) \quad \text{Eq. 34}$$

Substituting this equation into Eq. 31, while including a viscous dissipation term leads to Eq. 35.

This equation makes the same assumptions as the Pennes model, but it does not approximate the heat dissipation by perfusion. It includes heat dissipation by conduction, viscosity, and advection. It has to be noted that the advection and viscous dissipation corresponds to the blood flowing within the extravascular region.

$$\frac{1}{r} \frac{\partial}{\partial r} \left(kr \frac{\partial T}{\partial r} \right) + \frac{\partial}{\partial z} \left(k \frac{\partial T}{\partial z} \right) + \dot{Q} + \frac{\mu}{K} (u_b^2 + w_b^2) = \rho_o c_p \left(\frac{\partial T}{\partial t} + u_b \frac{\partial T}{\partial z} + w_b \frac{\partial T}{\partial r} \right) \quad \text{Eq. 35}$$

This model resembles the Klinger model [60], with the difference that it includes a viscous heat dissipation term. Calculating these velocities is the main issue with this equation. In this study, the use of Darcy's theory for flow transport in porous media [61] and the Boussinesq approximation [62] is used. The Darcy flow can be expressed as shown in Eq. 36 where μ is the viscosity of blood [$\text{kg s}^{-1} \text{m}^{-1}$], and K is the permeability constant [m^2].

$$\vec{U} = -\frac{K}{\mu} \nabla P \quad \text{Eq. 36}$$

It has to be noted that this is not the same pressure gradient as the one induced by the ultrasonic beam. It is assumed that the ultrasound generated pressure only influences the porous medium and not the fluid inside it (in this case, the blood). The pressure shown in Eq. 36 is the one needed to create a flow of the blood with a certain velocity \vec{U} inside the extravascular region.

The permeability constant K dictates the ability for a fluid to flow through the porous media. It happens exclusively in the extravascular region and might dissipate significant amounts of heat in the form of natural (not forced) convection.

In other words, the velocity of this flow is not the same as the one experienced by the vascular region and is not related to heat dissipation by perfusion, but by the tissues permeability and the pressure gradient.

Although it might be possible that this pressure gradient is dependent on the ultrasound beam by acoustic streaming, it is neglected in this study. The main factor to be studied is thus the pressure gradient caused by buoyancy.

The importance of buoyancy driven flow will be tested by checking if natural convection is an important heat dissipation agent in ultrasound. If it is assumed that the ultrasound signal is being propagated upwards, gravity will be considered only in the negative z direction.

Breaking down Eq. 36 into its cylindrical components leads to Eq. 37. The value ρg corresponds to the body forces experienced by the blood.

$$\vec{U}_b = w_b \hat{r} + 0 \hat{\theta} + u_b \hat{z} = -\frac{K_b}{\mu_b} \left(\frac{\partial P}{\partial r} \hat{r} + 0 \hat{\theta} + \left(\frac{\partial P}{\partial z} - \rho g \right) \hat{z} \right) \quad \text{Eq. 37}$$

If the curl of the velocity is taken, the pressure terms will disappear and the only term that will be a factor is the change of the blood density due to changes in temperature. As shown in Eq. 38.

$$\nabla \times \vec{U}_b = \frac{\partial w_b}{\partial z} - \frac{\partial u_b}{\partial r} = -\frac{K_b g}{\mu_b} \frac{\partial \rho_b}{\partial r} \hat{\theta} \quad \text{Eq. 38}$$

The relationship between the change in blood density and temperature is described by Boussinesq approximation [62]. This is shown in Eq. 39, where β is the coefficient of thermal expansion of the porous medium [1/K].

$$(\rho - \rho_\infty) \approx \rho \beta (T - T_\infty) \quad \text{Eq. 39}$$

The buoyancy driven flow of the blood can therefore be described by Eq. 40

$$\frac{\partial w_b}{\partial z} - \frac{\partial u_b}{\partial r} = -\frac{K g \rho_b \beta}{\mu} \frac{\partial T}{\partial r} \quad \text{Eq. 40}$$

Proper analysis of the Pennes model and this version of the Klinger model, exclusively for ultrasound induced heat generation, has never been inspected. Therefore, there is no conclusion on which of these terms plays a significant role in heat dissipation occurring during the signal delivery.

Chapter 3: Numerical Scheme

Numerical methods offer an attractive option for analyzing ultrasonic signals because they are relatively inexpensive and a wide range of results can be obtained. This study uses numerical methods in order to develop proper, simpler, coupled models of the relationship between delivered dosages and resulting temperature rises due to heat generation

Modeling

The results from the numerical analysis have to be validated with experimental methods. It is therefore required that the model to be used resembles the general experimental setup already shown in Figure 8.

Schematic

The model for the numerical analysis will follow the schematic shown in Figure 11, which illustrates the top view of a transducer delivering an ultrasonic pulse to a medium of interest. This medium will have the same acoustical and thermal properties as tissue. It is assumed that these are uniform and do not change with time.

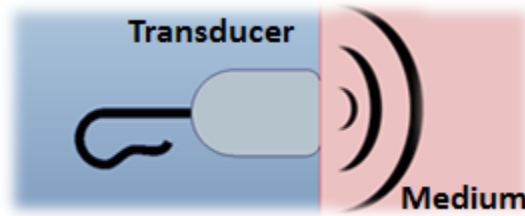


Figure 11 Schematic of a transducer delivering an ultrasound signal to a certain medium

It is also assumed that the pulse does not experience any obstacles upon its path. This means that it should be completely absorbed just by travelling throughout the medium. The boundaries would therefore be considered semi-infinite since the pulse will not reach the end. Not considering this would mean that the pulse might bounce back upon reaching the boundaries.

Geometry

Given these assumptions, it is valid to model the signal propagation as being symmetric with respect to a certain axis (as long as the source is symmetric too). The transducer is modeled as a disk concentric and internally adjacent to an axisymmetric cylinder, which represents the medium the signal travels upon, as shown in Figure 12. Because of its axisymmetry, results across the circumferential direction will be identical, so the coordinate θ can therefore be ignored. Therefore, only the radial coordinate r and the propagation coordinate z are needed. The size of this cylinder will be dictated by the parameters L and R , representing the propagation and radial distance, respectively. The choice of these parameters will be discussed in further sections.

The transducer will be modeled with either Eq. 19, Eq. 20, Eq. 22, or Eq. 24, depending on its geometry.

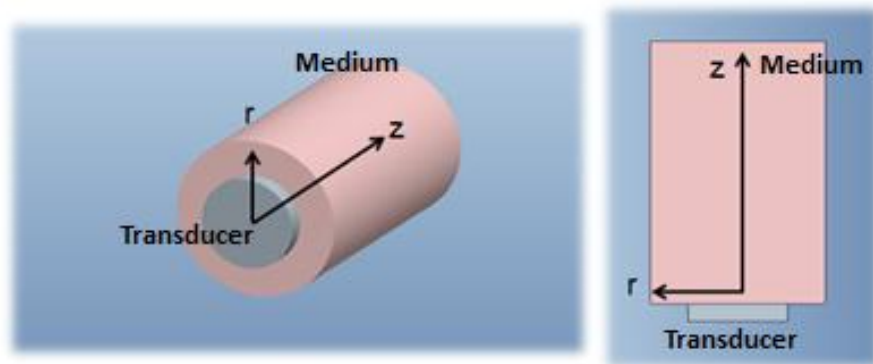


Figure 12 Left: Representation of Medium as an Axisymmetric Cylinder; Right: Cylinder's Radial and Propagation Coordinates r and z , respectively

The signal travels mainly in the propagation direction and it will be simulated until it is about to hit the boundaries. The boundaries have greater absorptive properties than the rest of the medium in order to symbolize semi-infinite media [25] [51], and they also are going to be described with ideally soft boundary conditions [63], which will be explained in further sections. There is a symmetry boundary condition at $r=0$ due to the axisymmetric geometry of the problem.

The main disadvantage of using this coordinate system is the lack of freedom when choosing the geometry of the transducer. Only perfectly symmetrical sources can be applied (piston and focused disk, as well as annulus transducers). Regardless, the complexity of the analysis is greatly reduced.

The overall length and radius of the medium should be optimized to be as minimal as possible in order to reduce the computational expense of the analysis. However, these dimensions should represent semi-infinite media and there is a minimum threshold value that provides enough

accuracy to do so. The threshold value depends on the source radius and the frequency of the signal and it will be discussed along with the choice of proper boundary conditions.

Finite Difference Methods

A wide variety of studies have used finite difference methods in the time domain to develop numerical models of ultrasound [25] [26] [64] [33] [54] [31]. The equations that were chosen to model ultrasound signal propagation, temperature, and tissue response can be discretized in space and time with the use of Taylor series.

The spatial domain is going to be composed of a grid with a finite set of nodes. These are identified with the index values of i and j for the propagation and the radial coordinates, respectively. The maximum number of nodes in the i and j direction are referred as i_{max} and j_{max} , respectively, as shown in Figure 13. It can also be seen that each node is separated by a distance Δr and Δz in the radial and propagation directions, respectively. Every node has a value for pressure $P_{i,j}^n$, temperature $T_{i,j}^n$, stream function $\psi_{i,j}^n$, and survival percentage $S_{i,j}^n$ at a certain time $t = n \Delta t$, where n is the iteration number.

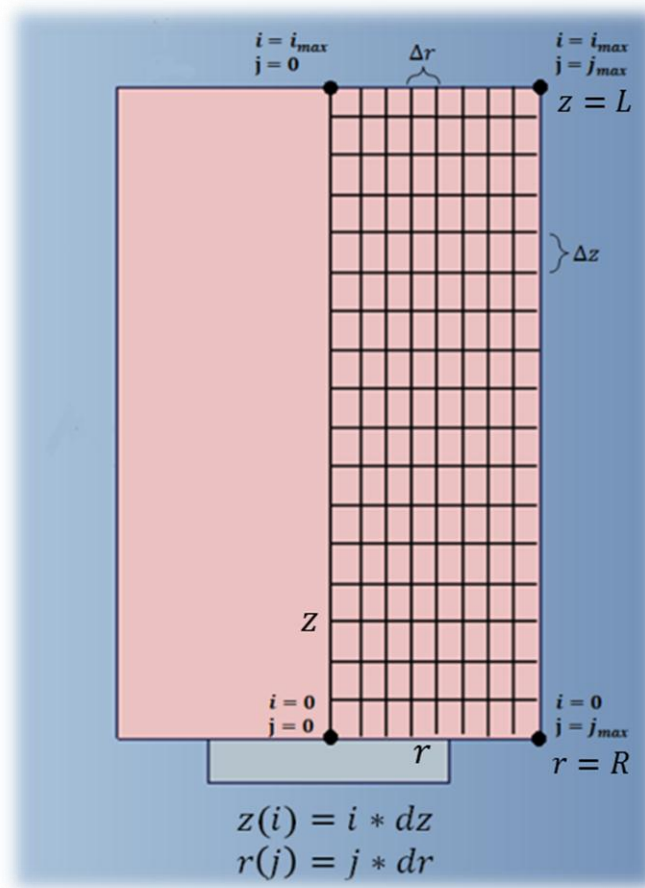


Figure 13 Schematic of the spatial grid used

Pressure and temperature are solved for the entire spatial field for several iterations. The number of iterations multiplied by the time step used Δt results in the total time.

Pressure Field Discretization

The first equation that is going to be approximated is the Westervelt Equation, which its terms have been separated into the time term of the D'alembertian, the absorptivity term, and the nonlinear term, shown in Eq. 41, Eq. 42, and Eq. 43 respectively.

Discretization for the spatial part of the D'alembertian term is going to depend on the location of the node (interior region, at the boundaries, etc.). The time dependent terms are therefore going to be considered first. The time dependent portion of the D'alembertian term was discretized using a central, second order difference, as shown in Eq. 41.

$$-\frac{1}{c_o^2} \frac{\partial^2 P}{\partial t^2} = -\frac{1}{c_o^2} \left[\frac{P_{i,j}^{n+1} + P_{i,j}^{n-1} - 2P_{i,j}^n}{\Delta t^2} \right] \quad \text{Eq. 41}$$

The diffusivity term was discretized using a backwards, second order difference, as shown in Eq. 42

$$\frac{\delta}{c_o^4} \frac{\partial^3 P}{\partial t^3} = \frac{\delta}{c_o^4} \left[\frac{3P_{i,j}^{n+1} - 10P_{i,j}^n + 12P_{i,j}^{n-1} - 6P_{i,j}^{n-2} + P_{i,j}^{n-3}}{2\Delta t^3} \right] \quad \text{Eq. 42}$$

The nonlinear term requires further approximation due to it having a squared value for P . The procedure has to be broken up into parts as shown in Eq. 43. The chain rule is used to take the first derivative of P^2 , followed by the product rule in order to take the second derivative. All the terms of the right hand side of Eq. 43 can be discretized.

$$\frac{\beta}{\rho_o c_o^4} \frac{\partial^2 P^2}{\partial t^2} = \frac{\beta}{\rho_o c_o^4} \frac{d}{dt} \left[2P \frac{dP}{dt} \right] = \frac{2\beta}{\rho_o c_o^4} \left[\frac{dP}{dt} \frac{dP}{dt} + P \left(\frac{d^2 P}{dt^2} \right) \right] \quad \text{Eq. 43}$$

One of the identical first order derivatives is going to be approximated with central difference in the second order, while the other one will be approximated with backwards difference in the second order. The second derivative shown in the second term will be approximated similarly to as it was done before for Eq. 41. The result is displayed in Eq. 44.

$$\frac{\beta}{\rho_o c_o^4} \frac{\partial^2 P^2}{\partial t^2} = \frac{2\beta}{\rho_o c_o^4} \left[\left(\frac{P_{i,j}^{n+1} - P_{i,j}^{n-1}}{2\Delta t} \right) \left(\frac{3P_{i,j}^n - 4P_{i,j}^{n-1} + P_{i,j}^{n-2}}{2\Delta t} \right) + P_{i,j}^n \left(\frac{P_{i,j}^{n+1} + P_{i,j}^{n-1} - 2P_{i,j}^n}{\Delta t^2} \right) \right] \quad \text{Eq. 44}$$

Substituting Eq. 41, Eq. 42, and Eq. 43 into Eq.10 will result in a completely linear equation that must be solved explicitly for $P_{i,j}^{n+1}$, provided that the values for $P_{i,j}^n, P_{i,j}^{n-1}$, etc. are known. It is analogous to say that the pressure field obtained for every point in time (the number of iterations n multiplied by the time step Δt). The resulting equation upon solving for $P_{i,j}^{n+1}$ is shown in Eq. 45.

$$P_{i,j}^{n+1} = \left(\frac{1}{c_o^2 \Delta t^2} - \frac{\beta}{\rho_o c_o^4 \Delta t^2} \left(\left(\frac{3P_{i,j}^n - 4P_{i,j}^{n-1} + P_{i,j}^{n-2}}{2} \right) + 2P_{i,j}^n \right) - \frac{3\delta}{2\Delta t^3 c_o^4} \right)^{-1} \left(\nabla^2 P - \frac{1}{c_o^2} \left[\frac{P_{i,j}^{n-1} - 2P_{i,j}^n}{\Delta t^2} \right] + \frac{\delta}{c_o^4} \left[\frac{-10P_{i,j}^n + 12P_{i,j}^{n-1} - 6P_{i,j}^{n-2} + P_{i,j}^{n-3}}{2\Delta t^3} \right] + \frac{2\beta}{\rho_o c_o^4} \left[-\frac{P_{i,j}^{n-1}}{2\Delta t} \left(\frac{3P_{i,j}^n - 4P_{i,j}^{n-1} + P_{i,j}^{n-2}}{2\Delta t} \right) + P_{i,j}^n \left(\frac{P_{i,j}^{n-1} - 2P_{i,j}^n}{\Delta t^2} \right) \right] \right) \quad \text{Eq. 45}$$

The Laplacian has to be defined differently for different regions of the grid. The interior points use a central difference scheme in the fourth order. It has been proven that the use of fourth order derivative approximations reduce numerical dispersion [25], which are shown in Eq. 46, Eq. 47, and Eq. 48.

$$\frac{d^2 P}{dz^2} = \frac{-P_{i-2,j}^n + 16P_{i-1,j}^n - 30P_{i,j}^n + 16P_{i+1,j}^n - P_{i+2,j}^n}{12\Delta z^2} \quad \text{Eq. 46}$$

$$\frac{d^2P}{dr^2} = \frac{-P_{i,j-2}^n + 16P_{i,j-1}^n - 30P_{i,j}^n + 16P_{i,j+1}^n - P_{i,j+2}^n}{12\Delta r^2} \quad \text{Eq. 47}$$

$$\frac{dP}{dr} = \frac{P_{i,j-2}^n - 8P_{i,j-1}^n + 0P_{i,j}^n + 8P_{i,j+1}^n - P_{i,j+2}^n}{12\Delta r} \quad \text{Eq. 48}$$

Substituting these equations for the Laplacian leads to the results shown in Eq. 49. It has to be noted that these equations are specifically for interior points only. In other words, they are used for every i between 3 and $imax-2$ and every j between 3 and $jmax-2$.

$$\begin{aligned} \nabla^2 P &= \frac{\partial^2 P}{\partial z^2} + \left(\frac{1}{r} \frac{\partial P}{\partial r} + \frac{\partial^2 P}{\partial r^2} \right) \\ &= \left(\frac{-P_{i-2,j}^n + 16P_{i-1,j}^n - 30P_{i,j}^n + 16P_{i+1,j}^n - P_{i+2,j}^n}{12\Delta z^2} \right) \\ &\quad + \frac{1}{r_j} \left(\frac{P_{i,j-2}^n - 8P_{i,j-1}^n + 0P_{i,j}^n + 8P_{i,j+1}^n - P_{i,j+2}^n}{12\Delta r} \right) \\ &\quad + \left(\frac{-P_{i,j-2}^n + 16P_{i,j-1}^n - 30P_{i,j}^n + 16P_{i,j+1}^n - P_{i,j+2}^n}{12\Delta r^2} \right) \end{aligned} \quad \text{Eq. 49}$$

The source terms for a transducer of radius R_s are defined in Eq. 19, Eq. 20, Eq. 22, and Eq. 24.

They are used to calculate the pressure $P_{1,j}^n$ where $j = 0, \dots, R_s/\Delta r$ (provided $R_s/\Delta r$ is an integer).

The equations used for the derivatives in the propagation direction z , for the nodes with i values of 2 and j values between 3 and $jmax-2$, are approximated by a quasi-forward difference scheme in the fourth order, shown in Eq. 50. The derivatives in the radial direction are approximated by a central difference scheme in the fourth order that was already described by Eq. 47 and Eq. 48

$$\frac{d^2 P}{dz^2} = \frac{-10P_{i-1,j}^n - 15P_{i,j}^n - 4P_{i+1,j}^n + 14P_{i+2,j}^n - 6P_{i+3,j}^n + P_{i+4,j}^n}{12\Delta z^2} \quad \text{Eq. 50}$$

The nodes with i values of $imax-1$ and j values between 3 and $jmax-2$, as well as the ones with i values between 3 and $imax-2$ and j values of either 2 or $jmax-1$, will be considered as being semi-infinite boundaries, which will be discussed in the further section

Pressure Field Boundary Conditions

As discussed before, a symmetry condition is going to be applied at the region for all z and where $r = 0$. This requires that, along the axis of propagation, the radial pressure gradient $\partial P / \partial r = 0$ [25] [63]. In order to obtain the value for $P_{i,1}^n$ and $P_{i,2}^n$, a central scheme has to be used where the hypothetical values for j that do not exist (of either negative value or 0) are substituted by values for the dummy index value j' . This domain acts as a mirror in order to keep the domain symmetric in this region as shown in Eq. 51 and Figure 14.

$$P_{i,j}^n = P_{i,j'}^n \quad \text{Eq. 51}$$

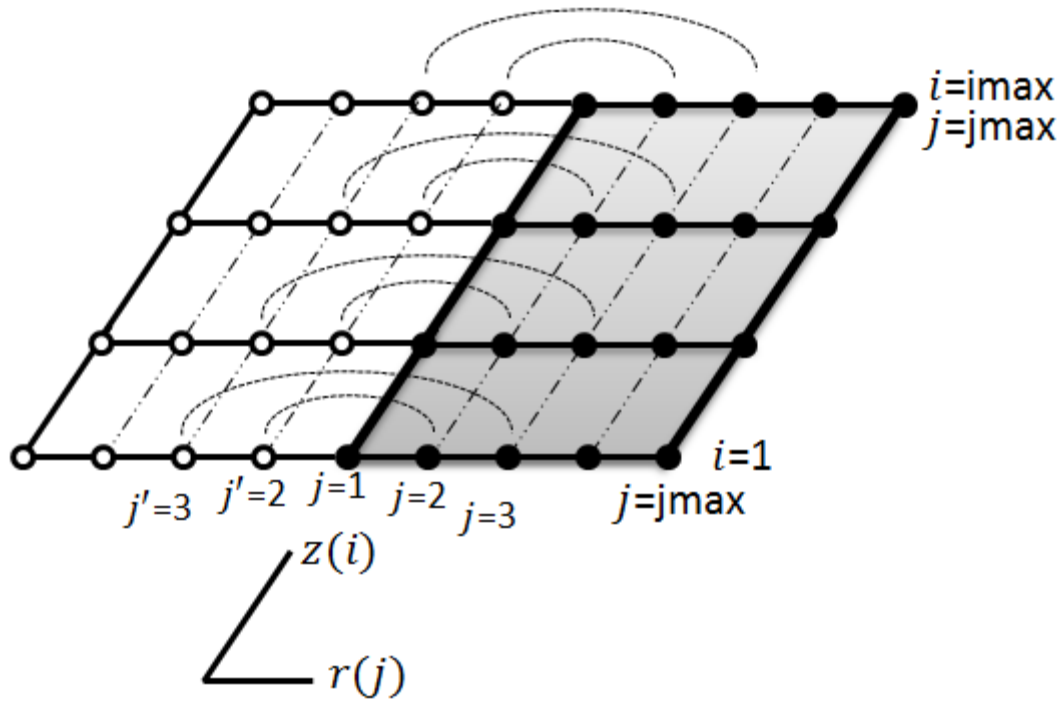


Figure 14 Illustration of the method used to define the symmetry boundary for all z when $r=0$

The values prescribed for all r between 0 and R_s at $z = 0$ depend on the type of source and signal used. The mathematical models for these are shown from Eq. 19 through Eq. 24. Time must be expressed using the number of iterations performed and the time step Δt . The values prescribed for all values of r greater than the source radius R_s rely on the assumption that the transducer is surrounded by a perfectly compliant baffle. These are therefore zero and they stay constant over time [26].

As stated before, the outer boundaries are supposed to act as semi-infinite media. These have to be carefully manipulated in order to avoid unwanted reflections. Many methods for manipulating these boundaries have been developed [65] [66] [67] [68] [69]. The usual method involves the use of absorbing boundary conditions (ABCs). They are developed by increasing the absorptive

properties of the medium at the outer regions, for faster wave attenuation, as shown in both graphs of Figure 15 [26] [33] [31] [25]. These properties start increasing at a distance equal to 80% of the total propagation and radial dimensions of the medium.

The data obtained at the boundaries, where the absorptive properties have been increased, is simulating semi-infinite media and it is therefore of no interest whatsoever. It can be assumed that accurate data will be obtained at the main regions of interest (focal point, near field, etc.)

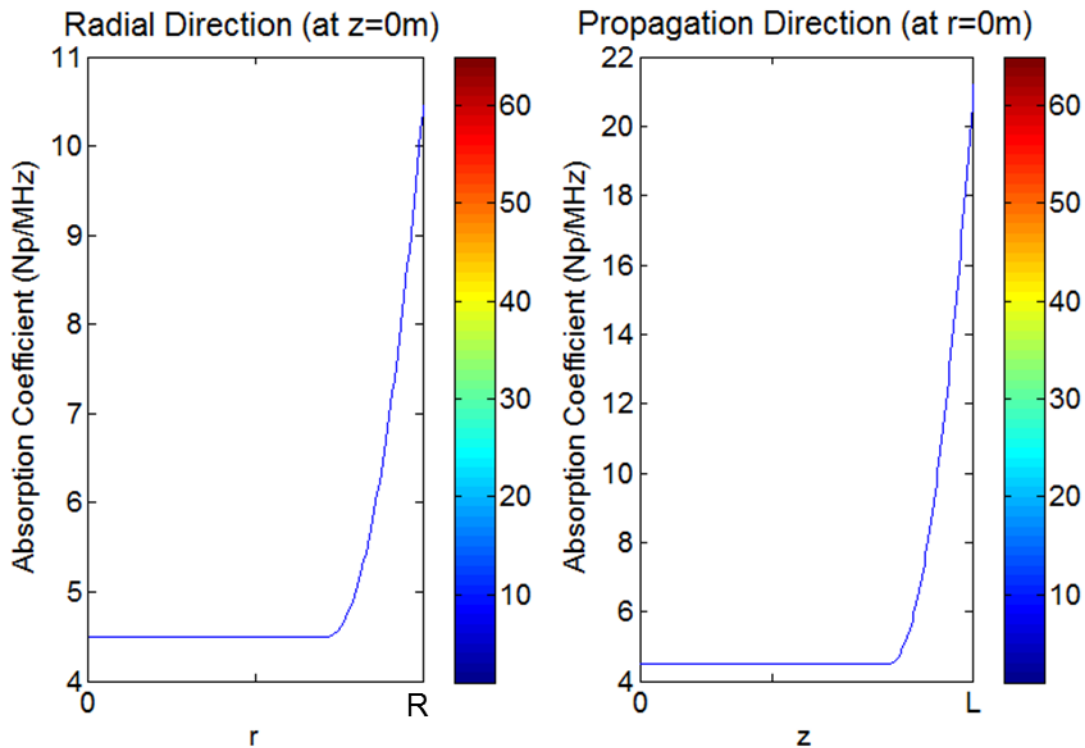


Figure 15 Absorption coefficient versus distance. L and R are the tissue's propagation and radial length, respectively Left: r-axis profile, Right: z-axis profile

The two dimensions of the medium are important parameters that need to be carefully examined.

They are denoted by L and R , respectively, and should be long enough in order to provide

significant results, that resemble practical applications. As expected, absorbing boundary conditions work better if the regions with higher absorptive properties are expanded further.

The equation for the propagation length L_c [m], for unfocused transducers, is shown in Eq. 52, where $L_{0.5P}$ [m] represents the distance the wave travels where its amplitude has been reduced by 50% of its maximum value. This value is represented by the Rayleigh distance Z_r [m], which is shown in [37], where λ is the wavelength of the signal [m].

$$L_c = 1.5 L_{0.5P} \quad \text{Eq. 52}$$

$$L_{0.5P} = Z_r = \frac{\pi R_s^2}{\lambda} \quad \text{Eq. 53}$$

Results from a past study [70] proved that there is a finite quantity for the propagation length L_c that provides the same results as the ones obtained using a hypothetical quantity $L_e \gg L_c$. The value of L_c can also be used for focused transducers; however, it might not be practical due to its computational expense. When driving focused signals into a medium, the far-field region usually does not experience pressure levels that are comparable to the ones in the focal region [37]. The value for $L_{0.5P}$ is almost identical to the focal point distance ϵ because of pressure values decay quickly after this distance [37].

It can therefore be concluded that L_c is a function of ϵ , and not $L_{0.5P}$, for focused transducers. Eq. 54 was obtained by using similar methods as the ones used to find L_c for piston transducers

$$L_c = 2.5 * \epsilon \quad \text{Eq. 54}$$

The reflections coming from the radial boundary are significantly smaller than the ones coming from the propagation boundary; however, they have to be taken into account. For piston sources, it is practical to assign a value for the radial length R_c that is dependent on L_c and the divergence half-angle width. The latter is defined in Eq. 55 for piston transducers as a function of the wavelength and the transducer size [37].

$$\theta_u = \sin^{-1} \left(\frac{0.61\lambda}{R_s} \right) \quad \text{Eq. 55}$$

For focused sources, the value for R_c depends on L_c and the aperture angle θ_f , which was shown in Figure 7. The definition of this angle comes from the trigonometric relationship between the radius of curvature and the transducer size, as shown in Eq. 56.

$$\theta_f = \sin^{-1} \left(\frac{\varphi}{R_s} \right) \quad \text{Eq. 56}$$

The value for R_c comes from solving the equation relating L_c and the angle θ which can be either θ_f or θ_u .

$$R_c = L_c \tan(2\theta) \quad \text{Eq. 57}$$

It can be seen that for piston sources the dimensions of the domain are primarily a function of the ratio between the transducer size and the frequency of the signal. An increment in the frequency causes a decrease in the wavelength. This, along with increments in the source radius, can lead to

larger values for the Rayleigh distance, therefore L_c . It also leads to a less accentuated decrease in the value of R_c .

Stability of the Numerical Procedure for Pressure Solution

Ultrasound signals generally involve large numbers for the values of frequency and pressure, usually ranging in the vicinity of the KHz-MHz and KPa-MPa ranges, respectively. It is necessary to have an enough amount of nodes in order to prevent aliasing phenomena. It has been known, for other types of studies using Finite Difference in the Time Domain (FDTD), that twenty nodes per wavelength λ is an acceptable amount that provides accurate results [26]. More nodes increase the accuracy of the results further but also increase the computational expense.

$$\Delta z = \frac{\lambda}{20} = \frac{c_0}{f 20}, \quad \Delta r = \frac{\lambda}{15} = \frac{c_0}{f 15} \quad \text{Eq. 58}$$

Eq. 58 shows how to calculate the spatial steps, where the value f is the regular central frequency [Hz]. The reason behind the value Δz being smaller than Δr is that the wave experiences more activity throughout the z axis. It can be seen that higher frequencies lead to denser grids, which lead to higher computational times.

In order to provide an adequate time step, the stability criterion from Neumann Analysis [26] is used. Eq. 59 shows the equation that describes this criterion, and will be used to obtain the time step Δt , which is usually in the order of 10^{-8} s.

$$\Delta t \leq \frac{\sqrt{3}}{2c_o\sqrt{\Delta z^{-2} + \Delta r^{-2}}} \quad \text{Eq. 59}$$

This significantly small time step serves as a significant inconvenience due to the fact that the temperature analysis does not require such small time steps, which will be discussed in later sections. Therefore, proper methods for coupling these are needed in order to provide a practical, computationally efficient, analysis.

Volumetric Heat Generation

In order to carry out the numerical analysis for the temperature field, the volumetric heat generation has to be calculated from the ultrasonic field. This is possible by using Eq. 29 for calculating the root-mean squared pressure followed by calculating the intensity $I_{i,j}$ at every node i and j .

$$I_{i,j} = \frac{P_{rms}^2}{\rho_o c_o} , \quad P_{rms} = \sqrt{\frac{1}{n_2 - n_1} \sum_{n_1}^{n_2} P_{i,j}^n{}^2} \quad \text{Eq. 60}$$

Eq. 60 is used to calculate these values where the time average used is in terms of iterations n_1 and n_2 , as opposed to the times t_1 and t_2 . The time average used to calculate the root mean squared is very important for providing accurate results; it average may not merely be taken as one acoustic period, since it would imply that the propagating acoustic wave consists of only one fundamental frequency. However, in view of the self-demodulation effect [37] [38] [71] [72] [73], even when the pressure source produces a monochromatic high frequency (as in the current

study), a low frequency signal would be generated with propagation [36] [37] [38] and a larger time span would need to be considered.

For continuous wave signals, ramping effects that occur initially do not need to be considered and therefore the volumetric heat generation computed during the initial phase needs to be omitted. However, for pulsed signals, it is important to consider this portion of the volumetric heat generation due to the discontinuities involved. The proper choice of the time range for continuous wave sources will be analyzed in the results and discussion section.

Temperature Discretization

The conservation of energy model to be discretized will include heat dissipation by conduction, perfusion, natural convection, and by viscous means, which is a combination of Eq. 33 and Eq. 35, and it leads to Eq. 61.

$$\begin{aligned} \frac{1}{r} \frac{\partial}{\partial r} \left(kr \frac{\partial T}{\partial r} \right) + \frac{\partial}{\partial z} \left(k \frac{\partial T}{\partial z} \right) + \dot{Q} + c_{pb} W_b (T_\infty - T) + \frac{\mu}{K} (u_b^2 + w_b^2) \\ = \rho_o c_p \left(\frac{\partial T}{\partial t} + u_b \frac{\partial T}{\partial z} + w_b \frac{\partial T}{\partial r} \right) \end{aligned} \quad \text{Eq. 61}$$

It is important to note that is the Pennes model is used, the values for the velocities u_b and w_b have to be set to zero. Moreover, if the Klinger model is to be used, the perfusion coefficient W_b will be set to zero.

For simplicity, the stream function ψ_b , will be substituted for velocities w_b and u_b using the relationship shown in Eq. 62, which comes from fundamentals of conservation of mass [74] [39].

$$u_b = \frac{1}{r} \frac{\partial \psi_b}{\partial r}, w_b = -\frac{1}{r} \frac{\partial \psi_b}{\partial z} \quad \text{Eq. 62}$$

Substituting the values of Eq. 62 into Eq. 40 and Eq. 61 leads to Eq. 63 and Eq. 64, which will be discretized explicitly and solved simultaneously for each iteration n. Eq. 64 assumes constant coefficient of thermal conduction k.

$$-\frac{\partial^2 \psi_b}{\partial z^2} - \frac{\partial^2 \psi_b}{\partial r^2} + \frac{1}{r} \frac{\partial \psi_b}{\partial r} = -\frac{Kg\rho_b\beta r}{\mu} \frac{\partial T}{\partial r} \quad \text{Eq. 63}$$

$$\begin{aligned} k \left(\frac{\partial^2 T}{\partial r^2} + \frac{1}{r} \frac{\partial T}{\partial r} + \frac{\partial^2 T}{\partial z^2} \right) + \dot{Q} + c_{pb} W_{pennes} (T_b - T) + \frac{\mu}{K} \left(\left(\frac{1}{r} \frac{\partial \psi_b}{\partial r} \right)^2 + \left(\frac{1}{r} \frac{\partial \psi_b}{\partial z} \right)^2 \right) \\ = \rho_o c_p \left(\frac{\partial T}{\partial t} + \frac{1}{r} \frac{\partial \psi_b}{\partial r} \frac{\partial T}{\partial z} - \frac{1}{r} \frac{\partial \psi_b}{\partial z} \frac{\partial T}{\partial r} \right) \end{aligned} \quad \text{Eq. 64}$$

The spatial derivatives, for both temperature and the stream function, shown in Eq. 63 and Eq. 64, are discretized using a central difference scheme in the second order. The time derivative for temperature is discretized using a forward difference scheme. The derivatives used are shown in Eq. 65-Eq. 73.

$$\frac{d^2 \psi_b}{dz^2} = \frac{\psi_{b_{i+1,j}}^n + \psi_{b_{i-1,j}}^n - 2\psi_{b_{i,j}}^n}{\Delta z^2} \quad \text{Eq. 65}$$

$$\frac{d^2 \psi_b}{dr^2} = \frac{\psi_{b_{i,j+1}}^n + \psi_{b_{i,j-1}}^n - 2\psi_{b_{i,j}}^n}{\Delta r^2} \quad \text{Eq. 66}$$

$$\frac{d\psi_b}{dz} = \frac{\psi_{b_{i+1,j}}^n - \psi_{b_{i-1,j}}^n}{2\Delta z} \quad \text{Eq. 67}$$

$$\frac{d\psi_b}{dr} = \frac{\psi_{b_{i,j+1}}^n - \psi_{b_{i,j-1}}^n}{2\Delta r} \quad \text{Eq. 68}$$

$$\frac{d^2T}{dz^2} = \frac{T_{i+1,j}^n + T_{i-1,j}^n - 2T_{i,j}^n}{\Delta z^2} \quad \text{Eq. 69}$$

$$\frac{d^2T}{dr^2} = \frac{T_{i,j+1}^n + T_{i,j-1}^n - 2T_{i,j}^n}{\Delta r^2} \quad \text{Eq. 70}$$

$$\frac{dT}{dz} = \frac{T_{i+1,j}^n - T_{i-1,j}^n}{2\Delta z} \quad \text{Eq. 71}$$

$$\frac{dT}{dr} = \frac{T_{i,j+1}^n - T_{i,j-1}^n}{2\Delta r} \quad \text{Eq. 72}$$

$$\frac{dT}{dt} = \frac{T_{i,j}^{n+1} - T_{i,j}^n}{\Delta t} \quad \text{Eq. 73}$$

Eq. 74 is used to calculate the temperature field and it is obtained by substituting Eq. 65-Eq. 73 into Eq. 63 and solving for $T_{i,j}^{n+1}$. It is important to note that the discrete values used for the pressure field and stream function $\Delta t'$, $\Delta z'$, and $\Delta r'$ are not the same as the ones used for the pressure field Δt , Δz , and Δr .

$$\begin{aligned}
T_{ij}^{n+1} = T_{ij}^n + \Delta t' & \left(-\frac{1}{r(j)} \left(\frac{\psi_{b_{ij+1}}^n - \psi_{b_{ij-1}}^n}{2\Delta r'} \right) \left(\frac{T_{i+1,j}^n - T_{i-1,j}^n}{2\Delta z'} \right) + \frac{1}{r(j)} \left(\frac{\psi_{b_{i+1,j}}^n - \psi_{b_{i-1,j}}^n}{2\Delta z'} \right) \left(\frac{T_{ij+1}^n - T_{ij-1}^n}{2\Delta r'} \right) \right. \\
& + \frac{1}{\rho_o c_p} \left(k \left(\left(\frac{T_{ij+1}^n + T_{ij-1}^n - 2T_{ij}^n}{\Delta r'^2} \right) + \frac{1}{r(j)} \left(\frac{T_{ij+1}^n - T_{ij-1}^n}{2\Delta r'} \right) + \left(\frac{T_{i+1,j}^n + T_{i-1,j}^n - 2T_{ij}^n}{\Delta z'^2} \right) \right) + \dot{Q}_{i,j} \right. \\
& \left. \left. + c_{pb} W_{pennes} (T_\infty - T_{ij}^n) + \frac{\mu}{K} \left(\left(\frac{1}{r(j)} \left(\frac{\psi_{b_{ij+1}}^n - \psi_{b_{ij-1}}^n}{2\Delta r'} \right) \right)^2 + \left(\frac{1}{r(j)} \left(\frac{\psi_{b_{i+1,j}}^n - \psi_{b_{i-1,j}}^n}{2\Delta z'} \right) \right)^2 \right) \right) \right)
\end{aligned} \tag{Eq. 74}$$

The values for the stream function are obtained from Eq. 75. Once again, the appropriate terms are substituted into Eq. 64 and then the equation is solved for $\psi_{b_{i,j}}^n$. This equation does not depend on time and it therefore has to be solved for every iteration once the temperatures of every node $T_{i,j}^n$ are obtained (from the past iteration).

$$\begin{aligned}
\psi_{b_{i,j}}^n = \left(\frac{2}{\Delta z'^2} + \frac{2}{\Delta r'^2} \right)^{-1} & \left(\left(\frac{\psi_{b_{i+1,j}}^n + \psi_{b_{i-1,j}}^n}{\Delta z'^2} \right) + \left(\frac{\psi_{b_{ij+1}}^n + \psi_{b_{ij-1}}^n}{\Delta r'^2} \right) - \frac{1}{r(j)} \left(\frac{\psi_{b_{i+1,j}}^n - \psi_{b_{i-1,j}}^n}{2\Delta r'} \right) \right. \\
& \left. - \left(\frac{Kg\rho_b\beta r(j)}{\mu} \left(\frac{T_{ij+1}^n - T_{ij-1}^n}{2\Delta r'} \right) \right) \right)
\end{aligned} \tag{Eq. 75}$$

Temperature Field Stability/Grid Coarsening

The stability criterion for the energy equation is not as rigorous as the one for the wave equation. However, undesired oscillations followed by instabilities might occur upon setting an incorrect value for the time step $\Delta t'$. A safe criterion to be used requires that the coefficient obtained from

factoring all the terms with the last temperature obtained, $T_{i,j}^n$, has to be bigger or equal to zero

[74], as shown in Eq. 76.

$$1 - \frac{2k\Delta t'}{\rho_o c_p \Delta r'^2} - \frac{2k\Delta t'}{\rho_o c_p \Delta z'^2} - \frac{c_{pb} W_{pennes} \Delta t'}{\rho_o c_p} \geq 0 \quad \text{Eq. 76}$$

Upon solving for the time step, Eq. 77 is obtained. It can be seen that increments in the coefficient of conductivity k lead to decrements in the time step $\Delta t'$.

$$\left(\frac{2k}{\rho_o c_p} \left(\frac{1}{\Delta r'^2} + \frac{1}{\Delta z'^2} \right) + \frac{c_{pb} W_{pennes}}{\rho_o c_p} \right)^{-1} \geq \Delta t' \quad \text{Eq. 77}$$

The values for $\Delta r'$ and $\Delta z'$ should not be the same ones as the ones used for the wave equation.

A proper grid independence study is required in order to find the optimum spatial discrete values.

This study will be shown in the results section. However, it is known that the spatial

discretization for temperature will be bigger than the one for pressure. It is therefore required to

produce an algorithm that transforms the grid size of the volumetric heat generation $\dot{Q}_{i,j}$ into one

with a coarser size, referred with different index values $\dot{Q}'_{i',j'}$.

The first assumption needed for the algorithm to work is that the discrete spatial values for

temperature are a multiple factor of the ones for the pressure field, as shown in Eq. 78. In this

equation, the values of N and M have to be integers.

$$\Delta z' = N\Delta z ; \Delta r' = M\Delta r \quad \text{Eq. 78}$$

Recall Figure 13, where the grid for the pressure field is shown. Figure 16 shows the grids both for the pressure and temperature field superimposed. It can be seen that, in this case, the value for m and n is 3. The first step is to define the variables $\Delta z'$, $\Delta r'$, N , and M from the amount of nodes the coarser grid will be.

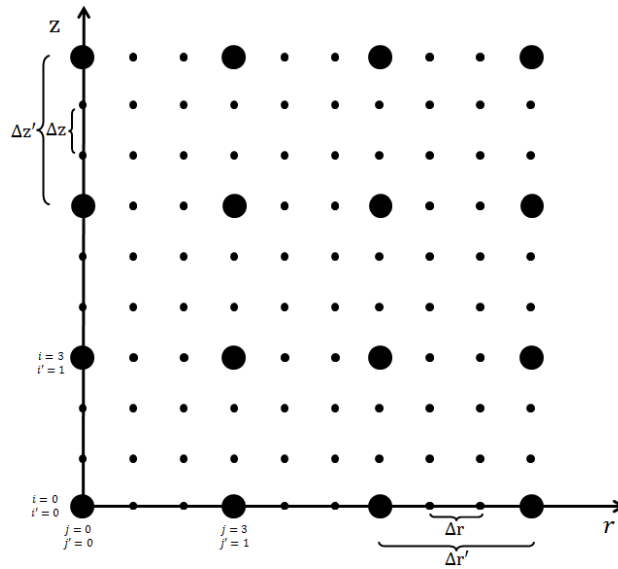


Figure 16 Schematic for the spatial pressure and temperature field used, where the larger dots define the temperature field nodes and the smaller dots define the pressure field nodes

The next step is to convert the obtained volumetric heat generation field $\dot{Q}_{i,j}$ [W m^{-3}] with the finer grid into heat generation $Q_{i,j}$ [W] by multiplying it with its respective volume $V_{i,j}$ [m^3] at each index value i and j , which is shown in Eq. 79.

$$Q_{i,j} = V_{i,j} \dot{Q}_{i,j} ; \text{ where, } V_{i,j} = \Delta z (2\pi r(j) \Delta r) \quad \text{Eq. 79}$$

Once the heat generation is obtained, it has to be converted into the actual heat generation respective of its coarser grid $Q'_{i',j'}$. Doing so will require defining the following parameters, shown in Eq. 80.

$$i_{center} = n(i' - 1) + 1 ; j_{center} = m(j' - 1) + 1 \quad \text{Eq. 80}$$

These variables can be visualized in Figure 17, where the corresponding index values for the pressure field i, j are shown for each index point i', j' . The variables are needed in order to transform the heat generation into the coarser grid, by using Eq. 81.

$$Q'_{i',j'} = \sum_{i=i_{center}-\left(\frac{n-1}{2}\right)}^{i_{center}+\left(\frac{n-1}{2}\right)} \sum_{j=j_{center}-\left(\frac{m-1}{2}\right)}^{j_{center}+\left(\frac{m-1}{2}\right)} Q_{i,j} \quad \text{Eq. 81}$$

This equation collects the values for heat generation around the grey area shown in Figure 17. It has to be noted that only odd values of N and M will be permitted. More complicated methods than Eq. 81 are needed if even values of N and M were to be used as well.

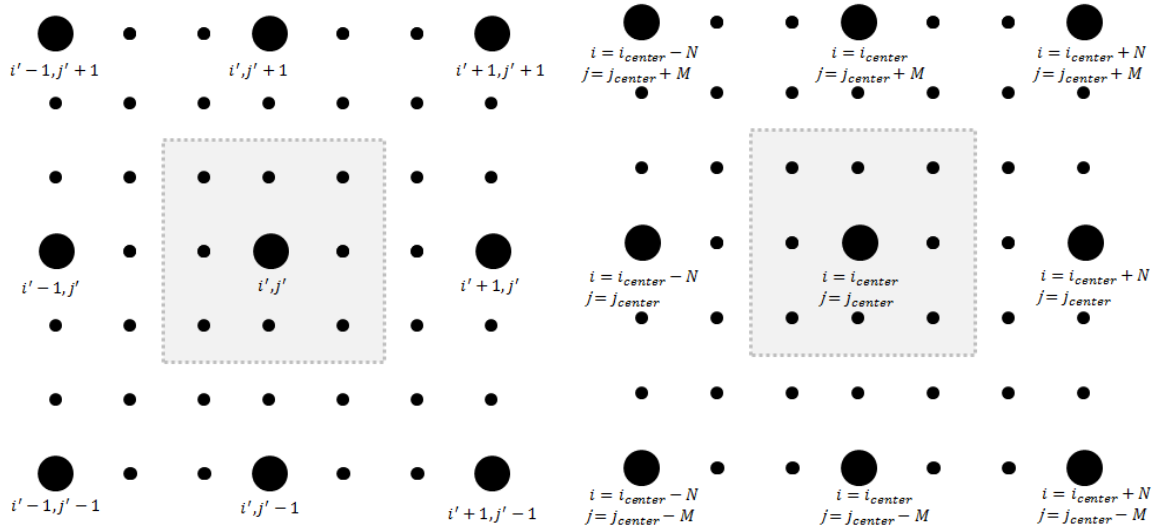


Figure 17 Left: schematic of certain point in space described for index values of temperature; Right: schematic of the same point in space described for index values of pressure

The last step requires transforming the obtained heat generation into the volumetric heat generation needed. This process is shown in Eq. 79

$$\dot{Q}'_{i,j} = \frac{Q'_{i,j}}{V'_{i,j'}} ; \text{ where, } V'_{i,j'} = \Delta z' (2\pi r(j') \Delta r') \quad \text{Eq. 82}$$

The grid generated will be the one used for the temperature numerical scheme. It decreases the computation time per iteration and requires less iterations in order to give meaningful results.

This is due to the fact that increments in $\Delta r'$ and $\Delta z'$ lead to increments in $\Delta t'$, as seen in Eq. 77.

The boundary conditions for the temperature field and the stream function do not suffer from computational reflections or any computational anomaly of that nature. The outer boundaries are kept at an ambient temperature of 38°C, and they are therefore acting as a heat sink [74]. The

outer boundaries for the stream function field are maintained at 0 following the same logic at the outer temperature boundaries.

Symmetry conditions are applied for the temperature and stream function fields along the z-axis when $r=0$. In other words, the gradient $\partial T/\partial r=0$; which means that the boundary acts as an insulator, not letting any heat go through [74]. Moreover, there is no flow going through the radial direction, at the boundary, which means that the velocity in the radial direction $w_b = 0$, and according to Eq. 62, $\partial\psi_b/\partial z=0$.

Applying the conditions just mentioned and substituting for Eq. 64, leads to Eq. 83. Noting that $r = 0$ at this boundary leads to the gradient $\partial\psi_b/\partial r=0$. It can be concluded that this flow is irrotational at the boundary, which means that its vorticity (or the curl of the velocity vector) is zero [75].

$$-r \frac{\partial^2 \psi_b}{\partial z^2} - r \frac{\partial^2 \psi_b}{\partial r^2} + \frac{\partial \psi_b}{\partial r} = 0 \quad \text{Eq. 83}$$

Approximating this derivative by second order forward finite difference leads to Eq. 84, which shows the value of the stream function at the propagation axis.

$$\psi_{b,i,1}^n = \frac{4\psi_{b,i,2}^n - \psi_{b,i,3}^n}{3} \quad \text{Eq. 84}$$

Applying the same conditions and substituting for Eq. 63 leads to Eq. 85. In this equation, heat is dissipated only by conduction and perfusion.

$$k \left(\frac{\partial^2 T}{\partial z^2} \right) + \dot{Q} + c_{pb} W_{pennes} (T_\infty - T) = \rho_o c_p \left(\frac{\partial T}{\partial t} \right) \quad \text{Eq. 85}$$

By using the appropriate central and forward finite difference method to the spatial second derivative and time derivative, Eq. 69 and Eq. 73 respectively, the value for the temperature and the propagation axis can be computed, as shown in Eq. 86.

$$T_{i,1}^{n+1} = T_{i,1}^n + \frac{\Delta t}{\rho_o c_p} \left(k \left(\frac{T_{i+1,1}^n + T_{i-1,1}^n - 2T_{i,1}^n}{\Delta z'^2} \right) + \dot{Q}_{i,1} + c_{pb} W_{pennes} (T_\infty - T_{i,1}^n) \right) \quad \text{Eq. 86}$$

Chapter 4: Results and Discussion

The properties used to describe tissue are shown in Table 1. The thermal properties used in this study are exclusively for prostate tissue [76]. The acoustic properties given are for water, which are very similar to the ones of any soft tissue [38] [77].

Table 1 Properties of prostate tissue

Symbol	Property Name	Reference	Units	Ref
α	Absorption Coefficient	4.5	$\text{Np m}^{-1} \text{MHz}^{-1}$	[31]
c_o	Small Signal Sound Speed	1500	m s^{-1}	[37] [38]
c_p	Specific Heat Capacity	3800	J K^{-1}	[74]
k	Thermal Conductivity Coefficient	0.5	$\text{W m}^{-1} \text{K}^{-1}$	[76] [74]
K	Permeability	11e-14	m^2	[78]
m	Signal Waveform Coefficient	10	-	-
β	Nonlinearity Coefficient	5.5	-	[38]
β	Coefficient of Thermal Expansion	4e-4	K^{-1}	[74]
μ	Viscosity	3.5e-3	kg m s^{-1}	[37] [38]
ρ	Density	1050	kg m^{-3}	[76]

The results about to be shown are a product of several trials where the frequency f as varies from 0.5 MHz to 1.25 MHz, the pressure P_o from 0.1MPa to 1.5 MPa, and the source radius R_s from 5 mm to 20 mm.

The pressure field will be discussed first, where a proper comparison of the source geometries and signal types will be done. The heat generation due to some pressure fields will then be compared and analyzed for different time range averages. Further, the temperature fields along with comparison of the Pennes and Klinger model will be done. Finally, development of simple

mathematical functions will be done with data for maximum pressure and volumetric heat generation.

Pressure Field

The results obtained have been compared with results from previous studies involving the use of Westervelt equation for describing ultrasonic wave propagation [26] [37].

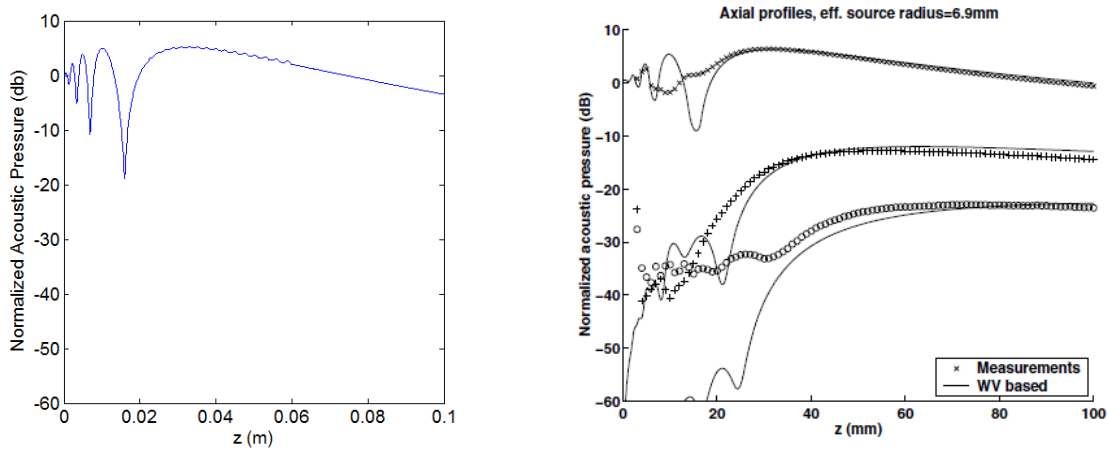


Figure 18 Results for axial profile of normalized peak pressures $P_o=0.5MPa$, $f=1MHz$, $R_s=7mm$; Left: Obtained with numerical scheme of this study; Right: separated into the first three harmonics, obtained with numerical scheme study by Huijssen [26]

Figure 18 shows one of these comparisons between two axial profiles resulting from delivering a 1 MPa continuous wave signal with a frequency of 1 MHz. The left graph in this figure uses the scheme developed in this study, while the right one uses a different scheme from a past study by Huijssen et al. (which separates these results for the first three harmonics) [26].

The profiles look similar. The main difference are observed in the pressure drops which, even though they happen at the same location, are more steep for the scheme used in this study. This is because Huijssen used smaller values for Δz and Δr , and therefore, smaller time step Δt .

However, the important regions, where the pressure reaches significant values, are identical for both schemes and they are therefore assumed to provide the same results.

Results for the pressure field for both unfocused and focused sources will be presented below for continuous wave and pulse signals. The main differences regarding focal point location and overall pressure values will be compared.

Unfocused Signals

Figure 19 shows an unfocused source with a radius of 5 mm delivering a 1MPa continuous wave signal with a frequency of 1 MHz. The entire signal is fully developed at the end of the trial. The signal reaches steady pressure peak at regions past where the signal already travelled. The wave progresses through the medium until it reaches the length of the domain. At this point, the peak pressures remain constant, which suggests that the boundary conditions are effectively acting as infinite media.

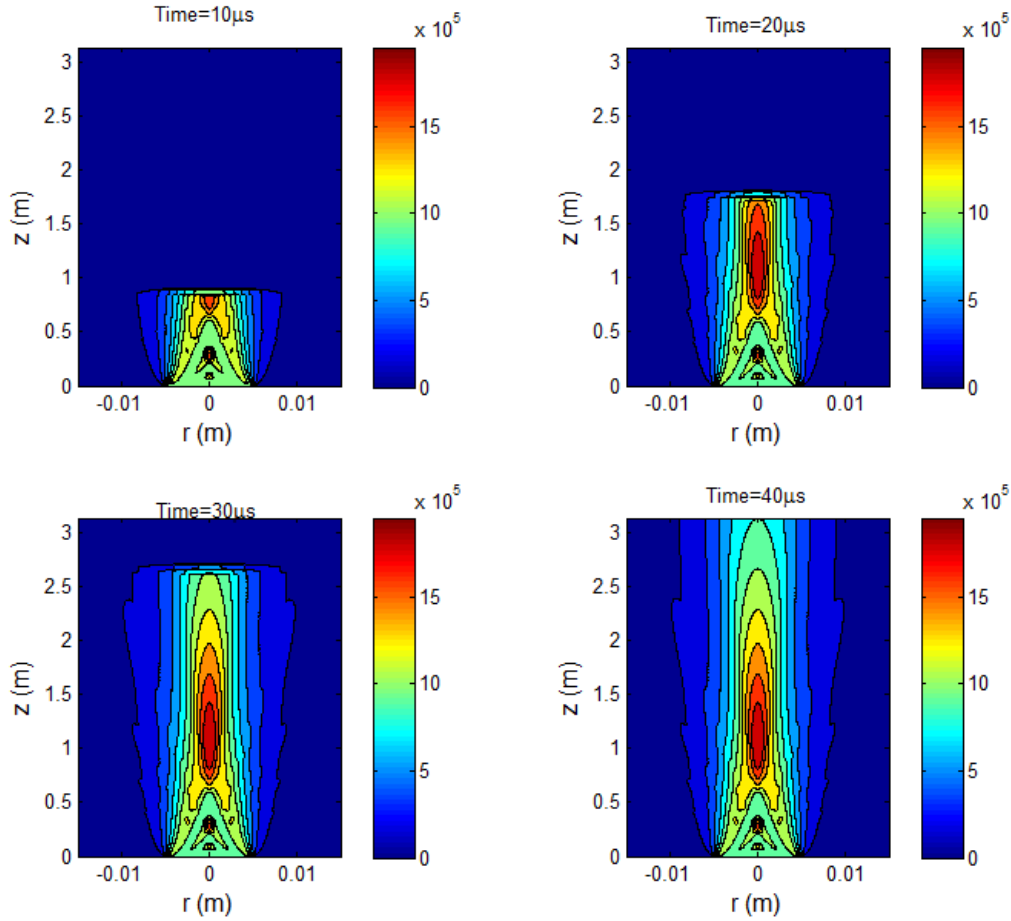


Figure 19 Pressure contour graphs (Pa) for a continuous wave signal in development: $P_o=1MPa$, $f=1MHz$, $R_s= 5mm$; Top left: for $t=10 \mu s$, Top right: for $t=20 \mu s$, Bottom left: for $t=30 \mu s$, Bottom right: for $t=40 \mu s$,

Figure 20 shows a similar contour graph for an unfocused 1 MPa and 1 MHz pulse signal with a source radius of 5 mm, and a pulse length of $T_o= 0.1\mu s$. As discussed in earlier sections, the pulsed signal is mathematically described by an envelope in time, shown in Eq. 20 and Eq. 24. Its pulse length T_o is dictated with the use of the desired duty factor DF, shown in Eq. 21, and the proper choice of T_{tot} (depending on the length L_c , shown in Eq. 52, and the velocity of the wave c).

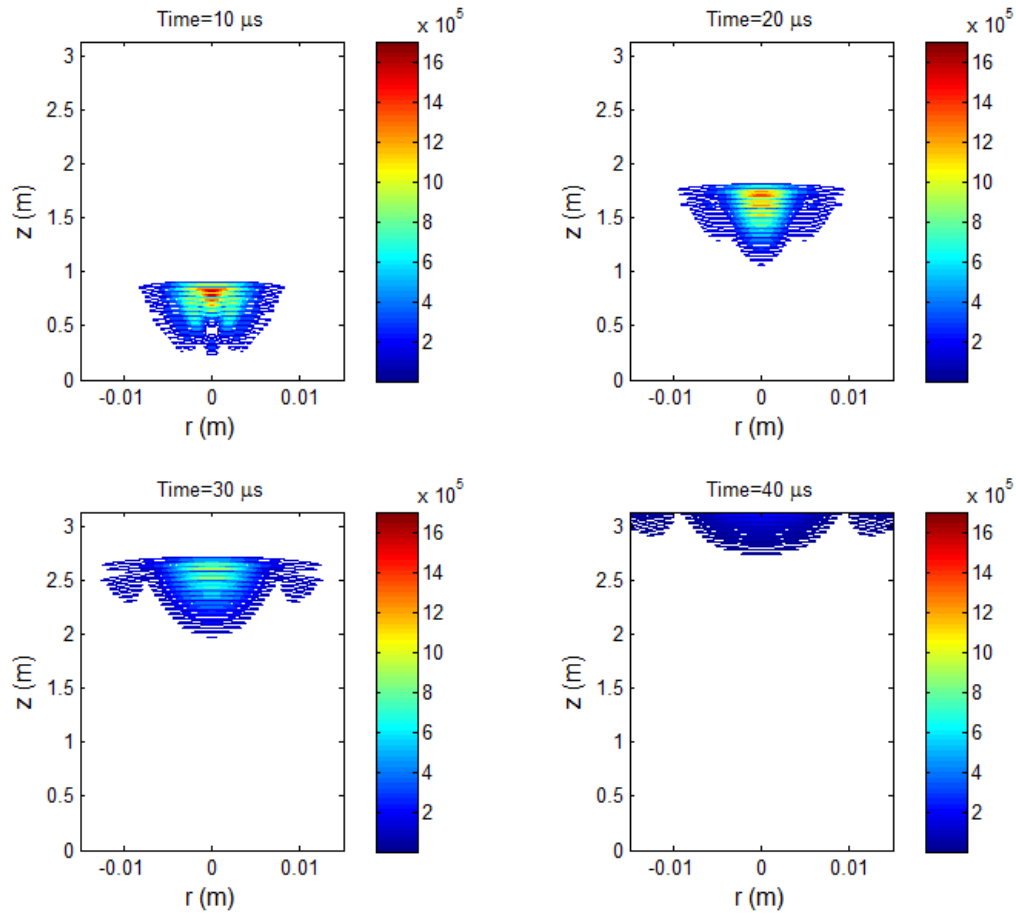


Figure 20 Pressure Contour graphs (Pa) for a Pulsed Signal in Development: $P_o=1MPa$, $f=1MHz$, $R_s=5mm$ $T_o=0.1\mu s$, $DF=0.25\%$

The final form of the continuous wave ultrasonic field can be further observed in Figure 21, which shows the normalized pressure axial profile at $r=0$. Nonlinearity effects can be seen by noting that the normalized pressure amplitudes increases by more than 5 dB with respect to the source pressure prescribed. Moreover, the signal's amplitude decay occurring in the region past the focal point shows that the absorptive properties are taken into effect.

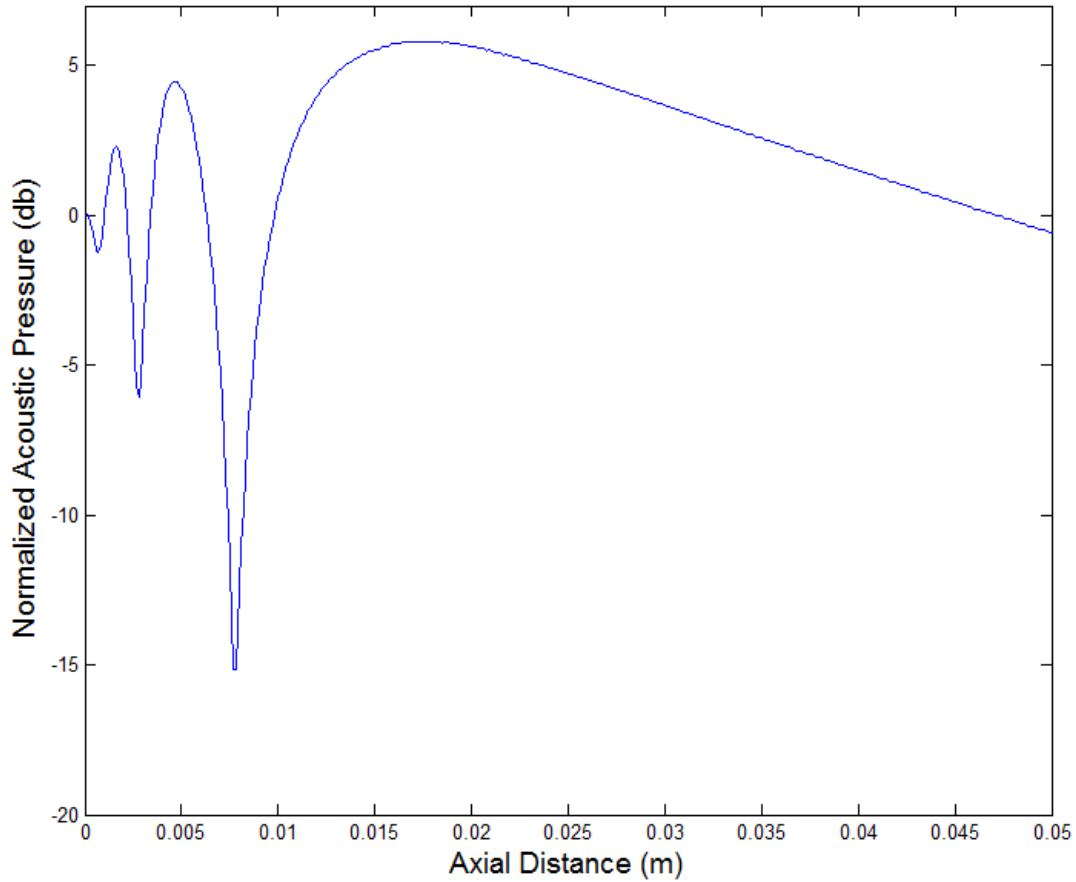


Figure 21 Axial Normalized Pressure for an Unfocused Source Delivering a Continuous Wave Signal:
 $P_o=1\text{ MPa}$, $f=1\text{ MHz}$, $R_s=5\text{ mm}$

The location where the maximum normalized pressure amplitude resides is approximately 0.016 m, which agrees with the linear acoustic theory. The focal point distance for piston sources can be approximated by Eq. 87 shown below [37] [38]. The resulting focal point distance calculated for this case is 0.0166m.

$$Z_{FP} = \frac{R_s^2}{\lambda}$$

Eq. 87

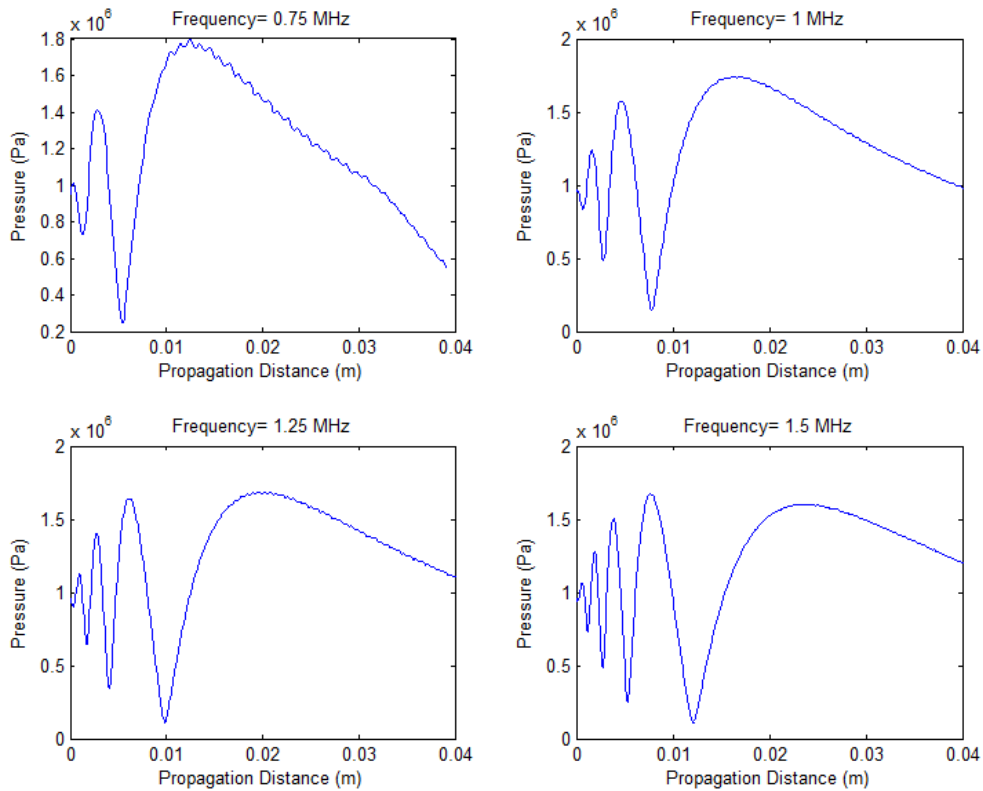


Figure 22 Root Mean Squared Pressure (Last 20% of the propagation Time) For Different Frequencies Prescribed by an Unfocused Source: $P_o=1MPa$, $R_s=5mm$

It can be seen in Figure 22 that variations in frequency not only change the location of the focal point, but also the pressure behavior at the near field. The focal point region is also less accentuated with increasing frequency. The graph corresponding to a frequency of 1.5 MHz suggests that at frequencies higher than a certain threshold value, Eq. 87 is not valid because the pressure at a certain point in the near field exceeds the one at the focal point.

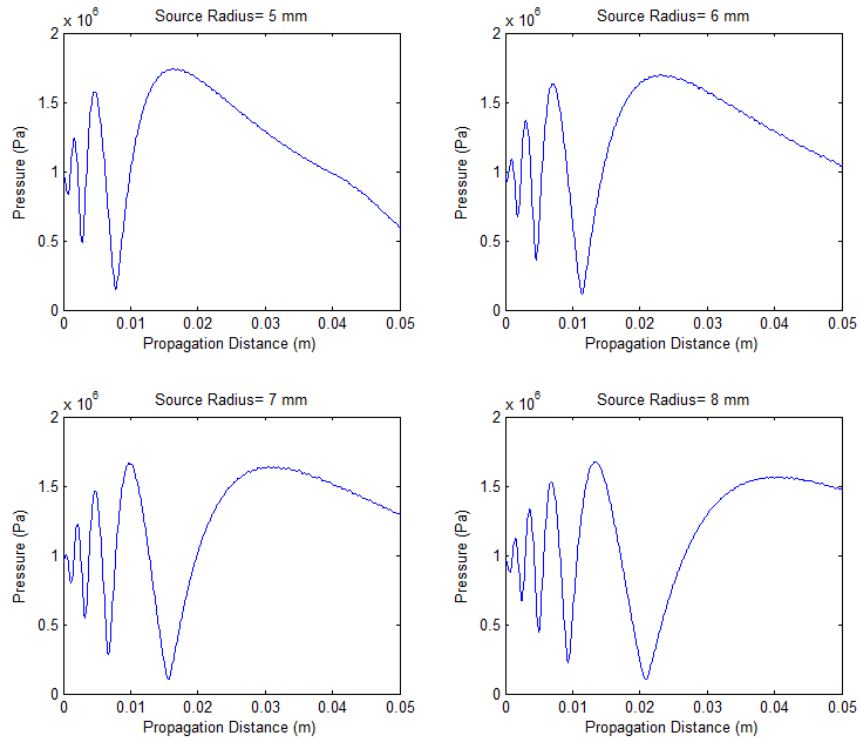


Figure 23 Root Mean Squared Pressure (Last 20% of the propagation Time) For Different Source Radii Prescribed by an Unfocused Source: $P_o=1MPa$, $f = 1 MHz$

Variations in the source radius correspond to the same type of changes in the pressure field as with varying frequency, as shown in Figure 23. It also proves that Eq. 87 is only valid for a certain range of transducer radii. In order to find the threshold value where Eq. 87 does not longer describe the focal point distance Z_{FP} the introduction of a new number is needed. In this study, the ka number will be defined using Eq. 88 [38]. Past derivations and validations of Westervelt and KZK equation [28] [46] [53] have used this dimensionless quantity to couple the source radius and frequency parameters (where the parameter a is defined as the transducer size, as opposed to R_s for this study).

$$ka = k * R_s = \frac{2\pi R_s}{\lambda} = \frac{2\pi f R_s}{c_o} \quad \text{Eq. 88}$$

Table 2 Error between Magnitude and Location of the Maximum Pressure with respect to the Calculated Focal Point: $P_o=1 \text{ MPa}$

Frequency (MHz)	Source Radius (mm)	ka Number(-)	Pressure Magnitude error (%)	Distance Error (%)
0.75	5	15.708	0	0.8
0.75	6	18.8496	1.2163	2.22
0.75	7	21.9911	0.7728	2.585
0.75	8	25.1327	0.4552	3.75
0.75	9	28.2743	0.7422	69.3827
0.75	10	31.416	4.4289	69.6
0.85	5	17.8024	1.7071	4.4983
0.85	6	21.3628	0	0.8074
0.85	7	24.9233	0.4589	1.2782
0.85	8	28.4838	1.2841	69.18
0.85	9	32.0442	5.504	68.9863
0.85	10	35.605	9.2913	68.651
0.95	5	19.8968	0.0852	1.6066
0.95	6	23.8761	0.2668	3.9705
0.95	7	27.8555	0.0668	5.3649
0.95	8	31.8348	5.5089	69.356
0.95	9	35.8142	9.4302	69.0161
0.95	10	39.794	14.034	67.59
1	5	20.944	0.494	2.2
1	6	25.1327	0.4552	3.75
1	7	29.3215	2.2291	70.3061
1	8	33.5103	6.8733	68.8281
1	9	37.6991	11.8238	68.333
1	10	41.888	15.049	68.8

Table 2 shows a series of trials where frequency and source radius were varied. The recorded results included the ka number, the percentage difference of the maximum pressure P_{max} with

respect to the pressure at the focal point P_{FP} , and the percentage difference of the respective distance where the maximum pressure occurs with respect to the focal point distance.

Small percentage differences occur for ka numbers smaller than approximately 28.4. For ka numbers higher than this value, the percentage error for the pressure magnitude increases with increasing ka numbers. However, the percentage difference for the distance stays roughly constant.

For trials with different frequencies and source radii, but identical ka numbers, the results calculated for both percentage differences are identical. The two contour graphs in Figure 24 show that almost identical behaviors for the pressure field are also obtained for signal sharing identical values of the ka number.

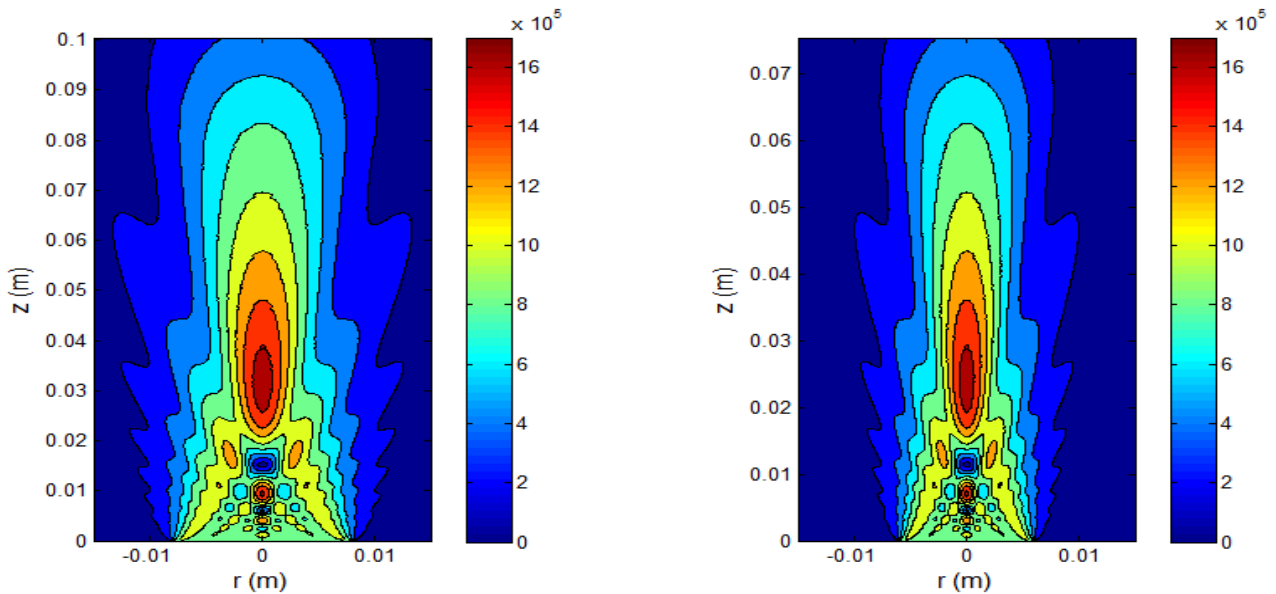


Figure 24 Left: Pressure contours for $P_0=1$ MPa, $f=0.75$ MHz, $R_s=8$ mm, $ka=25.13$; right: pressure contours for $P_0=1$ MPa, $f=1$ MHz, $R_s=6$ mm, $ka=25.13$

Variations in the source pressure prescribed do not affect the overall behavior, or shape, of the pressure field, but just scales the magnitude. Figure 25 shows different results for axial profiles of RMS pressures resulting from different signal pressures ranging from 0.1 to 1 MPa at a frequency of 1 MHz for an unfocused source of radius $R_s = 6\text{mm}$.

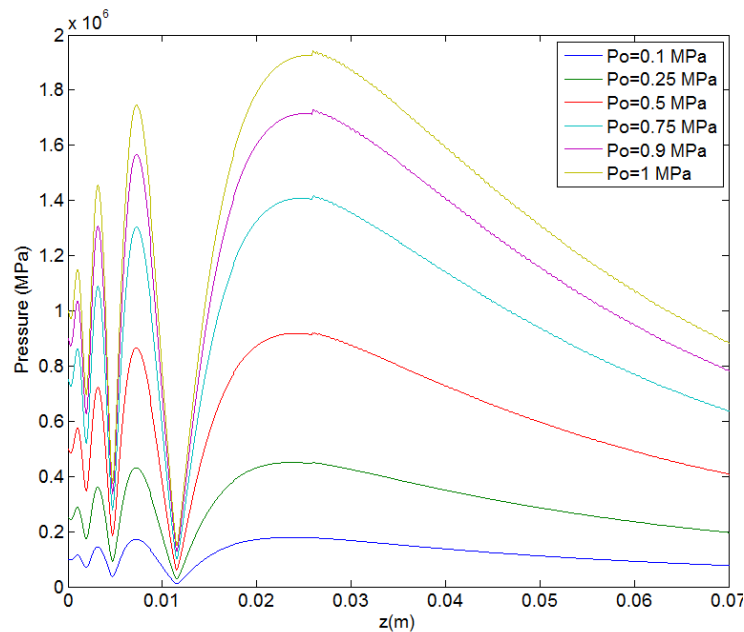


Figure 25 Root Mean Squared Pressure (last 20% of the Propagation time) for Different Source Pressures Prescribed

Results show that the overall shape of the profile remains undisturbed; however, by scaling these profiles, as shown in Figure 26, the nonlinear behavior is evident and it proves that even for piston sources it has to be taken into account for large source pressure amplitudes, as done in the past [25].

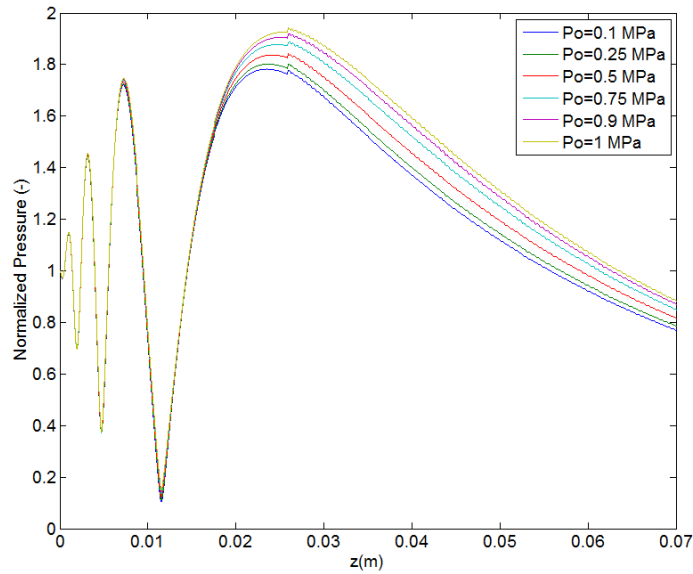


Figure 26 Root Mean Normalized Squared Pressure (last 20% of the Propagation time) for Different Source Pressures Prescribed

Focused Signals

As expected, the pressure field for focused sources is mostly dictated by the radius of curvature of the focused source φ . Figure 27 shows the expected, the by two different focused sources, with the same source radius and continuous wave signal of 0.25 MPa and 1 MHz. The maximum pressure occurs at a distance equal to the difference between the radius of curvature φ and the rim height h . This number was already assigned as ϵ and illustrated in Figure 7.

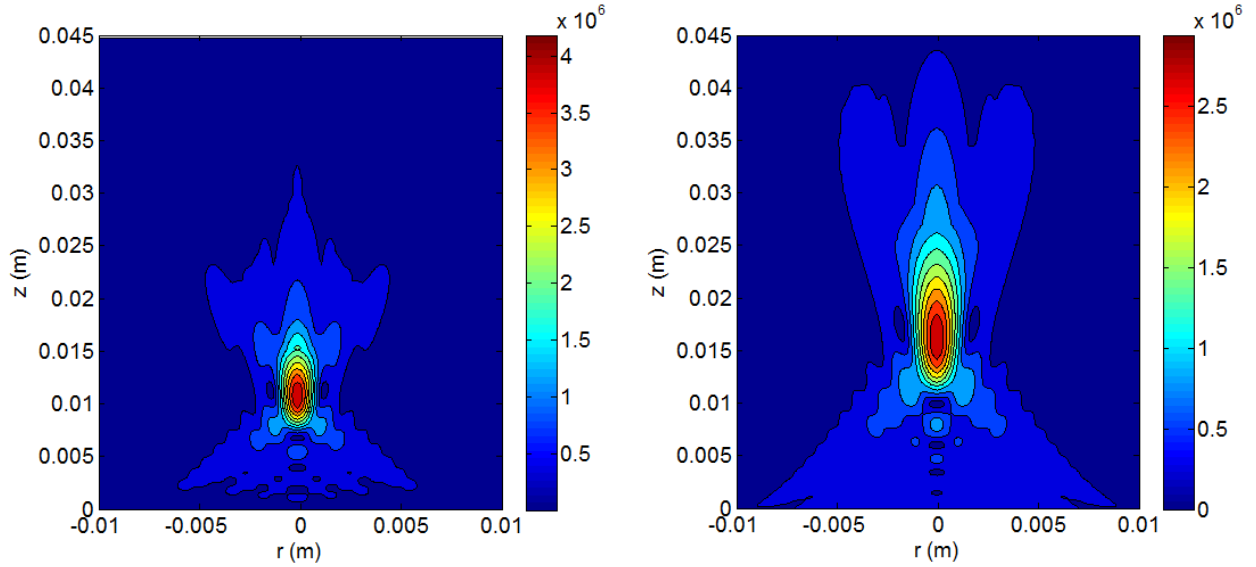


Figure 27 Pressure Contour for a focused source $P_o=0.25 \text{ MPa}$, $f=1 \text{ MHz}$, $R_s= 10\text{mm}$, Left: $\epsilon= 11.20\text{mm}$, Right: $\epsilon= 17.30 \text{ mm}$

It can be seen that the smaller the radius of curvature is, the more the transducer is forcing the signal to be focused. This increases the pressure at that point and it is significantly greater than the prescribed pressure.

Many analytical solutions for focused sources [38] [37] [43] [53], especially for solving the KZK equation shown in Eq. 16, have used the dimensionless number referred to as the gain G , which is shown in Eq. 89. This number is equal to the peak value of the pressure at the focal point divided by the source pressure prescribed P_o .

$$G = \frac{Z_r}{\varphi} = \frac{P(0, \epsilon)}{P_o} \quad \text{Eq. 89}$$

It can be seen on Table 3 that this nondimensional quantity does not describe the actual ratio $\frac{P_{max}}{P_o}$.

This is due to the fact that Westervelt equation is an approximation of directional beams, as discussed before. In this results, the error percentage decreases with increasing radius of curvature. It has been concluded that its accuracy starts decreasing at aperture angles of 20° or higher [46]. Other effects such as self-demodulation provoke strong nonlinearities which lead to no useful correlation for strong focus (small radius of curvature).

Table 3 Resulting Gain and Error with respect to linear Gain Theory for a 0.25MPa, and 1 MHz signal with a radius source of 10 mm

Radius of Curvature φ	Distance to Focal Point ϵ	Aperture Angle θ	Gain G	$\frac{P(0, \epsilon)}{P_o}$	Error %
15	11.2	41.81	13.96	16.2295	13.98379
20	17.3	30	10.47	11.66	10.20583
25	22.9	23.5782	8.3776	9.0167	7.087959
30	28.3	19.4712	6.9813	7.5023	6.944537
35	33.5	16.6015	5.984	6.3892	6.341952

However, the fact that the error decreases uniformly with increasing the radius of curvature suggests some dependence. Therefore, because of the dependence of G on the Rayleigh distance Z_r , it can be concluded that, for focused transducers, the frequency and the source radius, as well as the radius of curvature, are important factors that define the maximum pressure obtained in the field, and therefore the heat generated by the signal.

Volumetric Heat Generation

The appropriate time average selection mentioned earlier will be revisited and discussed further. The importance of this time average will then be compared for pulsed and continuous wave signals.

Selection of Time Average

As discussed earlier, not averaging the heat generation leads to results that will depend on time. This means that the temperature and pressure numerical schemes would have to be computed at the exact times, for every iteration. Hallaj et al performed both simulations simultaneously showed that negligible temperature rise is obtained for reasonable amount of computational time [25].

In order to provide adequate coupling between temperature and pressure, an adequate time range for the time average of the intensity has to be computed. It means that the values for the iteration numbers n_1 and n_2 of Eq. 60 have to be chosen such that the resulting intensity does not depend on time. Other recent studies have not averaged the intensity and performed simulations with different pressure and temperature times steps, assuming that it was already time independent [34] [56]. Moreover, other studies by Hallaj et al [31], Yin et al. [49], and Makov et al. [29] averaged the intensity for one entire cycle of time, or the acoustic period.

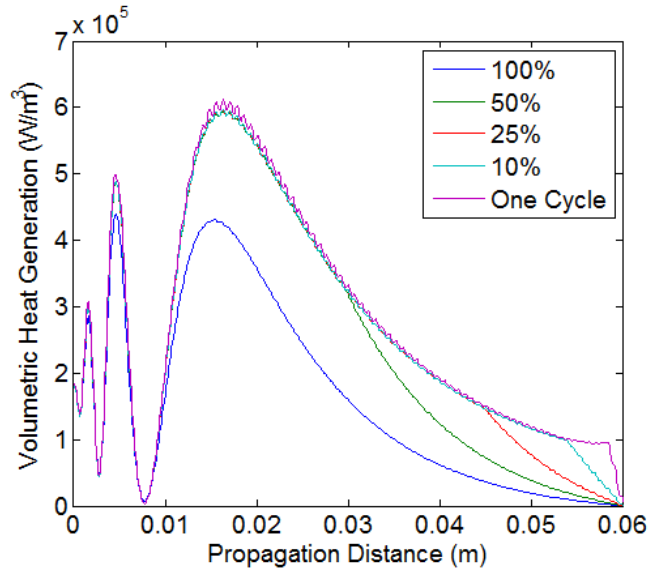


Figure 28 Axial Profile of Average Volumetric Heat Generation for different Time Ranges

Figure 28 shows a graph of the axial profile at $r=0$ for different volumetric heat generation rates. These are all obtained from the resulting pressure field of a 6 mm radius piston transducer radiating a continuous 0.25 MPa signal at a frequency of 1 MHz at different time ranges. In other words, n_2 was the maximum number of iterations (the same for each trial) and $n_1 = 0, 0.5 n_2, 0.75 n_2, 0.9 n_2, 1.0 n_2 - \frac{1}{f \Delta t}$, where the last term means that the average was taken to be merely the last acoustic period.

Ramping effects are evident when taking the average of the entire trial, and it can be seen that it leads to noisy results. This is due to the fact that ramping effects only happen when the pressure field is reaching a steady state. These can be assumed to be negligible for continuous waves.

Taking the average over the last cycle leads to volumetric heat generation fields that are not constant with time, as seen by the small oscillations the curve exhibits. The higher the pressure, the more the nonlinear effect will affect the curve, as seen in past studies [70]. It is therefore safe to use the time range as being the last 25% of the trial, because the curve is smooth enough and close to the real values at the region of main interest.

Continuous Wave vs. Pulsed Signals

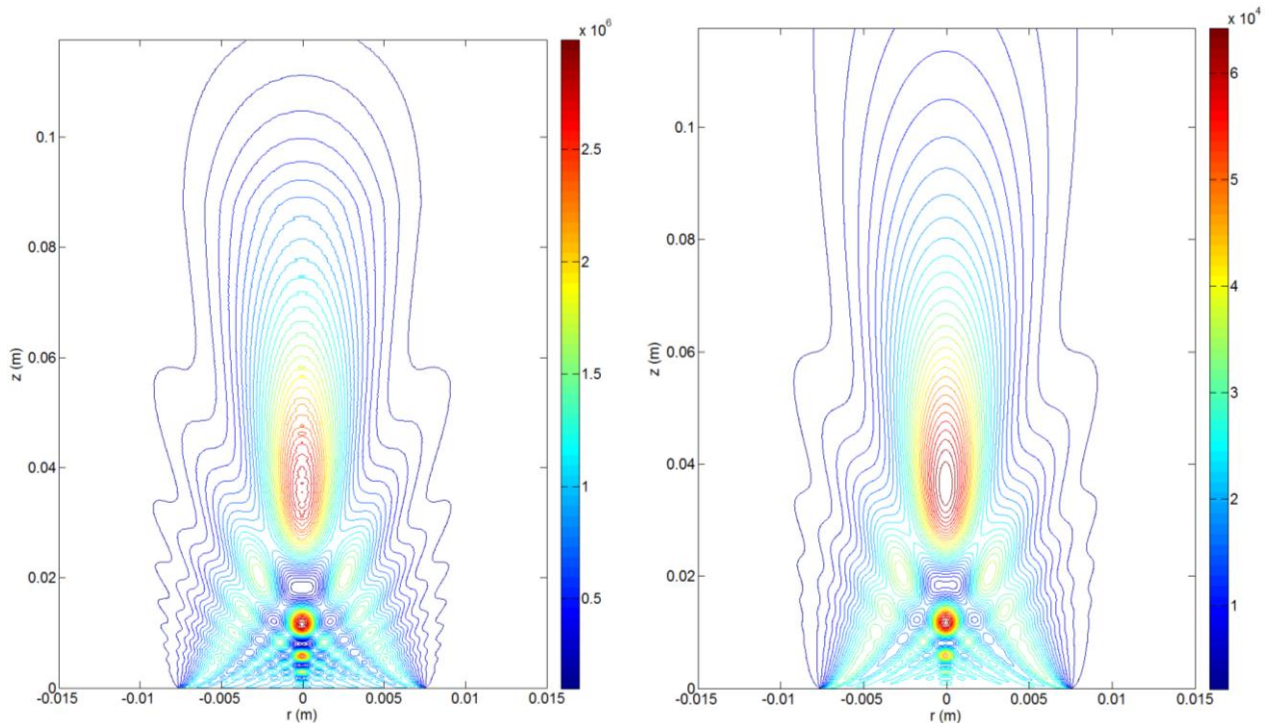


Figure 29 Contour Graphs For Volumetric Heat Generation Fields $P_o=0.5 \text{ MPa}$, $f=1 \text{ MHz}$, $R_s=7.5 \text{ mm}$, Left: CW Signal, Right: Pulsed Signal, $T_o=0.1 \mu\text{s}$ DF=0.35%

Figure 29 shows the contour graphs of resultant volumetric heat generations of the same 0.5 MPa and 1MHz signal with the same source unfocused radius of 7.5 mm. The difference is that one of

these signals is modulated by an envelope of a $0.1 \mu\text{s}$ length as opposed to it being a continuous wave. The smoothness of the volumetric heat generation for the pulsed signal occurs because the time range has to be the complete trial time. In other words, in Eq. 60 the iteration number $n_1 = 0$, because ramping effects cannot be ignored.

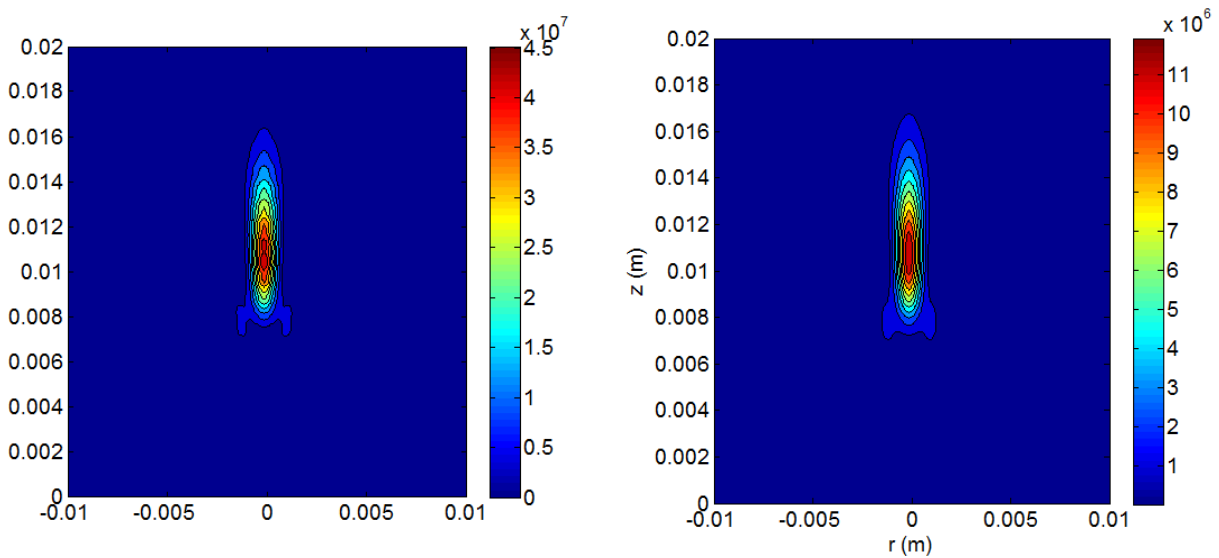


Figure 30 Contour Graphs For Volumetric Heat Generation Fields $P_o=0.25 \text{ MPa}$, $f=1 \text{ MHz}$, $R_s= 10\text{mm}$, $\epsilon = 11.20 \text{ mm}$; Left: CW Signal, Right: Pulsed Signal, DF=0.25%

As discussed before, modulating of the pressure amplitude does not affect either the shape pressure and heat generation field. The entire shape for the graphs shown in Figure 29 does not change. This is also shown in Figure 30 for focused sources, where a significant difference in the maximum volumetric heat generation, but identical location, can be seen.

Temperature

With the use of the calculated heat generation fields, proper selection of the parameters for grid coarsening will be chosen. The temperature rise induced by focused and unfocused sources with different signals will then be shown and discussed by using the Klinger model, shown in Eq. 35. This will require setting the perfusion coefficient W_{pennes} to zero.

Moreover, the importance of blood perfusion will be evaluated for different tissue properties. For this evaluation, W_{pennes} will therefore be varied and the quantity of the stream function $\psi_{b_{i,j+1}}^n$ will be set to zero for each iteration n . The results for the temperature obtained from different perfusion coefficients will be compared.

Stability

In order to generate accurate results from the temperature analysis, the right values for $\Delta r'$ and $\Delta z'$ have to be obtained. Therefore, a proper grid independence study has to be performed. The values for N and M in Eq. 78 will be varied, and the maximum temperature (located at the focal point) will be recorded. These values can be easily recalled using Figure 31.

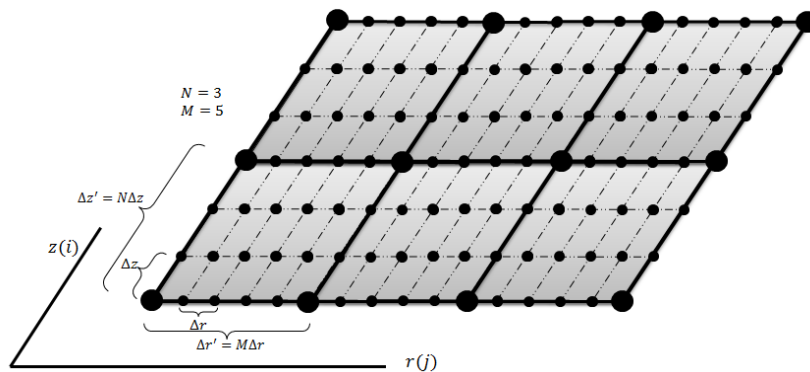


Figure 31 Schematic of Both Pressure and Temperature Grids Points Illustrating the Values of M and N

The maximum temperature for each case will then be compared to the maximum temperature obtained with the same grid as the one used for the pressure simulation (where $N = M = 1$). The values for N and M can only be odd according to the algorithm developed for coarsening the grid.

Table 4 Values for Maximum Temperature and Relative Error with Different values of N and M , induced by a 0.25 MPa and 1MHz continuous wave signal with a source radius of 8 mm for 30 s

N	M	$\Delta z'$ [mm]	$\Delta r'$ [mm]	$\Delta t'$ [s]	i_{max}'	j_{max}'	Total Nodes	T_{max} [C]	Error [%]
1	1	0.1	0.1	0.002	1340	191	255940	39.9659	0
1	3	0.1	0.3	0.0036	1340	64	85760	39.9888	0.057299
1	5	0.1	0.5	0.0038	1340	38	50920	40.025	0.147876
1	7	0.1	0.7	0.0039	1340	27	36180	40.0696	0.259471
1	9	0.1	0.9	0.0039	1340	21	28140	40.1182	0.381075
3	1	0.3	0.1	0.0036	447	191	85377	39.9659	0
3	3	0.3	0.3	0.018	447	64	28608	39.9895	0.05905
3	5	0.3	0.5	0.0264	447	38	16986	40.0259	0.150128
3	7	0.3	0.7	0.0303	447	27	12069	40.071	0.262974
3	9	0.3	0.9	0.0323	447	21	9387	40.1193	0.383827
5	1	0.5	0.1	0.0038	268	191	51188	39.9655	0.001001
5	3	0.5	0.3	0.0264	268	64	17152	39.9893	0.05855
5	5	0.5	0.5	0.0499	268	38	10184	40.0258	0.149878
5	7	0.5	0.7	0.066	268	27	7236	40.0717	0.264726
5	9	0.5	0.9	0.0762	268	21	5628	40.1196	0.384578
7	1	0.7	0.1	0.0039	191	191	36481	39.9663	0.001001
7	3	0.7	0.3	0.0303	191	64	12224	39.9904	0.061302
7	5	0.7	0.5	0.066	191	38	7258	40.0276	0.154382
7	7	0.7	0.7	0.0977	191	27	5157	40.0747	0.272232
7	9	0.7	0.9	0.1217	191	21	4011	40.1226	0.392084
9	1	0.9	0.1	0.0039	149	191	28459	39.965	0.002252
9	3	0.9	0.3	0.0323	149	64	9536	39.9889	0.057549
9	5	0.9	0.5	0.0762	149	38	5662	40.0256	0.149377
9	7	0.9	0.7	0.1217	149	27	4023	40.073	0.267978
9	9	0.9	0.9	0.1614	149	21	3129	40.1205	0.38683
11	1	1.1	0.1	0.004	122	191	23302	39.9655	0.001001
11	3	1.1	0.3	0.0334	122	64	7808	39.9886	0.056798
11	5	1.1	0.5	0.0826	122	38	4636	40.0281	0.155633
11	7	1.1	0.7	0.139	122	27	3294	40.0712	0.263475
11	9	1.1	0.9	0.1933	122	21	2562	40.1264	0.401592
13	1	1.3	0.1	0.004	103	191	19673	39.9653	0.001501

13	3	1.3	0.3	0.0341	103	64	6592	39.9895	0.05905
13	5	1.3	0.5	0.0868	103	38	3914	40.0269	0.15263
13	7	1.3	0.7	0.1514	103	27	2781	40.0757	0.274734
13	9	1.3	0.9	0.218	103	21	2163	40.124	0.395587

Table 4 shows different temperature trials induced a 0.25 MPa and 1MHz continuous wave signal with a source radius of 8 mm for 30 s. The error with respect to the real maximum temperature (last column from left to right) is small, and it is due to the fact that the volumetric heat transfer field is changing to the new grid size and therefore adapting to the temperature simulation. It has to be recalled that the heat generation is not obtained by any function, but it is interpolated for every new grid point. It is therefore expected to obtain small changes in maximum temperature.

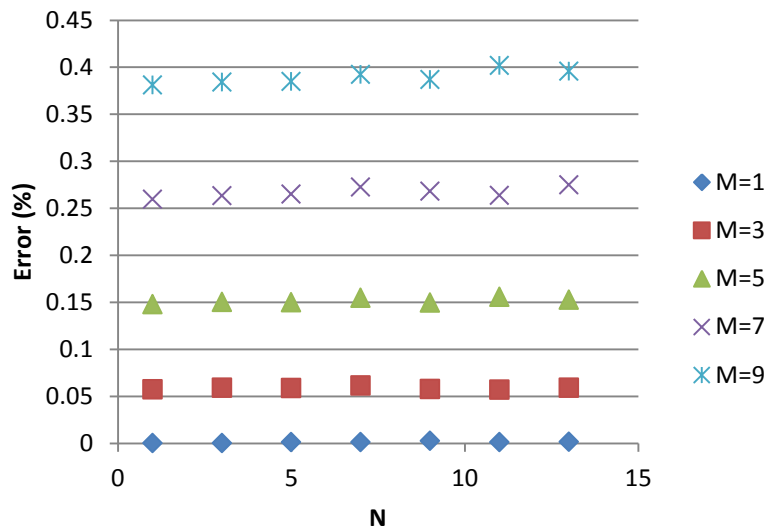


Figure 32 Graph of The Relative Error vs. N for Different values of M (Increasing values of these two numbers leads to decrease in the overall amount of nodes)

However, Figure 32 shows that the maximum temperature is more sensitive for changes in the value of $\Delta r'$ (increments in M) than for $\Delta z'$ (increments in N). In other words, changing the value of M produces greater error percentage than by changing the value of N . Moreover, changing the value of M does not decrease the total number of nodes as much as changing the value of N , as seen in Table 4.

This happens because there are steeper volumetric heat generation gradients in the radial direction than in the propagation direction (especially near the z –axis, where r gets closer to 0). It is therefore important to keep a roughly high number of nodes for the r direction and therefore a small number for M . The number of nodes for the z direction can be decreased with significantly more freedom, even though the entire propagation length L is much greater than the radial length R . It shows good numerical stability and N can therefore be a higher number. Based on these results, a value of $N = 13$ and $M = 3$ will be used for appropriate error margin.

Unfocused Sources

Figure 33 shows the temperature field for a 1MPa and 1MHz signal induced by a source radius of 8 mm at various times. The maximum temperature at a time of 40s occurs at a distance $z_{T_{max}} = 0.0442$, which agrees with the linear theory of acoustics regarding the location of the focal point for unfocused sources. The value for this location obtained by using Eq. 87 is $z_{FP} = 0.0427$.

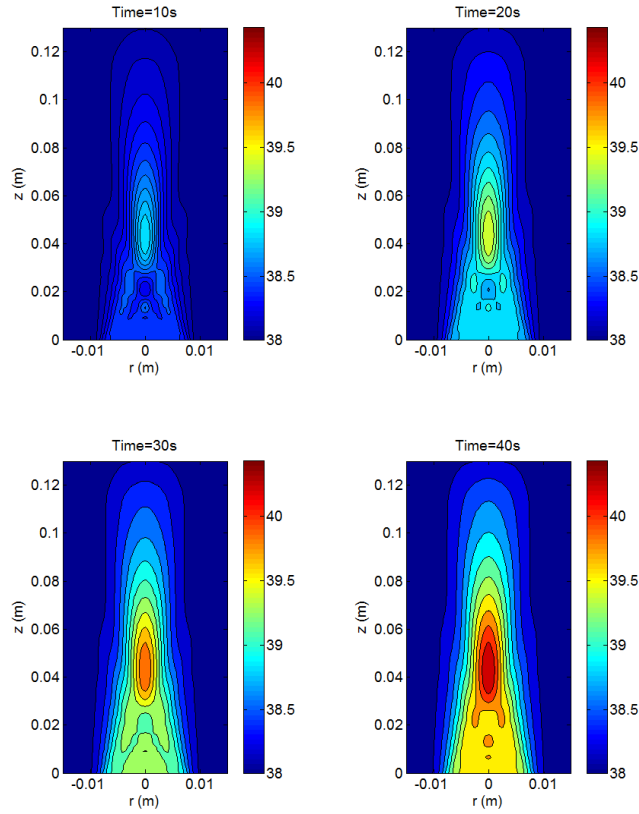


Figure 33 Contour Graph for Temperature Field at Different Times for an Unfocused Source
 $P_0=0.25 \text{ MPa}$, $f=1 \text{ MHz}$, $R_s= 8\text{mm}$ $ka=33.51$

The region near the transducer's face, also known as the nearfield (with a distance closer to the source than $z_{T_{max}}$), is rising in temperature at almost the same rate as the focal point. This is due to the volumetric heat generated at this region, which increases with ka number, as shown in Figure 34 (where the ka number increases due to an increment in the source radius).

This was expected according to the results found for the pressure field, which suggested that Eq. 87 was valid only for values less than a ka number of 28.4 and this signal has one of 33.51.

Figure 34 shows the temperature field for an unfocused source delivering a 1MPa and 1MHz signal at a source radius of 10 mm, resulting in a ka number of 41.88. The slight decrease in the

focal point's temperature, as well as the overall increase in the nearfield's temperature, is enough to prove that increments in the ka number are not a factor in the validity of Eq. 87 but it does weaken the focal point of the signal.

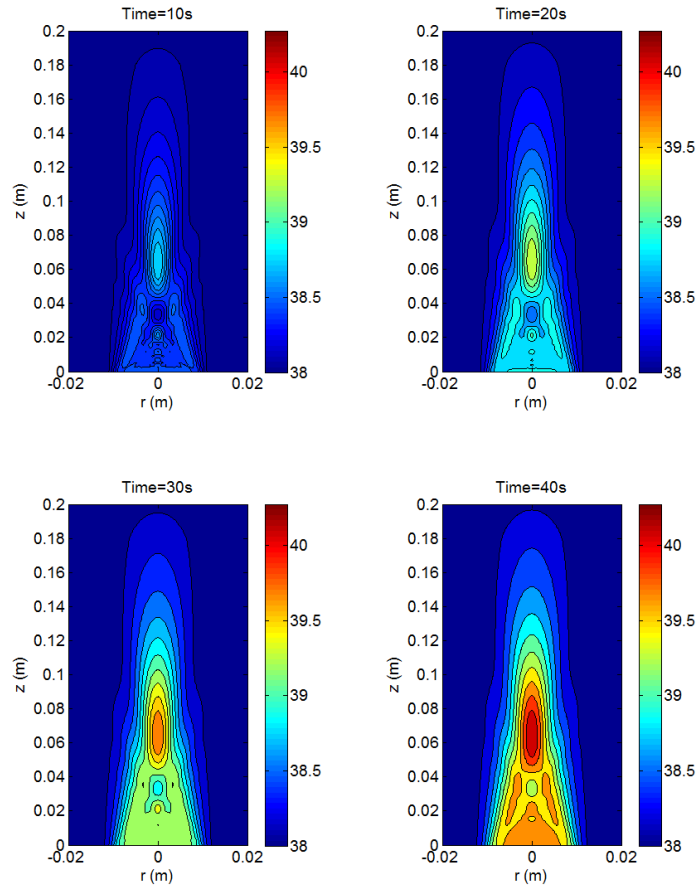


Figure 34 Contour Graph for Temperature Field at different Times for an Unfocused Source $P_0=0.25$ MPa, $f=1$ MHz, $R_s= 10$ mm $ka=41.88$

One reason the focal point might also get weakened is because of diffusion with time. This is further illustrated in Figure 35, where the rate of change of temperature with respect to time for the trial with the 8 mm source radius is shown. Because the boundary condition at $z = 0$ is

insulated, the temperature at the nearfield takes longer to reach a steady state than the temperature at the focal point or deeper (farfield).

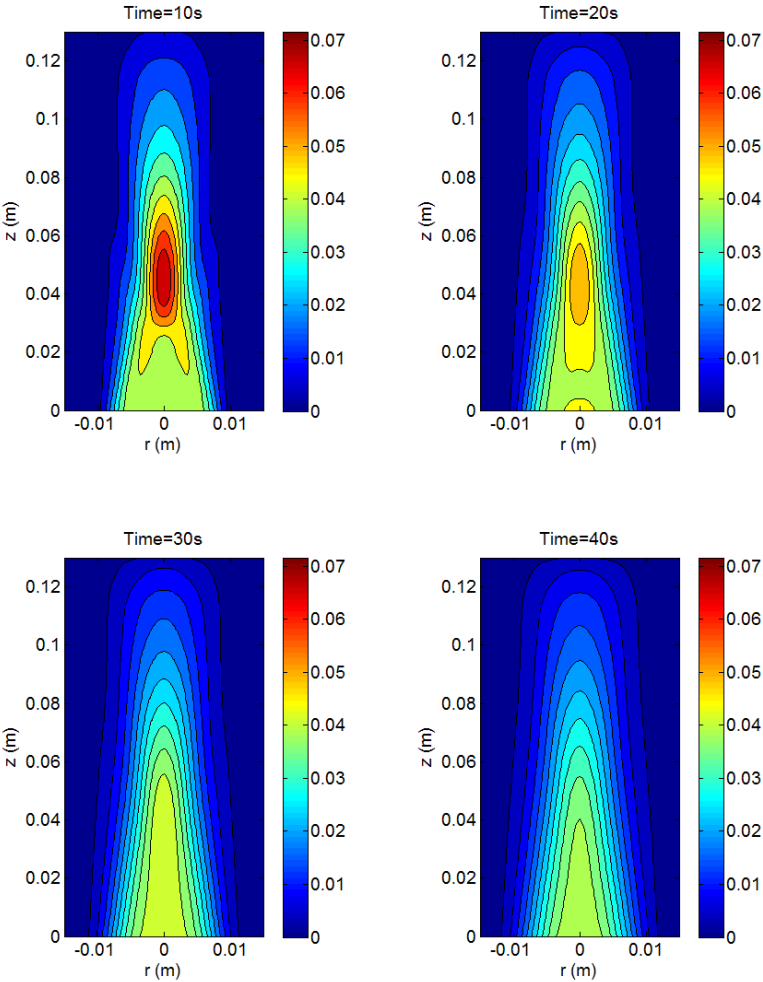


Figure 35 Contour Graph for the rate of change of the Temperature Field at different Times for an Unfocused Source $P_o=0.25 \text{ MPa}$, $f=1 \text{ MHz}$, $R_s= 8 \text{ mm}$

It can be concluded that, regardless of the value of ka , the focal point will get weaker with time. However, larger values of ka , there is a significant amount of heat generated that causes

significant temperature increments in the nearfield and accelerates the process of weakening the focal point.

Focused Sources

By comparing both Figure 34 and Figure 36, it can be seen that the maximum temperatures for unfocused and focused sources are significantly different. The maximum temperature induced by the focused source at an application time of 20s is roughly 25°C greater than the one induced by the unfocused source at 40s of application.

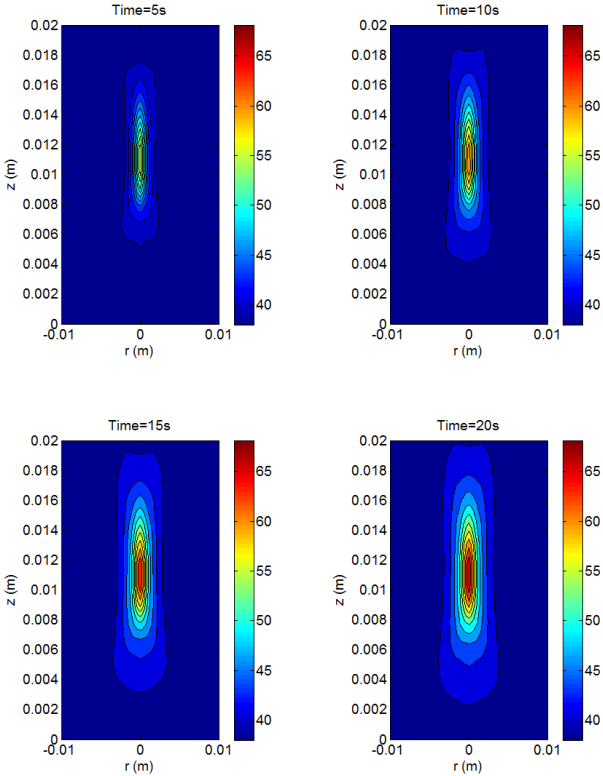


Figure 36 Contour Graph for Temperature Field at different Times for a Focused Source $P_0=0.25\text{ MPa}$, $f=1\text{ MHz}$, $R_s= 10\text{mm}$, $\epsilon = 11.20\text{ mm}$

As expected, pulsed signals delivered by focused sources results in temperature fields with the same shape as the ones obtained with continuous wave signals by the same type of source. However, these have significantly lower overall temperatures, as shown in Figure 37.

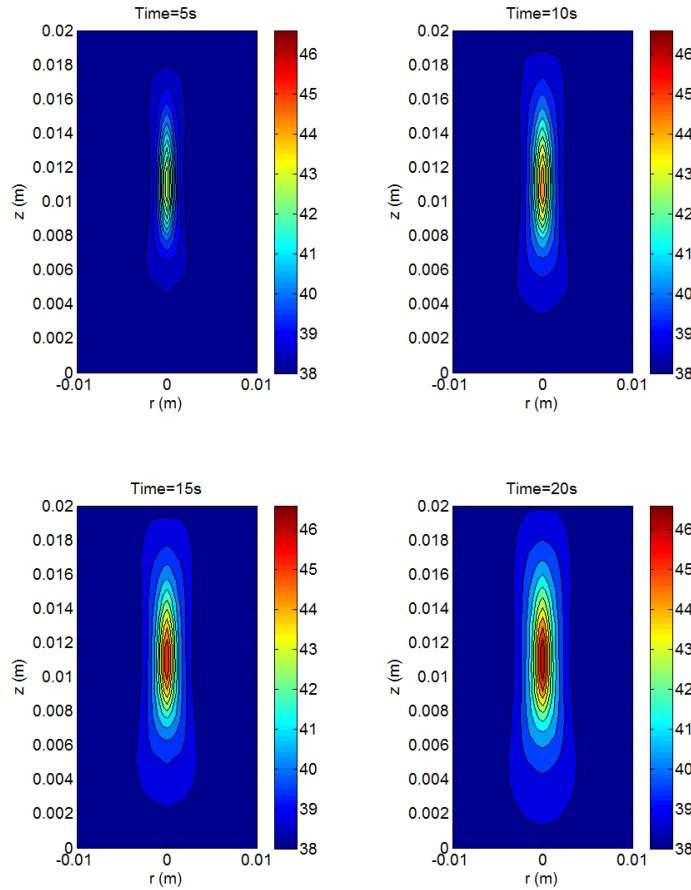


Figure 37 Contour Graph for Temperature Field at different Times for a Focused Source $P_0=0.25\text{ MPa}$, $f=1\text{ MHz}$, $R_s=10$, $\epsilon = 11.20\text{ mm}$, $DF=0.25\%$

The temperature field induced by focused sources does not suffer from the weakening of the focal point discussed for unfocused transducers. This can be again seen in Figure 38, which shows a contour graph of the temperature field obtained by a 0.25 MPa and 1 MHz signal with a focused source of $R_s=10\text{ mm}$ and $\epsilon = 11.20\text{ mm}$.

The rate of change of temperature with respect to time in the nearfield induced by this source is negligible with respect to the one induced at the focal point. Moreover, this field stays fairly constant compared to the one induced by unfocused sources.

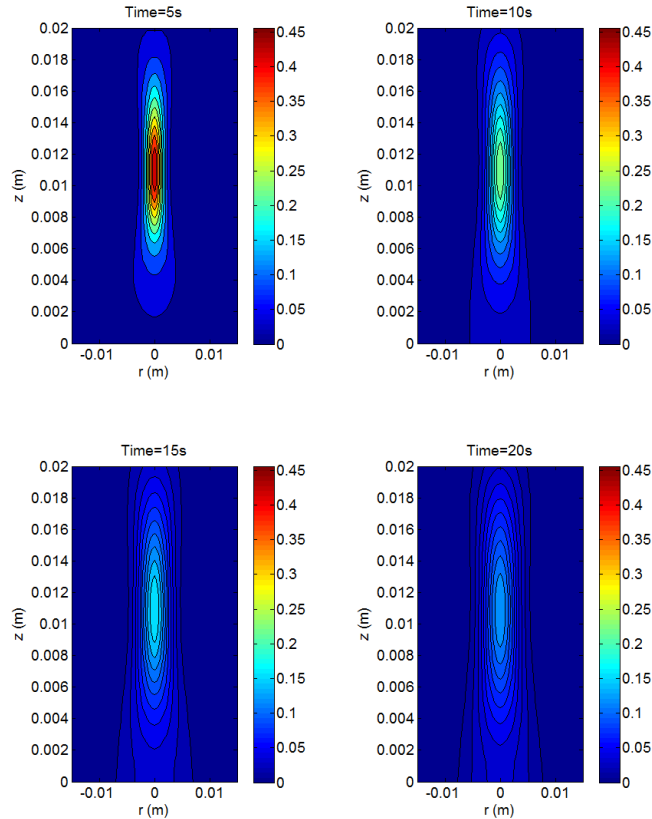


Figure 38 Contour Graph for the rate of change of the Temperature Field at different Times $P_0=0.25 \text{ MPa}$, $f=1 \text{ MHz}$, $R_s= 10\text{mm}$ $\epsilon = 11.20 \text{ mm}$

Effect of Advection and Viscous Dissipation

As stated earlier, the effects of advection and viscous dissipation depend of the flow of blood inside the porous medium. The velocity of this flow is described by Darcy's model for a porous medium, shown in Eq. 36.

It has to be noted that the flow might be dependent on factors such as acoustic streaming, large vessels, etc. By using Darcy and Klinger models, this study attempts analyze the behavior and importance of buoyancy driven flow in ultrasonic applications. In order to do so, the resulting stream function due to the temperature gradients present in the field has to be analyzed.

Figure 39 shows the streamlines of a field for a 1MPa and 1MHz signal induced by a source of radius 10 mm. The resultant temperature field of this signal is shown in Figure 34. It can be seen that the circulation of the flow happens at the nearfield and at a radial distance r equal to the diameter of the transducer.

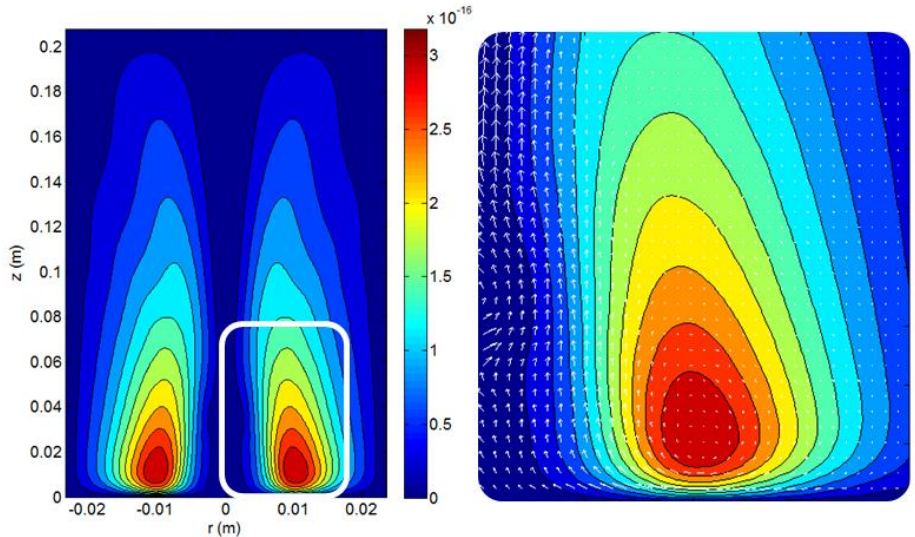


Figure 39 Left: Contour Graph of Streamlines for an Unfocused Source $P_0=0.25 \text{ MPa}$, $f=1 \text{ MHz}$, $R_s=10 \text{ mm}$ Time=40s; Right: Closed-Up of Enclosed Area with Velocity Vectors Included

Results obtained from focused sources are significantly different. Figure 40 shows the streamlines of a field for a 1MPa and 1MHz signal delivered by a focused source radius of $R_s=$

10mm and $\epsilon = 11.20 \text{ mm}$. The resultant temperature field of this signal is shown in Figure 36.

The circulation in this field happened at a distance equal to the focal point. Regardless of the shape of the field, the magnitude of the streamlines is practically negligible.

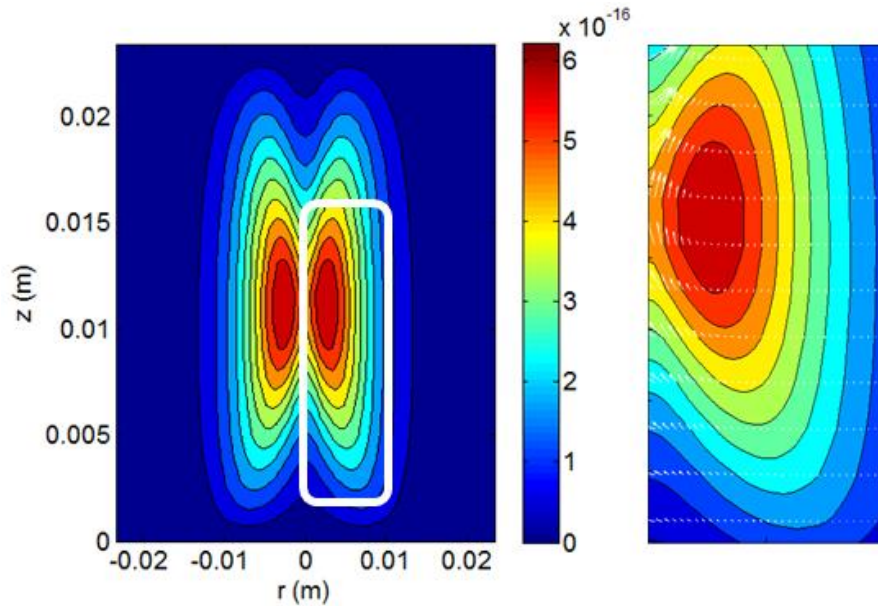


Figure 40 Left: Contour Graph of Streamlines for a Focused Source $P_0=0.25 \text{ MPa}$, $f=1 \text{ MHz}$, $R_s=10 \text{ mm}$ $\epsilon = 11.20 \text{ mm}$ Time=20s; Right: Closed-Up of Enclosed Area with Velocity Vectors Included

Figure 41 shows the temperature field for an unfocused source delivering a 1MPa and 1MHz signal at a source radius of 10 mm, without taking into account porous properties. In other words, the advection and viscous dissipation terms are not taken into account and the tissue is treated as a solid without blood flowing ($\psi = 0$).

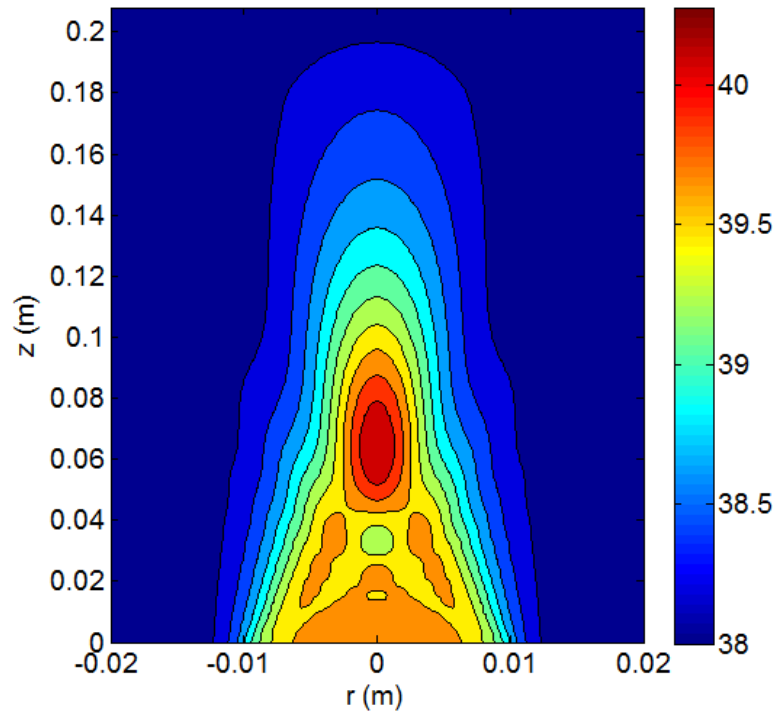


Figure 41 Contour Graph for the Temperature Field for an Unfocused Source $P_o=0.25 \text{ MPa}$, $f=1 \text{ MHz}$, $R_s= 10\text{mm}$, Time=40s, for the Case $\psi = 0$

It can be seen that the differences between this field and the one shown in Figure 33 are almost negligible. Figure 42 shows the difference percentage for every node, and it shows that the region where the temperature changes the most is around the edge of the source. The area around the focal point shows some change which is expected due to the temperature gradients in the z direction above and below the maximum temperature.

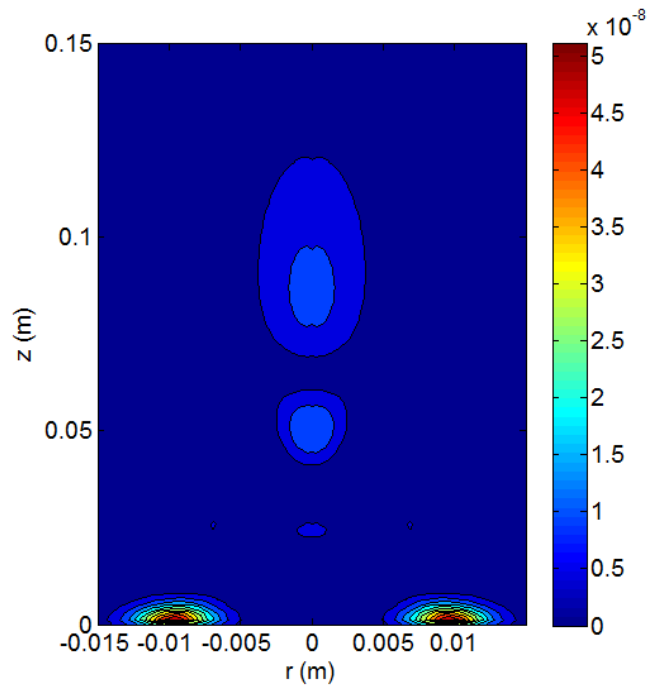


Figure 42 Contour Graph for the Temperature Field Percentage Difference in between Porous and Nonporous Media for an Unfocused Source $P_o=0.25 \text{ MPa}$, $f=1 \text{ MHz}$, $R_s= 10\text{mm}$, Time= 40s

The temperature field for focused sources does not change its shape significantly either. Figure 43 shows the temperature field for an unfocused source delivering a 1MPa and 1MHz signal delivered by a source radius of 10 mm with a focal point $\epsilon = 11.20 \text{ mm}$ for 20 s, without taking into account porous properties.

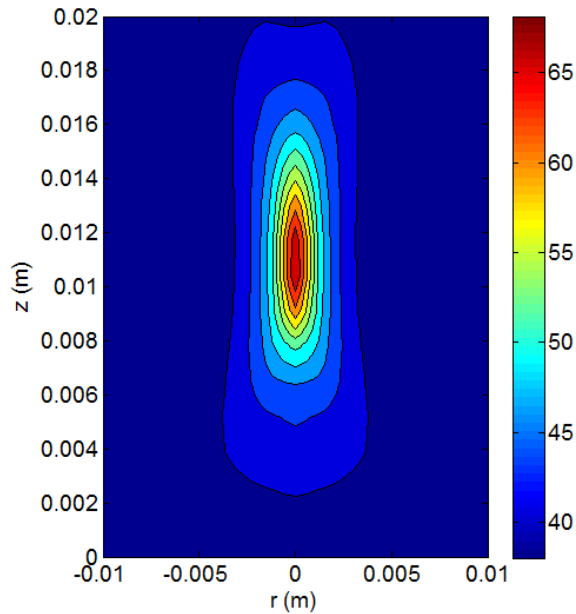


Figure 43 Contour Graph for the Temperature Field for an Focused Source $P_o=0.25 \text{ MPa}$, $f=1 \text{ MHz}$, $R_s=10 \text{ mm}$, $\epsilon = 11.20 \text{ mm}$, Time= 20 s , for the Case $\psi = 0$

However, it can be seen in Figure 44 that the difference in temperature for porous and nonporous models increases drastically for focused sources. Even though this change is still negligible, it can be concluded that focused sources lead to higher heat dissipation by advection and viscous dissipation. Other application (not medical) where the temperature of the medium is raised to significantly higher levels, or has higher levels of permeability, might need to take this factor into account.

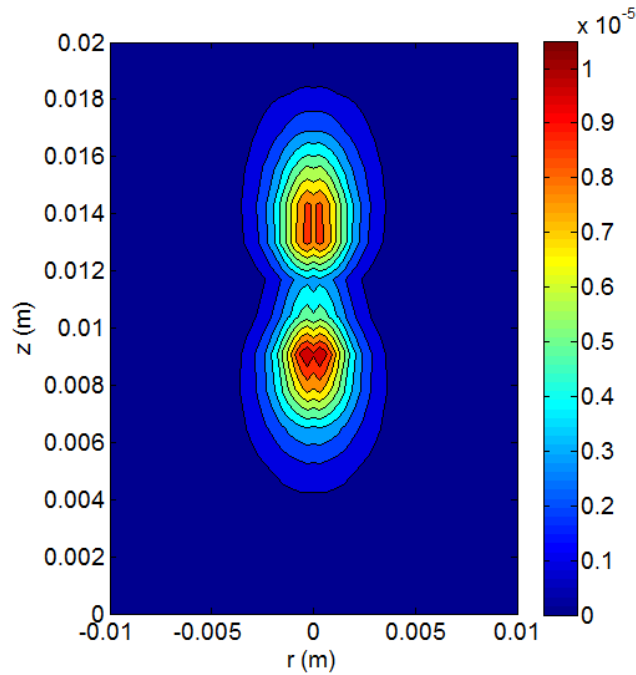


Figure 44 Contour Graph for the Temperature Field Percentage Difference in between Porous and Nonporous Media for a Focused Source $P_0=0.25 \text{ MPa}$, $f=1 \text{ MHz}$, $R_s= 10\text{mm}$, $\epsilon = 11.20 \text{ mm}$, Time= 20s

This negligible heat dissipation is also in part due to the very low permeability levels of tissue. It can be therefore concluded that the buoyancy driven terms do not affect the temperature field. Further experimentation regarding other factors that lead to blood flow is needed in order to understand the Klinger model further. Understanding this model will lead to conclude if its extra terms are needed for proper description of the temperature field.

Effect of Blood Perfusion

Up to this point, the Pennes model has not been used to describe any of the results for the temperature field. In other words, the coefficient of blood perfusion W_{pennes} has been considered to be zero, and therefore only the Klinger model has been used. This means that all the past results obtained either diffused the heat generated by conduction, viscous dissipation, advection, or stored it (which in turn raised the temperature of tissue).

As already discussed, the heat diffused by advection and viscous dissipation for the model used is a product of the blood circulating in the extravascular region and does not have any relationship with the micro channels (or vascular region) shown in Figure 9. The velocity of the flow was strictly only because of buoyancy driven effects.

The Pennes model assumes that enough blood with a certain temperature T_{∞} is successfully flowing in and out of the region of interest. This assures that there is a clear difference between T_{∞} and T_b .

Comparing the temperature fields obtained with the use of different values W_{pennes} will define its importance when describing temperature fields due to heat generation. Eq. 74 will be used while setting the value $\psi_{i,j}^n = 0$.

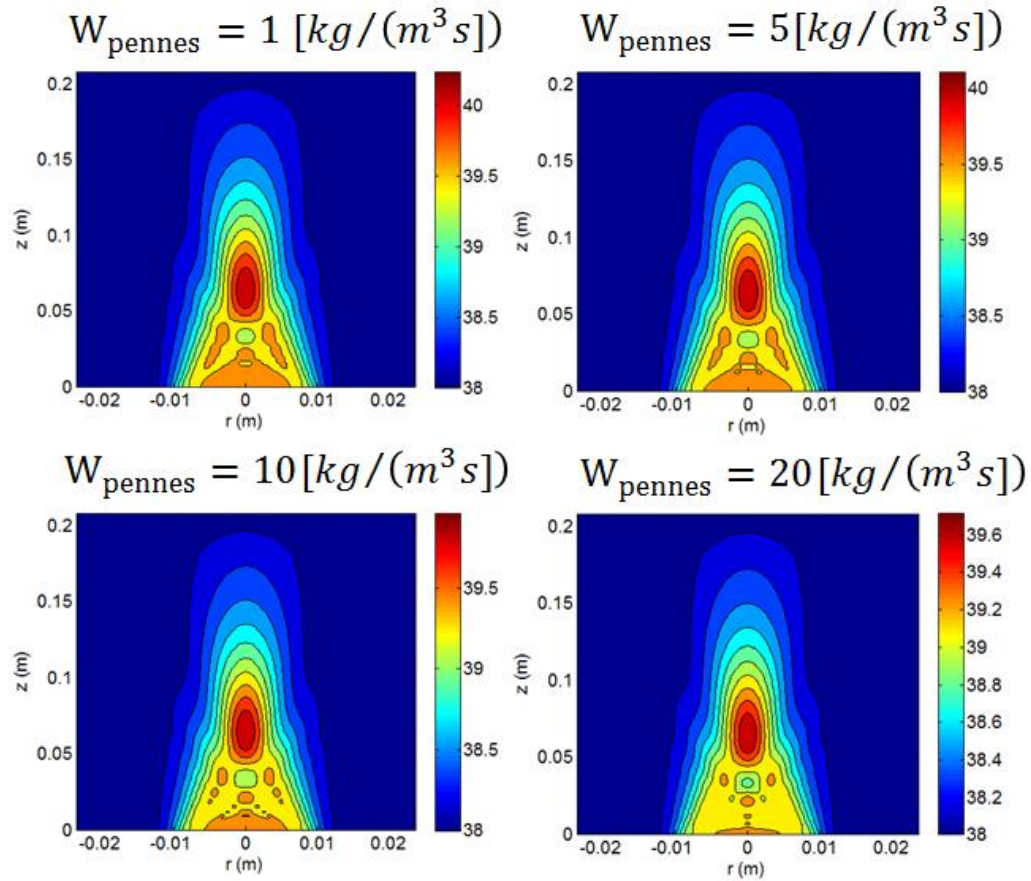


Figure 45 Contour Graphs for the Temperature Field delivered by an Unfocused Source $P_o=0.25 MPa$, $f=1 MHz$, $R_s= 10mm$, Time=40s, for different Cases of W_{Pennes}

It can be seen in Figure 45 that the temperature fields do not vary as much in shape with varying W_{Pennes} . However, a decrement of the overall temperature is evident, as further illustrated by Figure 46, which shows the temperature difference between the fields generated with the use of different values for W_{Pennes} and the one where perfusion is ignored (shown in Figure 41).

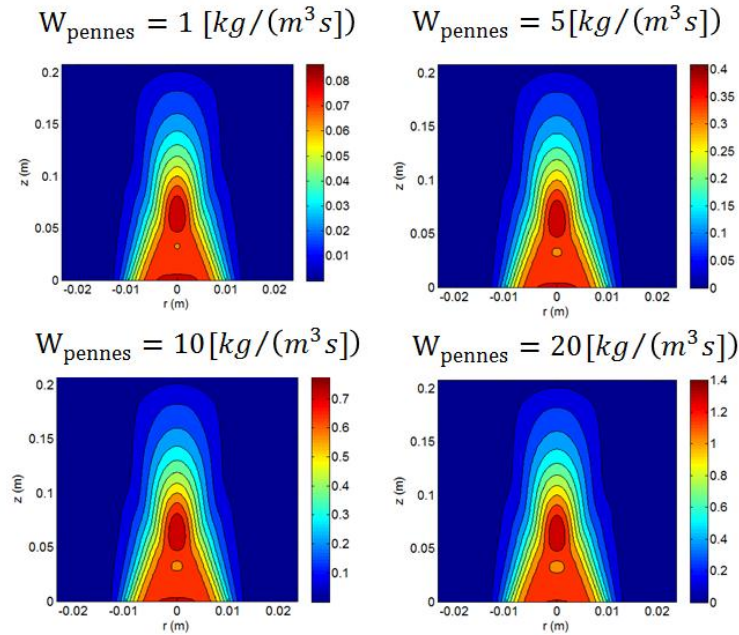


Figure 46 Contour Graphs for the Changes in Temperature Field with respect to the field in Figure 41 delivered by an Unfocused Source $P_0=0.25 \text{ MPa}$, $f=1 \text{ MHz}$, $R_s= 10\text{mm}$, Time=40s, for Different Cases of W_{Pennes}

The values used for the perfusion coefficient would correspond to velocities significantly higher than the ones obtained only by buoyancy driven forces. As stated earlier, this perfusion term describes heat being carried away by blood flowing in micro channels (which are representing the vascular region). Regardless of its value, the regions where the temperature changes occur do not agree with Klinger’s model.

Mathematical Relationship between Maximum Pressure and Signal Parameters for Unfocused Sources

Results for the resultant pressure of unfocused sources showed that the ka number was the ultimate factor in defining the pressure field and location of the focal point. Figure 24 showed that for different transducer sizes and frequencies, the normalized pressure field is identical given that both the ka numbers are the same.

According to Eq. 87 and Eq. 88 , the location of the focal point can easily be related to the transducer size by Eq. 90.

Even though it was shown that this relationship stops working for ka numbers greater than 28.4, the analysis for temperature showed that the maximum temperature is still located at Z_{FP} . The effect of increases the ka was mainly the weakening of the focal point.

$$Z_{FP} = \left(\frac{ka}{2\pi}\right) R_s \quad \text{Eq. 90}$$

Eq. 90 shows that the location of the focal point can be approximated with the ka number. It therefore makes it tempting to also find a relationship that approximates the pressure at the focal point P_{FP} obtained at this location with the ka number.

In order to find a relationship, various trials for different frequencies f , source pressure P_o , and source radii R_s where performed. The frequency, pressure, and source radius was varied from 0.8

to 1.2 MHz in 0.1 MHz increments, 0.1 to 1 MPa in 0.25 increments, and 5 to 10 mm, in 1 mm increments, respectively.

The values for the ka number and P_{FP} were recorded. Moreover, all the resulting data obtained for P_{FP} , for every combination of the parameters specified, was scattered with respect to the ka number.

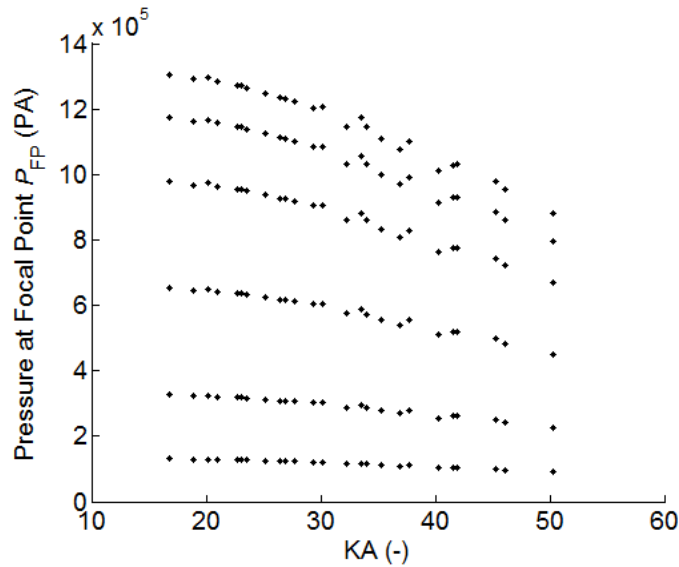


Figure 47 Scatter plot of Pressure at the Focal Point P_{FP} vs. ka number. Data points were obtained from various experiments with different values for signal frequency f , source Pressure P_o , and source radii R_s

Figure 47 shows the result of this scattered plot. It can be seen that various source pressures are tested, leading to multiple values of P_{FP} (one for each different source pressure), for single values of the ka number. It was expected to note that there is no clear and direct relationship

between P_{FP} and ka . However, plotting the quantity Θ (shown in Eq. 91) with respect to the ka number leads to a clear relationship, as shown in Figure 48.

$$\Theta = \frac{P_{FP}}{P_o ka} \quad \text{Eq. 91}$$

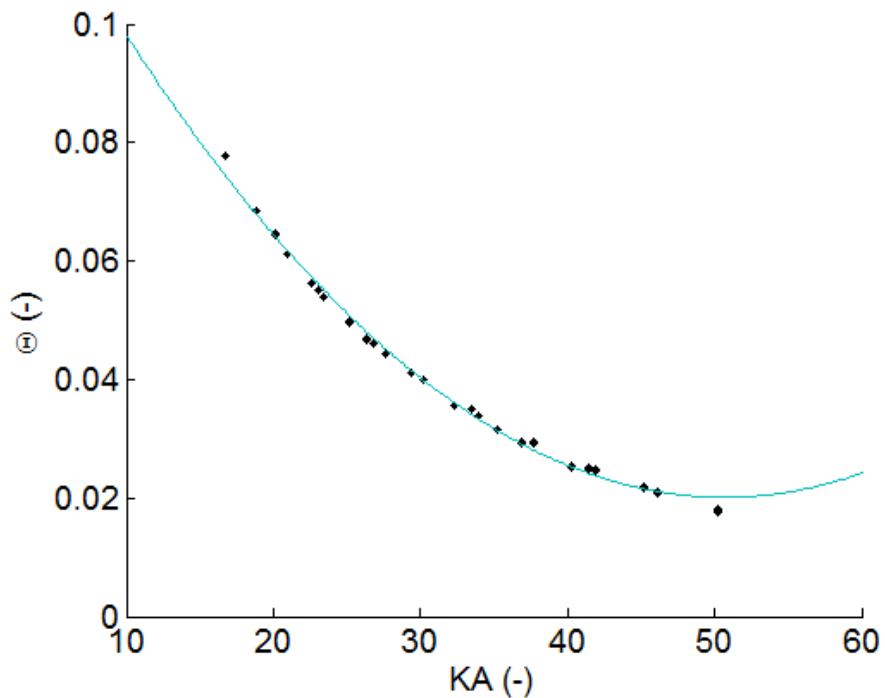


Figure 48 Scatter plot of quantity Θ vs. ka number. Data points were obtained from various experiments with different values for signal frequency f , source Pressure P_o , and source radii R_s

The model obtained for this relationship was developed by the method of least squares. The function obtained for Θ was transformed back to P_{FP} and the result is shown in Eq. 92, yielding a norm of the residuals of 0.028987, an error value r^2 of 81.78%.

$$P_{FP} = 4.7 \times 10^{-5} P_o (ka)^3 - 0.0047 P_o (ka)^2 + 0.14 P_o ka$$

This clear relationship is a useful approximation for calculating the pressure at a certain focal point an unfocused source with a certain radius R_s is able to deliver. In cases where a specific source radius is given and a certain location Z_{FP} and maximum pressure P_{FP} are desired, the values for f and P_o can be adjusted to satisfy the specifications given.

It has to be noted that the coefficients obtained will vary with other parameters considered to be constant properties of tissue, such as the nonlinearity coefficient β , the diffusion coefficient δ , small signal sound speed c_o , etc. The method used in this experiment has to be performed for different types of tissue in order for the relationship to be accurate.

Mathematical Relationship between Maximum Volumetric Heat Generation and Signal Parameters for Unfocused Sources

A similar relationship regarding the maximum volumetric heat generated \dot{Q}_{FP} and its location will be as useful as the relationship just found for P_{FP} . Similarly to the procedure done earlier, the frequency, pressure, and source radius was varied from 0.8 to 1.2 MHz in 0.1 MHz increments, 0.1 to 1 MPa in 0.25 increments, and 5 to 10 mm, in 1 mm increments, respectively. The values for the ka number and \dot{Q}_{FP} , were recorded and scattered in the same fashion.

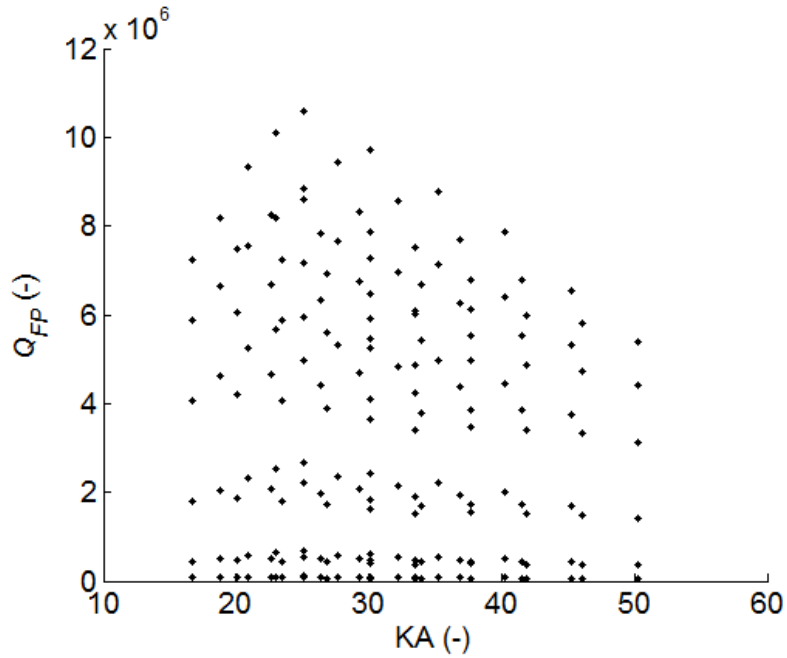


Figure 49 Scatter plot of Heat Generation at the Focal Point \dot{Q}_{FP} vs. ka number. Data points were obtained from various experiments with different values for signal frequency f , source Pressure P_o , and source radii R_s

It can be seen on Figure 49 that there is no clear relationship between \dot{Q}_{FP} and the ka number. However, if the quantity Γ , shown in Eq. 93, is plotted with respect to the ka number, another model is obtained, which is shown in Figure 50.

$$\Gamma = \ln\left(\frac{\dot{Q}_{FP}}{P_o^2 k \alpha^2 f}\right) \tag{Eq. 93}$$

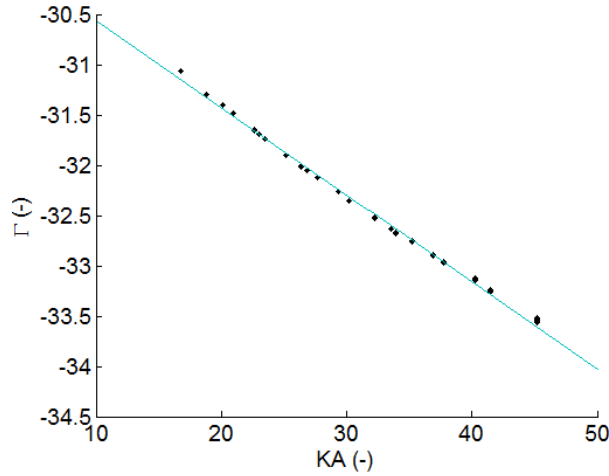


Figure 50 Scatter plot of quantity Γ vs. ka number. Data points were obtained from various experiments with different values for signal frequency f , source Pressure P_o , and source radii R_s

The model obtained was again transformed back into \dot{Q}_{FP} and the results are shown in Eq. 94.

The norm of residuals obtained was 1.1162, and the r^2 value was 98 %.

Eq. 94

$$\dot{Q}_{FP} = P_o^2 ka^2 f e^{-(0.085 ka + 29.747)}$$

It can be seen that this value depends not only on the ka number, but on frequency too. This is because the coefficient of absorption is dependent on the frequency as shown in Eq. 26. The value obtained by this model is very useful for the same types of purposes as the model shown in Eq. 92.

It can be concluded that, with use of the models presented, the location of the focal point and its overall volumetric heat generated can be approximated for a certain prescription of ultrasonic

parameters. These models have not been validated and proper experimentation already discussed is needed in order to do describe its accuracy.

Chapter 5: Conclusion

The main objective of this study was to inspect the relationships between prescribed ultrasonic parameters and its resulting effects in soft tissue. Moreover, heat dissipation in the form of perfusion and natural convection was examined as a secondary objective of the study.

A numerical scheme coupling the pressure distribution, volumetric heat generation, temperature increment, and tissue damage, induced by different types of ultrasonic signals has been developed.

Relationships between the source parameters and the pressure propagation, volumetric heat generation, and temperature rise fields have been proposed.

Pressure Field

Results for the pressure field agreed with data from prior studies [26] [37]. The analysis showed that the prescribed signal was developing forward over time and not bouncing at the boundaries. The location of the maximum values obtained, for each field, and the theoretical focal point distance were compared.

Good agreement, with error percentage of less than 5% was shown for signals delivered by unfocused sources, for $ka < 28.4$. It was also shown that regardless of the source radius and frequency, the shape of the resulting pressure field will be identical for different sources and

signals provided that their ka number is the same. Moreover, a nonlinear relationship exists between the maximum and prescribed pressures, with the extent of nonlinearity increasing with increasing source pressure. However, it might be small enough to neglect for applications where the use of this relationship can be approximated and it does not affect the pressure distribution across the field.

For focused sources, the focal point location agreed with the one specified by the geometry of the source itself. Due to the fact that the equation used only works for directional beams, results for the focus gain did not agree with the coefficient used in analytical analyses, for situations where the aperture angle is too wide. The resulting pressure field was well defined and did not experience large pressure values in the near field, as opposed to the unfocused sources.

Heat Generation

Important conclusions regarding the choice of the time range for the average volumetric heat generation were drawn. Moreover, proper differences between pulsed and continuous wave signals in terms of the time range were specified. This was needed for proper coupling between the pressure and temperature analyses.

Temperature

Proper comparison between the Pennes and Klinger bioheat models was performed in order to understand which heat dissipation effects should be taken into account in the presence of ultrasound induced volumetric heat generation.

It was shown that the effects of viscous dissipation and advection are negligible for buoyancy driven flow. It was concluded that only the temperature fields for applications with significantly high temperature increments or high permeability will be affected.

The effect of perfusion was evaluated and it was concluded that increments in the perfusion coefficient lead to increments in temperature that do not change the shape of the temperature field. This result does not agree with Klinger model, where the shape of the temperature field does change with higher permeability constant.

Simple mathematical models relating values such as the pressure and volumetric heat generation at the focal point with the prescribed signal parameters were developed.

Final Thoughts

The study's hypothesis was proved to be correct. There exist a clear relationship between the prescribed parameters of ultrasonic sources and temperature rise. The information presented in this study helps identify which signal and source types are more useful than others, for different applications. For example, sonophoresis and lipolysis require the use of uniform and less intense signals that would be suitable for treatments using unfocused sources driving continuous wave signals. Other applications such as forced hyperthermia use focused sources to produce accurate

tissue lesions, while the duty factor of the pulsed signals can be used to control the rate of injury produced by the ultrasonic signal.

The main objective of this study was to increase awareness of the potential use of biomedical ultrasound in several applications. Moreover, the theory presented will allow the development of safer, more accurate devices. Areas of future work include further development of mathematical relationships including the geometry of focused sources and the duty factor as variables. Further research of the Klinger and Pennes models for ultrasonic applications, mostly regarding causes of blood flow other than buoyancy factors, is needed for proper modeling of the temperature field.

Appendix A: Nomenclature

a	Specific Surface Area	m^2	w	Velocity in the Radial Direction	$m s^{-1}$
c_o	Small Signal Sound Speed	$m s^{-1}$	W	Coefficient of Perfusion	kg
c_p	Specific Heat Capacity	$J K^{-1}$	z	Distance Propagation Coordinate	m
DF	Duty Factor	%	Z_r	Rayleigh Distance	m
g	Standard Gravity	$m s^{-2}$	Greek Symbols		
f	Frequency	Hz	α	Absorption Coefficient	Np/m
G	Geometric Gain	-	β	Nonlinearity Coefficient	-
h	Convection Coefficient	$W m^{-2} K^{-1}$	β	Coefficient of Thermal Expansion	K^{-1}
h	Rim Height	m	δ	Coefficient of Diffusivity	$m^2 s^{-1}$
I	Intensity	$W m^{-2}$	ε	Porosity	-
i	Index Value in Propagation Direction	-	ε	Geometrical Focal Point	m
j	Index Value in Radial Direction	-	θ	Aperture Angle	$^\circ$
k	Thermal Conductivity Coefficient	$W m^{-1} K^{-1}$	λ	Wavelength	m
k	Wavenumber	m^{-1}	μ	Viscosity	$kg m s^{-1}$
K	Permeability	m^2	ρ	Density	$kg m^{-3}$
ka	Nondimensional Number see Eq. 88	-	φ	Radius of Curvature	m
L	Length in the Propagation Direction	m	ψ	Stream Function	$m^2 s^{-1}$
m	Signal Waveform Coefficient	-			
M	Ratio of Temperature to Pressure	-			
M	Discretization in Radial Direction	-			
n	Number of Cycles	-			
N	Ratio of Temperature to Pressure	-			
N	Discretization in Propagation Direction	-			
P	Pressure	Pa			
\dot{Q}	Volumetric Heat Generation	$W m^{-3}$			
r	Distance Radial Coordinate	m			
R	Length in Radial direction	m			
R_s	Source Radius	m			
t	Time	s			
T	Temperature	C°			
T_o	Signal's Active Time	s			
T_{tot}	Wave's Propagation Time	s			
U	Velocity Vector	$m s^{-1}$			
u	Velocity in the Propagation Direction	$m s^{-1}$			
V	Volume	m^3			

Chapter 6: Bibliography

- [1] E. W. Wood and A. L. Loomis, "The Physical and Biological Effects of High-Frequency Sound Waves of Great Intensity," *Philosophical Magazine*, vol. 4, no. 22, pp. 417-436, 1927.

- [2] G. t. Haar, "Therapeutic Applications of Ultrasound," Vols. (93) 111-129, 2006.

- [3] A. Blana, B. Walter, S. Rogenhofer and W. F. Wienland, "High-intensity focused Ultrasound for the Treatment of Localized Prostate Cancer: 5-year Experience," *Urology*, vol. 63, no. 2, pp. 297-300, 2004.

- [4] L. Poissonnier, J.-Y. Chapelon, O. Rouviere, L. Curiel, R. Bouvier, X. Martin, J. M. Dubernard and A. Gelet, "Control of Prostate Cancer by Transrectal Hifu in 227 Patients," *European Urology*, vol. 51, no. 2, pp. 381-387, 2006.

- [5] P. Huber, J. Jenne, R. Rastert, L. Simiantonakis, H.-P. Sinn, H.-J. Strittmatter, D. v. Fournier, M. Wannemacher and J. Debus, "A New Noninvasive Approach in Breast Cancer Therapy Using Magnetic-Guided Focused Ultrasound Surgery," *Cancer Research*, vol. 61, p. 8441, 2001.

- [6] E. Postma, R. v. Hillergersberg, B. Daniel, L. Merckel, H. Verkooijen and M. v. d. Bosch, "MRI-Guided Ablation of Breast Cancer: Where do we stand Today," *Journal of Magnetic Resonance Imaging*, vol. 34, no. 2, pp. 254-261, 2011.

- [7] M. Nathan, C. Greg, B. Peter, J. Ferenc and H. Kullervo, "Transcranial MRI-Focused Ultrasound Surgery of Brain Tumors: Initial Findings in Three Patients," *Neurosurgery*, vol. 66, no. 2, pp. 323-332, 2010.

- [8] Z. Ram, Z. Cohen, S. Harnof, S. Tal, M. Faibel, D. Nass, S. Maier, M. Hadani and Y.

- Mardor, "Magnetic Resonance Image-Guided, High-Intensity Focused Ultrasound for Brain Tumor Therapy," *Neurosurgery*, vol. 59, no. 5, pp. 949-956, 2006.
- [9] M. Ersnt and A. J. Ferenc, "Noninvasive Treatment for Brain Tumors: Magnetic Resonance-Guided Focused Ultrasound Surgery," *Tumors of the Central Nerbous System*, vol. 3, no. 3, pp. 227-236, 2011.
- [10] T. Charrel, F. Aptel, A. Birer, F. Chavrier, F. Romano, J.-Y. Chapelon, P. Denis and C. Lafon, "Development of a Miniaturized HIFU Device for Glaucoma Treatment With Conformal Coagulation of the Ciliary Bodies," *Ultrasound in Medicine and Biology*, vol. 37, no. 5, pp. 742-754, 2011.
- [11] R. Rao and S. Nanda, "Sonophoresis: Recent Advancements and Future Trends," *Journal of Pharmacy and Pharmacology*, vol. 61, no. 6, pp. 689-705, 2009.
- [12] O. Dogu, D. Apaydin, S. Sevim, D. Talas and M. Aral, "Ultrasound-Guided versus 'Blind' Intraparotid Injections of Botulinum Toxin-A for the treatment of Sialorrhea in Patients with Parkinson's Disease," *Clinical Neurology and Neurosurgery*, vol. 106, no. 2, pp. 93-96, 2004.
- [13] J. Hindley , W. Gedroyc, L. Regan, E. Stewart, C. Tempany, K. Hynnen, N. Macdnold, Y. Inbar, Y. Itzchak, J. Rabinovici, K. Kim, J.-F. Geschwind, G. Hesley, B. Gostout, T. Ehrenstein, S. Hengst, M. Sklair-Levy, A. Shushan and F. Jolesz, "MRI Guidance of Focused Ultrasound Therapy of Uterine Fibroids: Early Results," *American Journal of Roentgenology*, vol. 183, no. 6, pp. 1713-1719, 2004.
- [14] G. Haar, "Therapeutic Ultrasound," *European Journal of Ultrasound*, vol. 9, no. 1, pp. 3-9, 1993.
- [15] P. Bhowmick, J. E. Coad, S. Bhowmick, J. L. Pryor, T. Larson, J. De La Rosette and J. C. Bischof, "In Vitro Assesment of the Efficacy of Thermal Therapy in Human Benign Prostatic Hyperplasia," *International Journal of Hyperthermia Vol.20 (4)*, pp. 421-439, 2004.
- [16] W. C. Dewey, "Arrhenius Relationships from the Molecule and Cell to the Clinic,"

International Journal of Hyperthermia, vol. 10, no. 4, pp. 457-483, 1994.

- [17] E. P. Armour and G. P. Raaphorst, "Long Duration Mild Temperature Hyperthermia and Brachytherapy," *International Journal of Hyperthermia*, vol. 20, no. 2, pp. 175-189.
- [18] A. Vander, J. Sherman and D. Luciano, *Human Physiology: The mechanism of Body Function*, Boston, Mass: McGraw Hill, 1998.
- [19] P. Abraham, G. Leftheriotis, B. Desvaux, M. Saumet and J. Saumet, "Diameter and Blood Velocity Changes in the Saphenous Vein during Thermal Stress," *European Journal of Applied Physiology and Occupational Physiology*, vol. 69, no. 4, pp. 305-3008, 1994.
- [20] D. Draper, S. Sunderland, D. Kirkendall and M. Ricard, "A Comparison of Temperature Rise in Human Calf Muscles following Applications of Underwater and Topical Gel Ultrasound," *Journal of Orthopaedic & Sports Physical Therapy*, vol. 17, no. 5, pp. 247-251, 1993.
- [21] K. Baker, V. Robertson and F. Duck, "A review of Therapeutic Ultrasound: Biophysical Effects," *Journal of the Physical Therapy Association*, vol. 81, pp. 1351-1358, 2001.
- [22] G. Haar, "Basic Physics of Therapeutic Ultrasound," *Physiotherapy*, vol. 73, pp. 110-113, 1987.
- [23] T. J. Dubinsky, C. Cuevas, M. K. Dighe, O. Kolokythas and J. H. Hwang, "High-Intensity Focused Ultrasound: Current Potential and Oncologic Applications," *American Journal of Roentgenology*, vol. 190, no. 1, pp. 191-199, 2008.
- [24] R. Hogan, K. Burke and T. Franklin, "The effect of ultrasound on microvascular hemodynamics in skeletal muscle: Effects during ischemia," *Microvascular Research*, vol. 23, no. 3, pp. 370-379, 1982.
- [25] I. M. Hallaj and R. O. Cleveland, "FDTD Simulation of Finite-Amplitude Pressure and Temperature fields of Biomedical Ultrasound," *J. Acoust. Soc. Am.*, 1999.

- [26] J. Huijssen, A. Bouakaz, M. D. Verweij and N. d. Jong, "Simulations of the Nonlinear Acoustic Pressure Field Without Using the Parabolic Approximation," *IEEE Ultrasonics Symposium*, vol. 2, pp. 1851-1854, 2003.
- [27] X. Liu, J. Li, X. Gong and D. Zhang, "Nonlinear Absorption in Biological Tissue for High Intensity Focused Ultrasound," *Ultrasonics*, vol. 44, pp. e27-e30, 2006.
- [28] V. A. Khokhlova, J. Tavakkoli, O. A. Sapozhnikov and D. Cathignol, "Numerical Modeling of Finite-Amplitude Sound Beams: Shock Formation in the Near Field of a CW Plane Piston Source," *Journal Acoustical Society of America*, vol. 110, no. 1, pp. 95-108, 2001.
- [29] Y. Makov, V. Morcillo, F. Camarena and V. Espinosa, "Nonlinear Change of on Axis Pressure and Intensity Maxima Positions and its Relation with the Linear Focal Shift Effect," *Ultrasonics*, vol. 48, pp. 678-686, 2007.
- [30] M. Canney, M. Bailey, L. Crum, V. Khokhlova and O. Sapozhnikov, "Acoustic Characterization of High Intensity Focused Ultrasound Fields: A combined Measurement and Modeling Approach," *Journal Acoustical Society of America*, vol. 124, no. 4, pp. 2406-2420, 2008.
- [31] I. Hallaj, R. Cleveland and K. Hynynen, "Simulations of the Thermo-Acoustic Lens Effect During Focused Ultrasound Surgery," *Journal of the Acoustical Society of America*, vol. 109, no. 5, pp. 2245-2253, 2001.
- [32] D. Kruse, C. Lai, D. Stephens, P. Sutcliffe, E. Paoli, S. Barnes and K. Ferrara, "Spatial and Temporal- Controlled Tissue Heating on a Modified Clinical Ultrasound Scanner for Generating Mild Hyperthermia in Tumors," *IEEE Transactions on Biomedical Engineering*, vol. 57, no. 1, 2010.
- [33] G. Pinton, J. Dahl, S. Rosenzweig and G. Trahey, "A Heterogeneous Nonlinear Attenuating Full-Wave Model for Ultrasound," *IEEE Transactions on Ultrasonics, Ferroelectrics, and Frequency Control*, vol. 56, no. 3, pp. 474-488, 2009.
- [34] K. Lee, I. Sim, G. Kang and M. Choi, "Numerical Simulation of Temperature Elevation on Soft Tissue by High Intensity Focused Ultrasound," *Modern Physics Letters B*, vol. 22, no.

11, pp. 803-807, 2008.

- [35] M. Bailey, V. Khokhlova, O. Sapozhnikov, S. Kargl and L. Clum, "Physical Mechanisms of the Therapeutic Effect of Ultrasound (a review)," *Acoustical Physics*, vol. 49, no. 4, pp. 369-388, 2003.
- [36] A. D. Pierce, *Acoustics: An Introduction to its Physical Principles and Applications*, McGraw-Hill, 1981.
- [37] R. S. C. Cobbold, *Foundations of Biomedical Ultrasound*, New York: Oxford University Press, 2007.
- [38] M. F. Hamilton and D. T. Blackstock, *Nonlinear Acoustics*, London, UK: Academic Press Lim., 1998.
- [39] R. L. Panton, *Incompressible Flow*, New York City: John Wiley & Sons, Inc., 1996.
- [40] T. Sheu, M. Solovchuk, A. Chen and M. Thiriet, "On an Acoustics–Thermal–Fluid Coupling Model for the Prediction of Temperature Elevation in Liver Tumor," *International Journal of Heat and Mass Transfer*, vol. 54, no. 17-18, pp. 4117-4126, 2011.
- [41] M. Solovchuk, T. Sheu, W. Lin, I. Kuo and M. Thiriet, "Simulation Study on Acoustic Streaming and Convective Cooling in Blood Vessels During a High-Intensity Focused Ultrasound Thermal Ablation," *International Journal of Heat and Mass Transfer*, vol. 55, pp. 1261-1270, 2012.
- [42] Y.-S. Lee and M. Hamilton, "Time-Domain Modeling of Pulsed Finite-Amplitude Sound Beams," *Journal Acoustical Society of America*, vol. 97, no. 2, pp. 906-917, 1994.
- [43] T. Hart and M. Hamilton, "Nonlinear Effects in Focused Sound Beams," *Nournal Acoustical Society of America*, vol. 84, no. 4, pp. 1488-1496, 1988.
- [44] L. Zhen-Bo, F. Ting-Bo, G. Xia-Sheng and Z. Dong, "Effect of Tissue Inhomogeneity on Nonlinear Propagation of Focused Ultrasound," *Chinese Physical Society*, vol. 27, no. 9,

2010.

- [45] X. Yang and R. Cleveland, "Time Domain Simulation of Nonlinear Acoustic Beams Generated by Rectangular," *Journal of the Acoustical Society of America*, vol. 117, no. 1, pp. 113-123, 2004.
- [46] Y. Jing, G. T. Clement and D. Shen, "Verification of the Westervelts Equation for Focused Transducers," *IEEE Transactions on Ultrasonics, Ferroelectrics, and Frequency Control*, vol. 5, p. 58, 2011.
- [47] L. APC International, *Piezoelectric Ceramics: Principles and Applications*, APC International, Ltd., 2002.
- [48] A. Arnau, *Piezoelectric Transducers and Applications*, Springer, 2008.
- [49] J. Yin, P. Zhang, W. Sun, X. Zhang, X. Jian and Z. Li, "Temperature Field FDTD Simulation of Self-Focusing and Electronic Phased Focusing in Human Body Tissues," *Bioinformatics and Biomedical Engineering 4th International Conference*, pp. 1-4, 2010.
- [50] Y.-S. Lee, "Numerical Solution of the KZK Equation for Pulsed Finite Amplitude Sound Beams in Thermoviscous Fluids," *Dissertation: University of Texas at Austin*, 1993.
- [51] X. Ynag and R. O. Cleveland, "Time Domain Simulation of Nonlinear Acoustic Beams Generated by Rectangular Pistons with Application to Harmonic Imaging," *Journal of Acoustical Society of America*, vol. 117, no. 1, pp. 113-123, 2005.
- [52] T. Kamakura, T. Ishiwata and K. Matsuda, "Model Equations for Strongly Focused Finite Amplitude Sound Beams," *Journal of the Acoustical Society of America*, vol. 107, no. 6, pp. 3035-3046, 2000.
- [53] B. Lucas and T. Muir, "The Field of a Focusing Source," *Journal of the Acoustical Society of America*, vol. 72, no. 4, pp. 1289-1296, 1982.

- [54] J. Huang, R. G. Holt, R. Cleveland and R. Roy, "Experimental Validation of a Tractable Numerical Model for Focused Ultrasound Heating in FLOW-THROUGH Tissue Phantoms," *Journal Acoustical Society of America*, vol. 116, no. 4, pp. 2451-2458, 2004.
- [55] N. Kharin and D. Vince, "Moderately Nonlinear Ultrasound Propagation in Blood-Mimicking Fluid," *Ultrasound in Medicine & Biology*, vol. 30, no. 4, pp. 501-509, 2004.
- [56] F. Li, R. Feng, Q. Zhang, J. Bai and Z. Wang, "Estimation of HIFU Induced Lesions in Vitro: Numerical Simulation and Experiment," *Ultrasonics*, vol. 44, pp. e337-e340, 2006.
- [57] A. Nakayama and F. Kuwahara, "A General Bioheat Transfer Model on the Theory of Porous Media," *International Journal of Heat and Mass Transfer*, vol. 51, pp. 3190-3199, 2008.
- [58] A. Khaled and K. Vafai, "The Role of Porous Media in Modeling Flow and Heat Transfer in Biological Tissues," *International Journal of Heat and Mass Transfer*, vol. 46, pp. 4989-5003, 2003.
- [59] E. H. Wissler, "Pennes' 1948 Paper Revisited," *American Physiological Society*, pp. 35-41, 1998.
- [60] H. Klinger, "Heat Transfer in Perfused Biological Tissue II The 'Macroscopic' Temperature Distribution in Tissue," *Bulletin of Mathematical Biology*, vol. 40, pp. 183-199, 1978.
- [61] H. Darcy, "Les Fontaines Publiques de la Ville de Dijon," *Vector Dalmont*, 1856.
- [62] J. Boussinesq, "Theorie de L'ecoulement Tourbillonnant et Tumultueux des Liquides Dans les Lits Rectilignes a Grande Section," *Gauthier-Villars et Fils*, 1897.
- [63] S. Ginter, M. Liebler, E. Steiger and T. Dreyer, "Full-Wave Modeling of Therapeutic Ultrasound: Nonlinear Ultrasound Propagation in Ideal Fluids," *Journal of Acoustical Society of America*, vol. 111, no. 5, pp. 2049-2059, 2002 .

- [64] Q.-H. Liu and J. Tao, "The perfectly Matched Layer for Acoustic Waves in Absorptive Media," *Journal of Acoustical Society of America*, vol. 102, no. 4, pp. 2072-2082, 1997.
- [65] G. Pinton, J. Dahl, S. Rosenzweig and G. Trahey, "A Heterogeneous Nonlinear Attenuating Full-Wave Model of Ultrasound," *IEEE Transactions on Ultrasonics, Ferroelectrics and Frequency Control*, vol. 56, no. 3, 2009.
- [66] T. Kako and Y. Ohi, "Numerical Method for Wave Propagation Problem by FDTD Method with PML," *University of Electro-Communications, Chofu Japan*.
- [67] Q. Liu and J. Tao, "The Perfectly Matched Layer for Acoustic Waves in Absorptive Media," *Journal of the Acoustical Society of America*, vol. 102, no. 4, pp. 2072-2082, 1997.
- [68] X. Yuan, D. Borup, J. Wiskin, M. Berggen, R. Eidens and S. Johnson, "Formulation and Validation of Berenger's PML Absorbing Boundary for the FDTD Simulation of Acoustic Scattering," *IEEE Transactions on Ultrasonics, Ferroelectrics and Frequency Control*, vol. 44, no. 4, pp. 816-822, 1997.
- [69] S. Johnson, "Notes on Perfectly Matched Layers (PML's)," *Michigan Institute of Technology*, 2010.
- [70] E. Echeverria and C. Thamire, "Development of Ultrasound-Temperature Numerical Simulator for Therapeutic Applications," *ASME IMECE Proceedings 2011*, 2011.
- [71] M. A. Averkiou, Y. S. Lee and M. F. Hamilton, "Self-Demodulation of Amplitude and Frequency-Modulated Pulses in a Thermoviscous Fluid," *Journal of the Acoustical Society of America*, vol. 94, no. 5, pp. 2876-2883, 1993.
- [72] P. Cervenka and P. Alais, "Fourier Formalism for Describing Nonlinear Self-Demodulation of a Primary Narrow Ultrasonic Beam," *Journal of the Acoustical Society of America*, vol. 88, no. 1, pp. 473-481, 1990.
- [73] H. Vos, D. Goertz and N. Jong, "Self-Demodulation of High Frequency Ultrasound,"

Journal of the Acoustical Society of America, vol. 127, no. 3, pp. 1208-1217, 2010.

- [74] F. P. Incropera, D. P. Dewitt, T. L. Bergman and A. S. Lavine, *Fundamentals of Heat and Mass Transfer*, New Jersey: Wiley, 2007.
- [75] M. Ganzarolli and L. Milanez, "Natural Convection in Rectangular Enclosures Heated from Below and Symmetrically Cooled from the Sides," *International Journal of Heat and Mass Transfer*, vol. 38, no. 6, pp. 1063-1073, 1995.
- [76] J. Leonard, "Thermal Properties of Tissue Equivalent Phantom Materials," *IEEE Transactions on Biomedical Engineering*, no. 7, pp. 533-536, 1984.
- [77] A. Worthington, J. Trachtenberg and M. Sherar, "Ultrasound Properties of Human Prostate Tissue During Heating," *Ultrasound in Medicine and Biology*, vol. 28, no. 10, pp. 1311-1318, 2002.
- [78] M. Swartz and M. Fleury, "Interstitial Flow and Its Effects in Soft Tissues," *Annual Review of Biomedical Engineering*, vol. 9, pp. 229-256, 2007.

